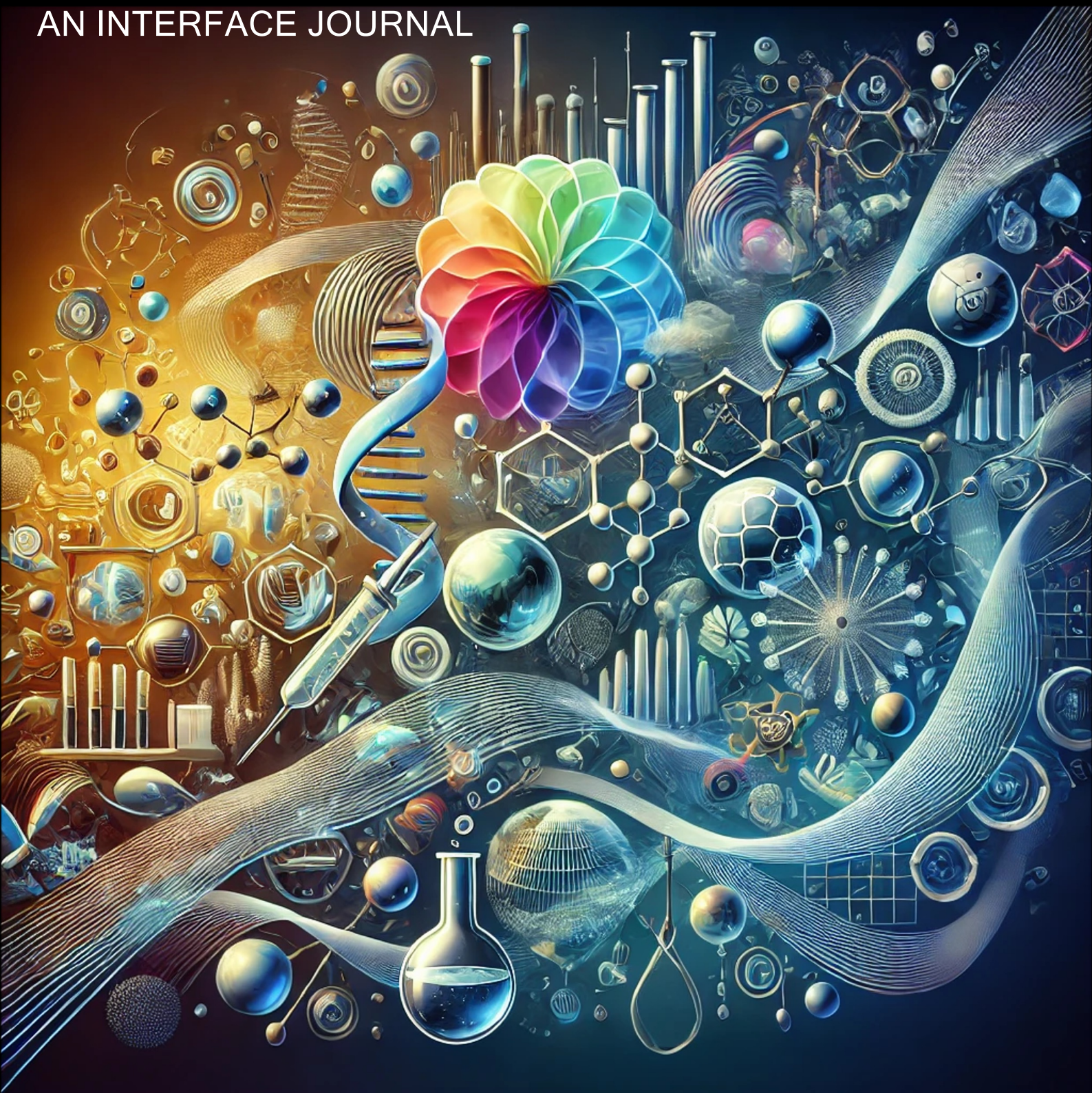


TRANSLATIONAL CHEMISTRY

AN INTERFACE JOURNAL

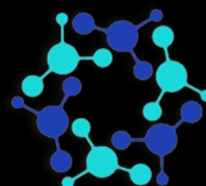


Editors in Chief

Carlos Lodeiro Y Espiño , PhD

José Luis Capelo – Martínez, PhD

Laura Mercolini, PhD



PROTEOMASS
SCIENTIFIC
SOCIETY



Translational Chemistry

An Interface Journal

EDITORIAL BOARD

Translational Chemistry Journal Editorial Board 2025

EDITORIAL

The Expanding Horizon of Translational Chemistry: From Fundamental Knowledge to Global Impact

ORIGINAL ARTICLES

Evaluation of positively charged benzothioxanthene imide derivatives as potential photosensitizers for antimicrobial photodynamic therapy

Practical application of blood microsampling: an effective VAMS-based workflow for anabolic androgenic steroids analysis

Increasing of enzymatic environmental reactions by applying Tesla valve

Enhancing Luminescent Solar Concentrators with Aggregation-Induced Emission Fluorophores: Overcoming ACQ for Efficient Light Harvesting in PMMA Films

REVIEW

Translational Advances: Biomaterials and Antimicrobial Photodynamic Therapy, a Synergic Approach

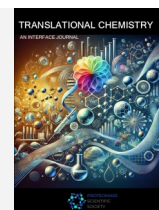
EDITORIAL BOARD



TRANSLATIONAL CHEMISTRY

AN INTERFACE JOURNAL

[HTTPS://WWW.TRANSLATIONALCHEMISTRY.COM/](https://www.translationalchemistry.com/)



EDITORIAL BOARD | DOI: 10.5584/translationalchemistry.v1i1.243

TRANSLATIONAL CHEMISTRY

AN INTERFACE JOURNAL

EDITORS-IN-CHIEF

Prof. Carlos Lodeiro

LAQV-REQUIMTE, NOVA FCT, NOVA University Lisbon, Caparica 2829-516 Portugal

Prof. Laura Mercolini

Department of Pharmacy and Biotechnology, University of Bologna, Italy

Prof. José Luis Capelo-Martínez

LAQV-REQUIMTE, NOVA FCT, NOVA University Lisbon, Caparica 2829-516 Portugal

EXECUTIVE EDITORS

Dr. Adrián Fernández-Lodeiro

Department of Electrical and Computer Engineering, University of Cyprus, Nicosia, Portugal

Prof. Elisabete Oliveira

LAQV-REQUIMTE, NOVA FCT, NOVA University Lisbon, Caparica 2829-516 Portugal

Prof. Emília Bértolo

School of Psychology and Life Sciences, Canterbury Christ Church University, UK

Prof. Hugo M. Santos

LAQV-REQUIMTE, NOVA FCT, NOVA University Lisbon, Caparica 2829-516 Portugal

Dr. Javier Fernández-Lodeiro

LAQV-REQUIMTE, NOVA FCT, NOVA University Lisbon, Caparica 2829-516 Portugal

Dr. Luís B. Carvalho

LAQV-REQUIMTE, NOVA FCT, NOVA University Lisbon, Caparica 2829-516 Portugal

Dr. Silvia Nuti

Department of Chemistry, University of Bologna, Italy

ASSOCIATED EDITORS

Prof. Ana Luísa Fernando

MEtRICs/CubicB, NOVA FCT, NOVA University Lisbon,
Caparica 2829-516 Portugal

Prof. Ana Rita Duarte

LAQV-REQUIMTE, NOVA FCT, NOVA University Lisbon,
Caparica 2829-516 Portugal

Prof. Artur Badyda

Warsaw University of Technology, Faculty of Environmental
Engineering, Poland

Prof. Atanas Kurutos

Bulgarian Academy of Sciences, Institute of Organic
Chemistry with Centre of Phytochemistry, Bulgaria

Prof. Clement Cabanetos

CNRS, University of Angers, France

Prof. Federica Pellati

University of Modena and Reggio Emilia, 41125, Modena,
Italy

Dr. Fernanda Papa Spada

University of São Paulo, Brazil

Prof. Gilberto Igrejas

University of Trás os Montes e Alto Douro, Portugal

Prof. Jakub Zdarta

Faculty of Chemical Technology, Poznan University of
Technology, Poland

Prof. Jean Christophe Pouilly

University of Caen, France

Prof. José Manuel Vila Abad

Department of Inorganic Chemistry, University of Santiago
de Compostela, Spain

Prof. Massimo La Deda

Department of Chemistry and Chemical Technology,
University of Calabria, Italy

Dr. Marco Carlotti

Dipartimento di Chimica e Chimica Industriale of the
University of Pisa, Italy

Prof. Patrícia Alexandra C.Q.D. Poeta

Veterinary and Animal Research Centre, University of Trás
os Montes e Alto Douro, Portugal

Prof. Pier Luigi Gentili

Department of Physical Chemistry - University of Perugia,
Italy

Prof. Ramón Martínez Mañez

Department of Inorganic Chemistry, Polytechnical University
of Valencia, Spain

Dr. Susana Gaudêncio

UCIBIO, NOVA FCT, NOVA University Lisbon, Caparica
2829-516 Portugal

Prof. Tarita Biver

Department of Chemistry and Industrial Chemistry -
University of Pisa, Italy

Prof. Veronica Dodero

Faculty of Chemical Technology, Poznan University of
Technology, Poland

Prof. Viviane Pilla

University of Uberlândia, Brazil

EDITORIAL



TRANSLATIONAL CHEMISTRY

AN INTERFACE JOURNAL

[HTTPS://WWW.TRANSLATIONALCHEMISTRY.COM/](https://www.translationalchemistry.com/)



EDITORIAL | DOI: 10.5584/translationalchemistry.v1i1.244

The Expanding Horizon of Translational Chemistry: From Fundamental Knowledge to Global Impact

Carlos Lodeiro^{1,2}, Laura Mercolini³, José Luis Capelo^{1,2}

¹ BIOSCOPE Research Group, LAQV-REQUIMTE, Chemistry Department, NOVA School of Science and Technology, Universidade NOVA de Lisboa, 2829-516 Caparica, Portugal; ² PROTEOMASS Scientific Society, 2825-466, Costa de Caparica, Portugal; ³ Research group of Pharmaco-Toxicological Analysis (PTA Lab), Department of Pharmacy and Biotechnology (FaBiT), Alma Mater Studiorum – University of Bologna, Via Belmeloro 6, 40126 Bologna, Italy

Received: March 2025 **Accepted:** March 2025 **Available Online:** June 2025

The Expanding Horizon of Translational Chemistry: From Fundamental Knowledge to Global Impact

The concept of Translational Research emerged as a response to the pressing need to bridge the gap between basic scientific discoveries and their practical applications - particularly in the biomedical and clinical sciences. Today, this philosophy has matured and transcended its original scope. In an increasingly interconnected and interdisciplinary scientific landscape, chemistry - the central science - holds the unique potential to drive translational efforts across a diverse range of disciplines. It is from this understanding that Translational Chemistry arises.

At its core, Translational Chemistry embodies the integration of chemical principles and innovations into applications that address real-world challenges. But its scope extends further - it reflects a mindset, a methodological approach that breaks down disciplinary silos, enabling chemical knowledge to interface seamlessly with biology, physics, engineering, environmental sciences, and medicine. It is this cross-pollination that fuels innovation and economic progress.

The field is not limited to pharmaceutical development or medical diagnostics. Instead, it spans the entire chemical spectrum - from synthetic organic and inorganic chemistry to analytical and physical chemistry, and into more specialized domains such as:

- Biochemistry and Biological Chemistry, where molecular-level understanding enables breakthroughs in disease mechanisms and drug design;
- Forensics and Conservation Science, where chemistry aids in crime scene analysis or the restoration of cultural heritage;
- Pharmaceutical and Medicinal Chemistry, where drug development and analytical innovation converge to translate discovery into life-saving therapeutics;
- Environmental Chemistry, addressing global sustainability and pollution mitigation;
- Chemical Engineering and Industrial Chemistry, where scalability, safety, and process optimization transform lab discoveries into products;
- Materials Chemistry and Nanochemistry, enabling the design of functional materials with applications in energy, electronics, and beyond.

Translational Chemistry is, therefore, not a new discipline, but rather a new paradigm - an interface perspective - that recognizes the pivotal role of chemistry in societal advancement. It promotes a looped model of innovation:

From fundamental research → technological development → industrial implementation → societal benefit → and back to fundamental inquiry informed by new questions.

This inaugural first issue of the *Translational Chemistry: An Interface Journal* is a testament to this vision. Here, we present contributions that exemplify this translational ethos - from novel chemical sensors with diagnostic utility, to catalytic systems with industrial relevance, to sustainable chemical processes designed to meet the goals of the green economy. These studies demonstrate how chemistry can serve as a connector between lab-scale discovery and large-scale impact.

The rich and diverse panel of editors aim for this journal to serve as a platform where chemists and scientists from all related disciplines find a common language and a shared mission: to apply the rigour and creativity of chemistry to solve global challenges. Whether you're designing a new compound, developing a device, or scaling a process, *Translational Chemistry* invites you to think beyond your bench - to the clinic, the factory, the ecosystem, the museum, the classroom, the daily live.

Translational Chemistry is not only a scientific approach, but a collaborative spirit. It is an invitation to connect ideas, methods and people - to build a chemical interface that is as human as technical.

We welcome all those who see chemistry not just as a science, but as a force for transformation.

Prof. Carlos Lodeiro

Prof. Laura Mercolini

Prof. José Luis Capelo

Editors-in-chief

Translational Chemistry: An Interface Journal

ORIGINAL ARTICLES



TRANSLATIONAL CHEMISTRY

AN INTERFACE JOURNAL

HTTPS://WWW.TRANSLATIONALCHEMISTRY.COM/



ORIGINAL ARTICLE | DOI: 10.5584/translationalchemistry.v1i1.240

Evaluation of positively charged benzothioxanthene imide derivatives as potential photosensitizers for antimicrobial photodynamic therapy

Joana Galhano,¹ Darío Puchán Sánchez,² Ahmad Kassem,² Magali Allain,² Maria Paula Duarte,³ Carlos Lodeiro,^{1,4,5} Clément Cabanetos,^{2,*} Elisabete Oliveira,^{1,4,5,*}

¹ BIOSCOPE Research Group, LAQV-REQUIMTE, Chemistry Department, NOVA School of Science and Technology, Universidade NOVA de Lisboa, 2829-516 Caparica, Portugal; ² CNRS, MOLTECH-ANJOU, SFR-MATRIX, F-49000 Angers, France; ³ METRICS / NOVA School of Science and Technology, Universidade NOVA de Lisboa, Campus de Caparica, 2829-516, Caparica, Portugal; ⁴ Canterbury Christ Church University, School of Human and Life Sciences, Life, Sciences Industry Liaison Lab, Sandwich, UK; ⁵ PROTEOMASS Scientific Society, 2825-466, Costa de Caparica, Portugal

Received: March 2025 Accepted: April 2025 Available Online: June 2025

ABSTRACT

Given the growing concern over antimicrobial resistance (AMR), the search for new alternative therapeutic strategies has increased, with antimicrobial photodynamic therapy (aPDT) emerging as a promising solution. This study aims at exploring the potential of two positively charged Benzothioxanthene imide derivatives (BTI) derivatives, namely BTI-Pyr⁺-CH₃ (C1) and DBI-Pyr⁺-CH₃ (C2) as photosensitizers for aPDT. In this context, C1 and C2 were successfully synthesized, fully characterized, and their antibacterial activity against Gram-negative and Gram-positive bacteria evaluated. The results demonstrate that both compounds exhibit phototoxic effects under light exposure, with enhanced inhibitory and bactericidal activity at lower concentrations than those reported in the existing literature. Notably, Compound C1 displayed the most promising antibacterial effects, showing inhibitory activity at concentrations approximately 20 times lower than those previously reported. The study highlights the significant light-dependent antibacterial properties of these affordable and accessible compounds, particularly against Gram-positive bacteria, suggesting a potential use for future antimicrobial applications.

Keywords: Antimicrobial Photodynamic Therapy (aPDT); Benzothioxanthene imide derivatives (BTI); Bacteria.

Introduction

The increase of antimicrobial resistance (AMR) mechanisms throughout commonly occurring bacterial colonies is becoming an alarming public health concern [1]. The new Global Research Agenda for Antimicrobial Resistance in Human Health, developed by the World Health Organization (WHO) [2], emphasizes the need for prevention strategies that aim to prevent infections before they occur. This guideline not only reduces the need for antibiotic use but also helps slow the spread of resistance mechanisms in microorganisms present in both domestic and clinical environments. This approach focuses on inhibiting or inactivating microorganisms before they can infect a human host, preventing the onset of the infectious process.

A promising alternative that has gained attention is the use of antimicrobial photodynamic therapy (aPDT) [3]. This process is based on a light-dependent oxygen-dependent photochemical reaction, used to, *in situ*, generate reactive oxygen species (ROS). In

the context of PDT, two ROS can be formed through two distinct fundamental mechanisms: Type I and II. Type I is commonly characterized by the production of radicals through electron/hydrogen transferences, yielding superoxide anions that can subsequently be transformed into more reactive ROS. On the other hand, the direct production of singlet oxygen through energy transfer typically characterizes Type II [4]. Both mechanisms can produce a significant antimicrobial effect, serving as an effective alternative to traditional antibiotics. However, while aPDT has a broad range of potential applications, most studies in the literature focus primarily on its use as an anticancer treatment, as well as in dentistry and dermatological applications [5–8].

Benzothioxanthene imide (BTI), a sulfur-containing rylene imide dye, has recently emerged as a highly promising alternative to state-of-the-art photosensitizers for PDT. Its unique chemical structure allows for efficient light absorption and precise modulation of its optoelectronic properties. Upon specific functionalization of its π -conjugated backbone, the selective generation of reactive oxygen species (ROS I and/or ROS II) has been demonstrated [9,10]

*Corresponding author: clement.cabanetos@univ-angers.fr (CC) and ej.oliveira@fct.unl.pt (EO)

making it an excellent candidate for photonics and biophotonics applications, particularly in PDT [11,12]. The compound's high photostability and strong fluorescence further enhance its potential for both therapeutic and diagnostic purposes, enabling targeted treatments with minimal damage to healthy tissue [13]. As a versatile photosensitizer, BTI holds considerable promise for advancing non-invasive, targeted therapies in areas such as cancer treatment; however, its antimicrobial properties and applications remained, to date, unexplored. It is in this precise context that we present the synthesis, characterization, and evaluation of this family of compounds as potential photosensitizers for antimicrobial photodynamic therapy (aPDT). Prepared with minimal synthetic efforts, through a straightforward route, two positively charged derivatives were tested, under light and dark incubation conditions, against a broad spectrum of Gram-positive and Gram-negative bacterial strains. The obtained results in this study confirmed the high potential of such structures with promising and selective phototoxicity.

Materials and Methods

Chemicals and Starting Materials

Mueller-Hinton Broth (MHB), Mueller-Hinton Agar (MHA) and Tryptone Soy Agar (TSA) were acquired from Biokar. Sodium Chloride was purchased from Sigma Aldrich. The **BTI**, **BTI-Br** and **DBI** were prepared from the literature [11,14,15]. Chemicals, reagents and solvents used for the preparation of both **BTI-Pyr⁺-CH₃** and **DBI-Pyr⁺-CH₃** were purchased from Sigma Aldrich. Thin Layer Chromatographies (TLCs) were performed on pre-coated aluminium sheets with 0.20 mm Merck Alugram SIL G/UV254 under UV @ 254nm. Column chromatography purifications were carried out using Sigma-Aldrich silica gel 60 (particle size 63-200 µm). Lab Armor™ beads were purchased from Thermo Fisher Scientific.

Instrumentation

Nuclear magnetic resonance (NMR) ¹H and ¹³C spectra were obtained on a Bruker 300 MHz Avance III spectrometer (300 MHz for ¹H and 75 MHz for ¹³C), on a Bruker 500 MHz Avance III HD spectrometer (500 MHz for ¹H and 125 MHz for ¹³C) and on a Bruker 600 MHz Avance III HD spectrometer (600 MHz for ¹H and 151 MHz for ¹³C). Chemical shifts were reported in ppm according to tetramethylsilane using the solvent residual signal as an internal reference (CDCl₃: δH = 7.26 ppm, δC = 77.16 ppm and DMF-d₇: δH = 8.03 ppm, δC = 163.13 ppm). Coupling constants (J) were given in Hz. NMR spectra were measured at 25°C. Resonance multiplicity was described as s (singlet), d (doublet), t (triplet), m (multiplet), dd (doublet of doublets), tt (triplet of triplets), td (triplet of doublets), and br (broad signal). Carbon spectra were acquired with a complete decoupling for the proton. High resolution mass spectrometry (HRMS) was performed with a JEOL JMS-700 B/E. Crystal data were collected on a Rigaku Oxford Diffraction SuperNova diffractometer equipped with an Atlas CCD detector and micro-focus Cu-K_α radiation (λ = 1.54184 Å). The

structures were solved by dual-space algorithm and refined on F2 by full matrix least-squares techniques using SHELX package (G.M. Sheldrick, ShelXL2019/3). All non-hydrogen atoms were refined anisotropically, and the H atoms were included in the calculation without refinement. Multiscan empirical absorption was corrected by using CrysAlisPro program (CrysAlisPro, Rigaku Oxford Diffraction, V1.171.41.118a, 2021). Deposition Number(s) 2428516 (for **BTI-Pyr**) and 2428517 (for **DBI-Pyr**) contain(s) the supplementary crystallographic data for this paper. This data is provided free of charge by the joint Cambridge Crystallographic Data Centre and Fachinformationszentrum Karlsruhe Access Structures service.

Antibacterial assays were conducted under asepsis conditions, ensured by a STERIL-VBH Laminar Flux Chamber. Incubations were conducted in a Mermmet Incubator B10. Sterile, single-use loops, transparent clear bottom 96-well plates were acquired from Greiner Bio-One. Bacterial suspension concentrations were adjusted with a Densitometer DEN-1B (Grant-Bio).

Synthesis of compounds

BTI-Pyr: To an oven dried Schlenk tube containing a stirring bar, **BTI-Br** (200 mg, 0.442 mmol), pyridin-4-ylboronic acid (81 mg, 0.663 mmol), Pd(PPh₃)₄ (50 mg, 0.044 mmol) and K₂CO₃ (183 mg, 1.3 mmol) were sequentially added. The solids were degassed 3 times under vacuum followed by a flow of argon. After addition of degassed dioxane and water (7:1 V:V ratio) the reaction mixture was heated to 110 °C in a bath of Lab Armor™ beads for 4 hours. After cooling down to room temperature, the mixture was diluted with dichloromethane (approx. 30 mL), transferred into a decantation flask where it was washed with water (3x30mL). Organic phases were then dried over MgSO₄ before being concentrated under vacuum. The crude was finally purified by column chromatography on silica gel using CHCl₃/MeOH (99:1) as eluent to afford BTI-Pyr as a yellow-orange solid (185 mg, 93%). ¹H NMR (300 MHz, CDCl₃) δ 8.86 – 8.78 (m, 2H), 8.65 (d, J = 7.9 Hz, 1H), 8.35 – 8.18 (m, 3H), 7.50 – 7.33 (m, 4H), 7.27 (m, 1H) 5.06 (m, 1H), 2.34 – 2.14 (m, 2H), 1.98 – 1.83 (m, 2H), 0.95 – 0.84 (t, J = 7.5 Hz, 6H). ¹³C NMR (151 MHz, CDCl₃) δ 150.9, 146.6, 138.3, 136.9, 132.3, 132.3, 132.2, 132.1, 132.0, 131.3, 131.2, 130.1, 128.7, 128.6, 128.0, 127.7, 126.8, 126.1, 126.0, 124.0, 120.0, 57.6, 25.0, 11.4. HRMS (MALDI-TOF) m/z: Calculated for C₂₈H₂₂N₂O₂S (M⁺) 450.13965; Found 450.13930 (Δ = -0.78 ppm).

BTI-Pyr⁺-CH₃: (30 mg, 0.067 mmol) was dissolved in acetonitrile (6 mL) MW tube equipped with a magnetic stirred. Iodomethane (18 mg, 0.133 mmol) was then added dropwise, and the reaction mixture was heated to 110 °C in a bath of Lab Armor™ beads for 16 hours. The reaction mixture was cooled down to room temperature before evaporating the solvent under reduced pressure. The resulting solid was washed with a mixture of PE/DCM (8:2) to afford a dark red solid (38 mg, 80 %). ¹H NMR (600 MHz, DMF-d₇) δ 9.50 (d, J = 6.1 Hz, 2H), 8.76 (d, J = 8.2 Hz, 1H), 8.70 (d, J = 6.0 Hz, 2H), 8.68 (d, = 8.0 Hz, 1H), 8.63 – 8.60 (m, 1H), 8.35 (s, 1H), 7.76 – 7.70 (m, 1H), 7.60 – 7.55 (m, 2H), 5.06 – 4.99 (m, 1H), 2.30 – 2.19 (m, 2H), 1.96 – 1.86 (m, 2H), 0.89 (t, J = 7.5 Hz, 6H).

^{13}C NMR (151 MHz, DMF-d₇) δ 206.0, 154.6, 147.1, 138.5, 136.7, 133.9, 133.2, 132.1, 132.1, 131.8, 131.7, 130.9, 130.2, 129.8, 128.9, 128.8, 128.8, 128.7, 128.3, 127.4, 126.9, 126.9, 125.6, 121.5, 57.2, 48.2, 24.7, 10.9. HRMS (MALDI-TOF) m/z: Calculated for C₂₉H₂₅N₂O₂S (M⁺) 465.16313; Found 465.16290 (Δ = -0.48 ppm).

DBI-Br: To a solution of DBI (500 mg, 1.18 mmol) in CH₂Cl₂ (90 mL) was added dropwise a 1 M solution of bromine in CH₂Cl₂ (190 mg, 1.18 mmol). The reaction mixture was refluxed for 16 h before being quenched with a saturated aqueous solution of Na₂S₂O₃. The organic phase was washed with water (2x) and brine (1x), dried over MgSO₄ and concentrated under reduced pressure. The resulting crude was purified by column chromatography on silica gel using CH₂Cl₂ as eluent to afford the target DBI-Br as orange solid (416 mg, 70%). ^1H NMR (300 MHz, CDCl₃) δ (ppm) 8.70 – 8.58 (m, 3H), 8.47 (d, J = 8.1 Hz, 1H), 7.90 – 7.81 (m, 2H), 7.58 – 7.50 (m, 2H), 7.46 (d, J = 8.6 Hz, 1H), 5.16 – 5.01 (m, 1H), 2.35 – 2.18 (m, 2H), 2.00 – 1.84 (m, 2H), 0.91 (t, J = 7.5 Hz, 6H). ^{13}C NMR (76 MHz, CDCl₃) δ (ppm) 136.7, 134.2, 133.0, 131.4, 130.8, 130.2, 129.2, 129.0, 127.7, 127.0, 126.5, 125.1, 124.0, 123.2, 114.1, 77.6, 57.7, 25.0, 11.5. HRMS (MALDI-TOF) m/z calculated for C₂₇H₂₀BrNO₂S (M⁺) 501.03926, found: 501.03900 (Δ = -0.57 ppm).

DBI-Pyr: To an oven dried Schlenk tube charged with a stirring bar was loaded DBI-Br (200 mg, 0.398 mmol), pyridin-4-ylboronic acid (73.39 mg, 0.597 mmol), Pd(PPh₃)₄ (46 mg, 0.0398 mmol) and K₂CO₃ (105 mg, 0.76 mmol). These powders were exposed to 3 vacuum/argon refilling cycles. Then, degassed dioxane and water (7:1 V:V ratio) were added and the reaction mixture was heated to 110 °C in a bath of Lab Armor™ beads for 5 hours. Cooled down to room temperature, the reaction mixture was diluted with CH₂Cl₂, and the organic phase was washed with water (2x) before being dried over MgSO₄, filtered and concentrated under vacuum. The dark crude was finally purified by column chromatography on silica gel using CHCl₃/MeOH (99:1) as eluent to afford DBI-Pyr as a yellow-orange solid (186 mg, 93%). ^1H NMR (500 MHz, CDCl₃) δ 8.82 (d, J = 5.1 Hz, 2H), 8.71 – 8.64 (m, 2H), 8.49 (d, J = 8.1 Hz, 1H), 8.36 (s, 1H), 7.87 (dd, J = 6.2, 3.3 Hz, 1H), 7.80 (d, J = 8.6 Hz, 1H), 7.60 – 7.52 (m, 4H), 7.31 (d, J = 8.5 Hz, 1H), 5.15 – 5.05 (m, 1H), 2.35 – 2.22 (m, 2H), 1.99 – 1.87 (m, 2H), 0.92 (t, J = 7.4 Hz, 6H). ^{13}C NMR (126 MHz, CDCl₃) δ 151.0, 146.6, 138.3, 136.9, 132.3, 132.2, 132.1, 132.0, 131.3, 131.2, 130.1, 128.7, 128.6, 128., 127.7, 126.8, 126.1, 126.0, 124.0, 120.0, 57.6, 25.0, 11.4. HRMS (MALDI) m/z: calculated for C₃₂H₂₄N₂O₂S (M⁺): 500.15530, found: 500.15470 (Δ = -1.13 ppm).

DBI-Pyr⁺-CH₃: the BTI-Pyr precursor (30 mg, 0.060 mmol) was charged in a microwaved reactor and subsequently dissolved in acetonitrile (6 mL) before adding dropwise iodomethane (17 mg, 0.119 mmol) under stirring. The reaction mixture was warmed up to 110 °C in a bath of Lab Armor™ beads and stirred for 24h. Once cooled down to room temperature, the solvent was directly evaporated the resulting powder was washed with a mixture of PE/DCM (8:2) to afford a dark purple solid (36 mg, 93%). ^1H NMR (300 MHz, DMF-d₇) δ 9.48 (d, J = 6.1 Hz, 2H), 8.86 – 8.65 (m, 4H),

8.42 (s, 1H), 8.14 (t, J = 7.3 Hz, 2H), 7.72 – 7.68 (m, 2H), 7.66 – 7.60 (m, 2H), 5.24 – 4.93 (m, 1H), 4.75 (s, 3H), 2.36 – 2.20 (m, 2H), 2.00 – 1.85 (m, 2H), 0.91 (t, J = 7.4 Hz, 6H). ^{13}C NMR (76 MHz, DMF-d₇) δ 155.5, 148, 138.7, 137.6, 135.3, 135.1, 133.8, 133, 132.8, 132.7, 132.3, 131.9, 130.8, 130.4, 130.3, 129.8, 129.7, 129.5, 129.1, 128.4, 128.3, 125.9, 125.1, 124.2, 58.1, 49, 25.7, 11.9. HRMS (MALDI) m/z: calculated for C₃₃H₂₇N₂O₂S⁺ (M⁺) 515.17878, found: 515.17790 (Δ = -1.68 ppm).

Photophysical Characterization

Stock solutions at a concentration of 10⁻² M were made for each compound (BTI-Pyr⁺-CH₃ (C1) and DBI-Pyr⁺-CH₃ (C2)) in MilliQ-H₂O. Absorption, emission and lifetime measurements were conducted using an aqueous solution of the compounds at a concentration of 10⁻⁵ M, obtained through an appropriate dilution of the stock solution. All spectra were acquired with a room temperature of 25 °C. Luminescent quantum yields were calculated using as a standard an ethanolic solution of fluorescein [Φ = 0.79] [16].

Antibacterial Assays

To determine the antibacterial activity of the compounds, the following strains were selected: *Escherichia coli* (*E. coli*, ATCC® 25922TM), *Salmonella enterica* subsp. *Enterica* serovar *Cholerasuis* (*Salmonella Cholerasuis*, ATCC® 10708TM), *Staphylococcus aureus* (*S. aureus*, ATCC® 6538TM), and methicillin-resistant *Staphylococcus aureus* (MRSA, ATCC® 33591TM). These were evaluated according to broth microdilution protocols, already published by our group [17]. Briefly, a gradient concentration of 95 -0.2 µg/mL for each compound was obtained through successive dilutions in a 96-well plate and incubated with a constant bacterial concentration. These assays were performed under light and dark incubation conditions, with an incubation period of ca. 18 hours. After this incubation period, 5 µL of each well were removed and plated onto a fresh TSA plate and once again incubated overnight under dark conditions to determine bactericidal conditions.

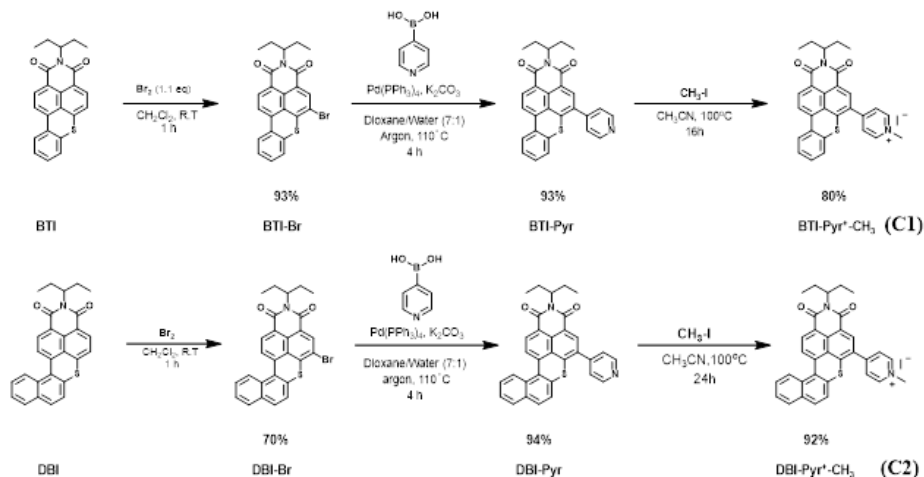
Results and Discussion

Synthesis of BTI-Pyr⁺-CH₃ (C1) and DBI-Pyr⁺-CH₃ (C2)

The synthetic route to both compounds is depicted in **Scheme 1**. Based on a common strategy, both dyes, referred to as BTI and DBI, were initially selectively brominated on the upper naphthalene ring at the alpha position. The effects of the sulfur heteroatom in conjunction with the electron-withdrawing nature of the imide make this position highly reactive towards electrophilic aromatic substitutions thus allowing a straightforward, efficient and selective bromination under mild conditions, using only 1.1 equivalents of bromine at room temperature. The resulting compounds were subjected to a Suzuki-Miyaura cross-coupling reaction with commercially available pyridin-4-ylboronic acid, achieving yields over 90% under optimized conditions established by our group.

The resulting pyridine functionalized compounds (**BTI-Pyr** and **DBI-Pyr**) were finally quaternized in the presence of iodomethane, in acetonitrile. As the desired charged compounds (**C1** and **C2**)

were formed, their limited solubility in acetonitrile caused gradual precipitation, which enhanced their conversion and facilitated their separation from the reaction mixture.



Scheme 1 | Synthetic route to both BTI-Pyr⁺-CH₃ (**C1**) (top) and DBI-Pyr⁺-CH₃ (**C2**) (bottom).

Photophysical Characterization

Absorption and emission spectra of both charged compounds, *ie*, **C1** and **C2** were performed in aqueous solutions at 25 °C, and the main results are depicted in **Figure 1**. Compounds **C1** and **C2** exhibit absorption bands at 478 nm and 504 nm, respectively, and emission bands at 536 and 571 nm. Compound **C1** demonstrates a higher emission quantum yield ($\Phi = 21\%$) compared to **C2** ($\Phi = 8\%$). The red shift in the characterization bands of **C2** compared to **C1** was primarily attributed to the presence of an extra aromatic ring in the lower part of the molecule (naphthyl vs phenyl). This additional aromatic ring in **C2** extends the π -conjugation, resulting in a bathochromic shift of about 26 nm in absorption and 35 nm in emission with respect to its phenyl counterpart (**C1**). However, this structural change also results in decreased planarity of the molecule, leading to increased spin orbit coupling and therefore intersystem crossing [11,18]. This instability is also reflected in the lifetime measurements, where **C1** exhibits a longer lifetime,

indicating greater stability in the excited state compared to **C2**.

Antibacterial Assays

To assess their antibacterial activity, a broth microdilution assay was selected as it allows for a high-throughput evaluation of inhibitory and bactericidal conditions [19]. To perform this assay, 1 mg/mL aqueous stock solutions were prepared for each compound, and successive dilutions with MHB were performed in a 96-well plate. After the concentration gradients were established, a constant volume of bacterial suspension was added to each well. To determine the influence of light irradiation on the antibacterial activity, two sets of plates were prepared in the same manner. One set was incubated for approximately 18 hours under dark conditions, while the second set was placed in a clear incubator to allow white-light irradiation for the same duration. Biological duplicates were prepared for each tested condition.

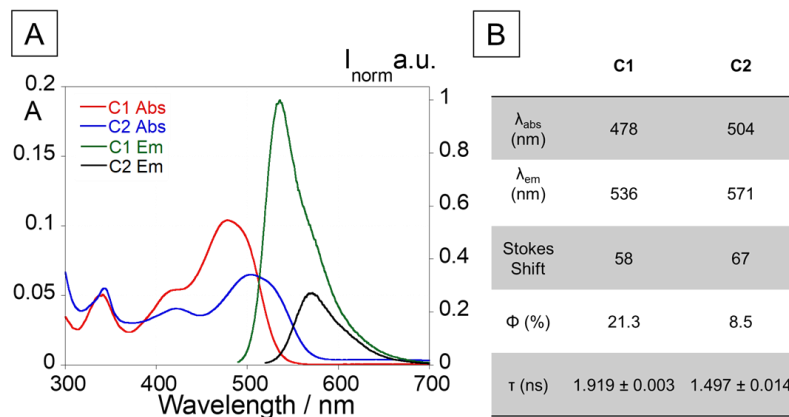


Figure 1 | Photophysical characterization of compounds **C1** and **C2** (absorption, emission, fluorescence quantum yield and lifetime). Absorption and emission spectra were collected at a sample concentration of 10^{-5} M. ($\lambda_{\text{C1 exc}} = 478$ nm; $\lambda_{\text{C2 exc}} = 504$ nm; $T = 25^\circ\text{C}$).

After the incubation cycles, the optical density at 600 nm (OD_{600}) was measured for each well, and data was plotted to correlate sample concentrations with Bacterial Growth percentages, as shown in **Figure 2**. To perform a comparative analysis between the compounds, the Minimum Inhibitory Concentration (MIC), described herein as a decrease of 50% in bacterial growth in the presence of the compound under analysis, was determined (**Figure 2**). To further investigate the antibacterial activity of these compounds, the Minimum Bactericidal Concentration (MBC) was evaluated. An aliquot of 5 μ L was removed from each well, plated

onto a TSA plate, followed by an overnight incubation period to allow bacterial growth. This step allows for the evaluation of bacterial viability, and, subsequently, the bactericidal activity of compounds, by transferring the bacteria to a medium free of the test compound. If the compound only exerts inhibitory action, bacterial colonies will grow in its absence. Conversely, if the compound demonstrates bactericidal activity, no bacterial growth is expected. To perform a comparative analysis of the antibacterial activity of the compounds, both the MIC and MBC values were determined, as previously described.

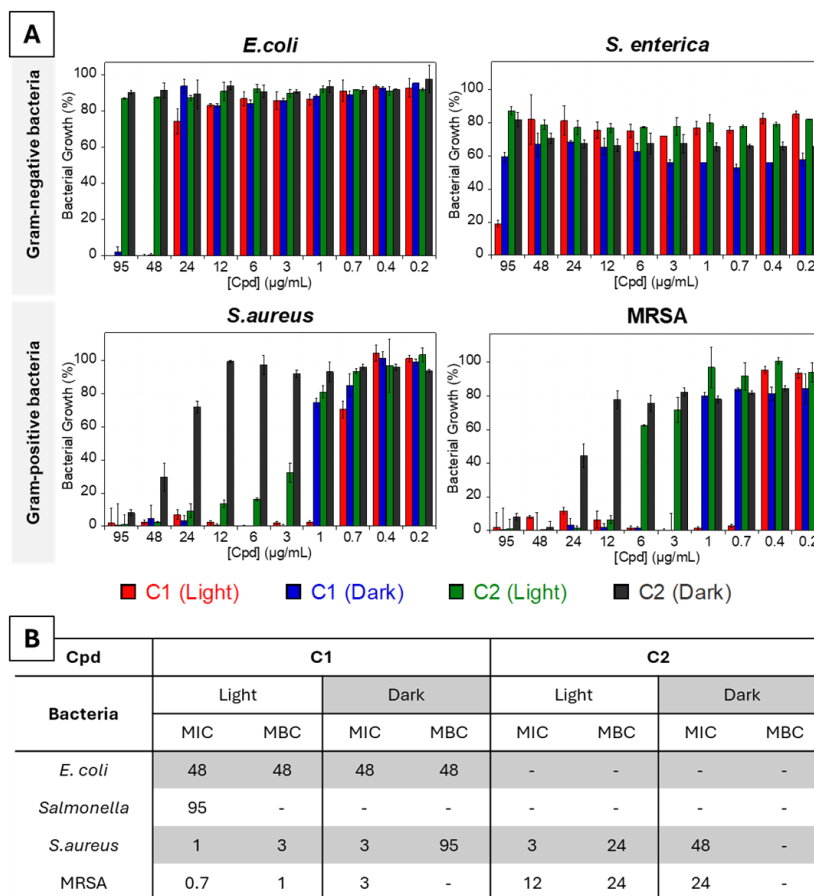


Figure 2 | Bacterial growth profiles (A) of all tested strains, with MIC values (B) represented as compound concentrations (μ g/mL).

A clear difference was observed in responses between Gram-positive and Gram-negative bacteria. Regarding the tested Gram-negative bacteria (*E. coli* and *S. enterica*), it was found that only C1 exhibited significant inhibitory and bactericidal activity. This compound indeed exhibited inhibitory/bactericidal activity against *E. coli* at a concentration of 48 μ g/mL, with no observed alterations under light or dark incubation conditions. On contrary, for *S. enterica*, an inhibitory effect was observed at a concentration of 95 μ g/mL, with a clear dependence on light irradiation, indicating light sensitivity in this system. Our study also revealed the strong inhibitory effects of both compounds on the tested Gram-positive bacteria (*S. aureus* and MRSA), with a pronounced light-sensitivity. Compound C1 demonstrated the strongest inhibitory and bactericidal effects against *S. aureus*, with MIC values of 1 and 3 μ g/mL under light and dark incubation conditions, respectively.

Significant bactericidal effects were also observed in these conditions, with MBC values of 3 and 95 μ g/mL, respectively. Regarding C2, it also exhibited inhibitory and bactericidal effects with notable modulation in presence of light since MIC of 3 μ g/mL were measured under irradiation compared to 48 μ g/mL in the dark. Similar results were obtained for MRSA, with C1 showing inhibitory effects at 0.7 and 3 μ g/mL under light and dark conditions, respectively, 12 and 24 μ g/mL were determined for C2. These findings thus underscore the potential applications of these compounds in light-sensitive environments.

The antibacterial properties of compounds containing the pyridine moiety are well-documented in the literature, with various proposed mechanisms of action [20]. However, the compounds tested here demonstrated improved inhibitory and bactericidal effects at lower concentrations compared to those reported in the

literature. For instance, compared to other pyridine-based compounds that exhibited inhibitory activity at concentrations of 32 µg/mL against *S. aureus* [21], **C1** showed similar inhibitory effects at concentrations approximately 20 times lower. Moreover, both compounds tested here showed significant inhibitory effects against MRSA, competitive with those reported in the literature where pyridine-based compounds had MICs ranging from 32 to 512 µg/mL, substantially higher than the values determined for the compounds tested herein [22]. While further studies are needed to fully understand the antibacterial mechanisms of these compounds, they exhibit promising antibacterial behavior, particularly modulated by light irradiation.

Concluding remarks

By confirming the potential of benzothioxanthene imide derivatives as effective photosensitizers for antimicrobial photodynamic therapy (aPDT), this study presents new design principles, aimed at enhancing efficacy and selectivity. Both compounds **C1** and **C2** exhibit significant antibacterial effects, with **C1** showing superior performances, especially against Gram-positive bacteria, under light irradiation. These findings indicate that this simple, yet readily accessible compound holds great promise for further development as a novel antimicrobial agent, offering a potential solution to combat antibiotic-resistant bacterial strains. Its applicability could extend to both medical and environmental settings to both treatment and prevention.

Acknowledgements

This work was supported by the Associate Laboratory for Green Chemistry - LAQV which is financed by national funds from FCT/MCTES (LA/P/0008/2020 DOI 10.54499/LA/P/0008/2020, UIDP/50006/2020 DOI 10.54499/UIDP/50006/2020 and UIDB/50006/2020 DOI 10.54499/UIDB/50006/2020) as well as the Scientific Society PROTEOMASS (Portugal) for funding support (General Funding Grant 2023-2024). J.G. thanks FCT/MEC (Portugal) for her doctoral grant 2022.09495.BD. E.O thanks FCT/MEC (Portugal) for the individual contract, CEECIND/05280/2022. The MITI, from CNRS, is acknowledged for the PhD grants of both A.K and D.P.S. C.L thanks to the Royal Society of Chemistry (RSC) by the Sustainable Laboratories Grant 2023 (Reference L23-8861107285)

References

[1] Salam MA, Al-Amin MY, Salam MT, Pawar JS, Akhter N, Rabaan AA, Alqumber MAA. Antimicrobial Resistance: A Growing Serious Threat for Global Public Health. *Healthcare* 2023;11:1946. <https://doi.org/10.3390/HEALTHCARE11131946>.

[2] Publication Item n.d. <https://www.who.int/publications/item/9789240102309> (accessed March 16, 2025).

[3] Piksa M, Lian C, Samuel IC, Pawlik KJ, Samuel IDW, Matczyszyn K. The role of the light source in antimicrobial photodynamic therapy. *Chem Soc Rev* 2023;52:1697–722. <https://doi.org/10.1039/DOCS01051K>.

[4] Sperandio FF, Huang Y-Y, Hamblin MR. Antimicrobial Photodynamic Therapy to Kill Gram-negative Bacteria. *Recent Pat Antiinfect Drug Discov* 2013;8:108. <https://doi.org/10.2174/1574891X113089990012>.

[5] Rajesh S, Koshi E, Philip K, Mohan A. Antimicrobial photodynamic therapy: An overview. *J Indian Soc Periodontol* 2011;15:323. <https://doi.org/10.4103/0972-124X.92563>.

[6] Zhou Z, Song J, Nie L, Chen X. Reactive Oxygen Species Generating Systems Meeting Challenges of Photodynamic Cancer Therapy. *Chem Soc Rev* 2016;45:6597. <https://doi.org/10.1039/C6CS00271D>.

[7] Almenara-Blasco M, Pérez-Laguna V, Navarro-Bielsa A, Gracia-Cazaña T, Gilaberte Y. Antimicrobial photodynamic therapy for dermatological infections: current insights and future prospects. *Frontiers in Photobiology* 2024;2. <https://doi.org/10.3389/FPHBI.2024.1294511>.

[8] Gholami L, Shahabi S, Jazaeri M, Hadilou M, Fekrazad R. Clinical applications of antimicrobial photodynamic therapy in dentistry. *Front Microbiol* 2023;13. <https://doi.org/10.3389/FMICB.2022.1020995>.

[9] Sazuk K, Kassem A, Dudek M, Sánchez DP, Khrouz L, Allain M, Welch GC, Sabouri M, Monnereau C, Josse P, Cabanetos C, Deiana M. Organelle-Specific Thiochromenocarbazole Imide Derivative as a Heavy-Atom-Free Type I Photosensitizer for Biomolecule-Triggered Image-Guided Photodynamic Therapy. *J Phys Chem Lett* 2025;2273–82. <https://doi.org/10.1021/acs.jpcllett.5c00136>.

[10] Puchán Sánchez D, Josse P, Plassais N, Park G, Khan Y, Park Y, Seinfel M, Guyard A, Allain M, Gohier F, Khrouz L, Lungerich D, Ahn HA, Walker B, Monnereau C, Cabanetos C, Le Bahers T. Driving Triplet State Population in Benzothioxanthene Imide Dyes: Let's twist! *Chemistry – A European Journal* 2024;30:e202400191. <https://doi.org/10.1002/CHEM.202400191>.

[11] Deiana M, Castán JMA, Josse P, Kahsay A, Puchan-Sánchez D, Morice K, et al. A new G-quadruplex-specific photosensitizer inducing genome instability in cancer cells by triggering oxidative DNA damage and impeding replication fork progression. *Nucleic Acids Res* 2023;51:6264–85. <https://doi.org/10.1093/NAR/GKAD365>.

[12] Deiana M, Josse P, Dalinot C, Osmolovskiy A, Marqués PS, Castán JMA, Gillet N, Ravindranath R, Patel AM, Sengupta P, Obi I, Rodríguez-Marquez E, Khrouz L, Dumont E, Abad-Galán L, Allain M, Walker B, Ahn HS, Maury O, Blanchard P, Le Bahers T, Ohlund D, von Hofsten J, Monneraru C, Cabanetos C, Sabouri N. Site-selected thionated benzothioxanthene chromophores as heavy-atom-free small-molecule photosensitizers for photodynamic therapy. *Communications Chemistry* 2022 5:1 2022;5:1–11. <https://doi.org/10.1038/s42004-022-00752-x>.

- [13] Sánchez DP, Morice K, Mutovska MG, Khrouz L, Josse P, Allain M, Gohier F, Blanchard P, Monnereau C, Le Bahers T, Sabouri N, Zagranyski Y, Cabanetos C, Deiana M Demadrille R, Welch GC, Risiko C, Blanchard P, Cabanetos C. Heavy-atom-free π -twisted photosensitizers for fluorescence bioimaging and photodynamic therapy. *J Mater Chem B* 2024;12:8107–21. <https://doi.org/10.1039/D4TB01014K>.
- [14] Josse P, Li S, Dayneko S, Joly D, Labrunie A, Dabos-Seignon S, Allain M, Siegler B, . Bromination of the benzothioxanthene Bloc: toward new π -conjugated systems for organic electronic applications. *J Mater Chem C Mater* 2018;6:761–6. <https://doi.org/10.1039/C7TC05245F>.
- [15] Josse P, Morice K, Puchán Sánchez D, Ghanem T, Boixel J, Blanchard P, Cabanetos C. Revisiting the synthesis of the benzothioxanthene imide five decades later. *New Journal of Chemistry* 2022;46:8393–7. <https://doi.org/10.1039/D2NJ00955B>.
- [16] Kellogg RE, Bennett RG. Radiationless Intermolecular Energy Transfer. III. Determination of Phosphorescence Efficiencies. *J Chem Phys* 1964;41:3042–5. <https://doi.org/10.1063/1.1725672>.
- [17] Galhano J, Kurutos A, Dobrikov GM, Duarte MP, Santos HM, Capelo-Martínez JL, Lodeiro C, Oliveira E. Fluorescent polymers for environmental monitoring: Targeting pathogens and metal contaminants with naphthalimide derivatives. *J Hazard Mater* 2024;480:136107. <https://doi.org/10.1016/J.JHAZMAT.2024.136107>.
- [18] Lodeiro C, Capelo JL, Mejuto JC, Oliveira E, Santos HM, Pedras B, Nuñez C. Light and colour as analytical detection tools: A journey into the periodic table using polyamines to bio-inspired systems as chemosensors. *Chem Soc Rev* 2010;39:2948–76. <https://doi.org/10.1039/B819787N>.
- [19] Galhano J, Marcelo GA, Duarte MP, Oliveira E. Ofloxacin@Doxorubicin-Epirubicin functionalized MCM-41 mesoporous silica-based nanocarriers as synergistic drug delivery tools for cancer related bacterial infections. *Bioorg Chem* 2022;118:105470. <https://doi.org/10.1016/j.bioorg.2021.105470>.
- [20] Marinescu M, Popa CV. Pyridine Compounds with Antimicrobial and Antiviral Activities. *International Journal of Molecular Sciences* 2022, Vol 23, Page 5659 2022;23:5659. <https://doi.org/10.3390/IJMS23105659>.
- [21] Chandak N, Kumar S, Kumar P, Sharma C, Aneja KR, Sharma PK. Exploration of antimicrobial potential of pyrazolo[3,4-b]pyridine scaffold bearing benzenesulfonamide and trifluoromethyl moieties. *Medicinal Chemistry Research* 2013;22:5490–503. <https://doi.org/10.1007/S00044-013-0544-1>.
- [22] Liu H Bin, Tang H, Yang D, Deng Q, Yuan LJ, Ji QG. Synthesis and biological evaluation of novel N-acyl substituted quinolin-2 (1H)-one derivatives as potential antimicrobial agents. *Bioorg Med Chem Lett* 2012;22:5845–8. <https://doi.org/10.1016/J.BMCL.2012.07.08>



TRANSLATIONAL CHEMISTRY

AN INTERFACE JOURNAL

[HTTPS://WWW.TRANSLATIONALCHEMISTRY.COM/](https://www.translationalchemistry.com/)



ORIGINAL ARTICLE | DOI: 10.5584/translationalchemistry.v1i1.238

Practical application of blood microsampling: an effective VAMS-based workflow for anabolic androgenic steroid analysis

Michele Protti ¹, Laura Mercolini ^{1*}, Roberto Mandrioli ²

¹ Research Group of Pharmaco-Toxicological Analysis (PTA Lab), Department of Pharmacy and Biotechnology (FaBiT), Alma Mater Studiorum – University of Bologna, Via Belmeloro 6, 40126 Bologna, Italy; ² Department for Life Quality Studies (QuVi), Alma Mater Studiorum – University of Bologna, Corso d'Augusto 237, Rimini, Italy

Received: March 2025 Accepted: April 2025 Available Online: June 2025

ABSTRACT

Volumetric absorptive microsampling (VAMS) has emerged as a promising alternative to traditional biological sampling methods, offering a high-reliability, field-deployable solution for steroid analysis with practical applications in anti-doping, forensic science and clinical testing. This study presents the optimisation of a VAMS-based workflow for the determination of anabolic androgenic steroids (AAS) in whole blood using high-performance liquid chromatography-tandem mass spectrometry (HPLC-MS/MS). The research primarily focuses on refining microsampling and pretreatment strategies and addressing critical parameters such as volumetric accuracy, extraction efficiency, haematocrit effect mitigation and matrix interference. The workflow assesses both endogenous and exogenous steroids, overcoming limitations associated with traditional venous blood sampling. Experimental evaluations included assessments of sample homogeneity, recovery rates (87-95%), stability over time (up to 30 days) and the impact of haematocrit variability (-7% - +9%) on sampled volume. Strategies for internal standard (IS) addition to VAMS were also optimised to further enhance analytical accuracy. By integrating microsampling with the high reliability of mass spectrometric analysis, this study bridges the gap between laboratory research and practical applications in anti-doping testing, forensic science and clinical bioanalysis. The study provides a validated, cost-effective alternative to traditional sampling methods, confirming that VAMS is a promising minimally invasive tool for steroid detection in whole blood and highlighting its potential for broader applications in translational chemistry and personalised medicine.

Keywords: Microsampling; volumetric absorptive microsampling; anabolic androgenic steroids; HPLC-MS/MS; anti-doping testing

Introduction

The detection of anabolic androgenic steroids (AASs) in sports drug testing remains a crucial challenge due to their widespread misuse for performance enhancement. AASs significantly modify muscle strength, increase the lean-to-fat mass ratio and improve athletic endurance, leading to their strict regulation by the World Anti-Doping Agency (WADA) [1,2]. However, AASs misuse is not limited to professional athletes and recreational users also frequently engage in steroid consumption, raising concerns regarding public health risks and severe physical and psychological side effects [3-5]. Prolonged steroid use has been associated with cardiovascular diseases, hepatic dysfunction, neuropsychiatric disorders and hormonal imbalances [6-9].

Traditional anti-doping tests primarily rely on urine and venous blood analysis using liquid chromatography-tandem mass

spectrometry (HPLC-MS/MS) for steroid determination [10]. While urine sampling remains the preferred matrix due to higher steroid metabolite concentrations and non-invasiveness, in some cases it can present drawbacks such as microbial degradation, storage instability and risk of sample adulteration [11-13]. Blood-based methods offer high selectivity and short detection windows, yet venous blood collection is invasive, logistically complex and requires trained personnel [14-16]. To address these limitations, microsampling techniques such as dried blood spotting (DBS) and volumetric absorptive microsampling (VAMS) have emerged as promising alternatives [17]. DBS has been widely studied for AASs analysis, providing low sample volume requirements, easy transport and storage stability [18-20]. However, DBS can suffer from inherent drawbacks such as the lack of volume control, uneven blood diffusion on the cellulose support and haematocrit (HCT)-dependent volume variability [21].

*Corresponding author: Laura Mercolini, laura.mercolini@unibo.it

VAMS, on the other hand, offers fixed-volume sampling regardless of HCT levels, improved accuracy and enhanced reproducibility [22-24]. These advantages make VAMS a superior choice for AAS analysis in anti-doping applications.

Translational chemistry plays a pivotal role in bridging the gap between fundamental analytical research and its practical applications in real-world scenarios, particularly in the development of innovative bioanalytical tools for anti-doping, forensic sciences and clinical workflows. The ability to translate advances in microsampling technology into robust, field-deployable solutions highlights the interdisciplinary nature of this research, integrating analytical chemistry, clinical applications and regulatory compliance [19,20,25-31]. By refining microsampling techniques such as VAMS, this study contributes to the advancement of sustainable, cost-effective and minimally invasive approaches for steroid detection, directly impacting both elite and amateur sports communities. Recent studies have validated VAMS-HPLC-MS/MS workflows for steroid and glucocorticoid assessment in urine microsamples, demonstrating their applicability in forensic toxicology, endocrinology and doping control [32,33]. While the chromatographic and mass spectrometric parameters for steroid analysis using HPLC-MS/MS are well-established [10,34], additional research is needed to optimise sampling accuracy and precision, analyte extraction, (HCT) independence of sampling and matrix effect evaluation in blood-derived micromatrices.

This study aims to develop and validate an optimised VAMS-based workflow for the analysis of AAS in whole blood, aligning with the principles of translational chemistry by providing a highly applicable and scientifically rigorous solution to real-world doping control challenges, as well as forensic and clinical analysis needs. Five representative AASs have been included, namely: testosterone, nandrolone, stanozolol, methandienone and boldenone (chemical structures in **Figure 1**). Study focus is placed on sampling and

pretreatment optimisation, including volumetric accuracy assessment, solvent extraction efficiency, internal standard (IS) addition strategies and HCT-related interferences, with the final aim of developing and validating a robust, high-throughput microsampling workflow using VAMS for AAS detection in whole blood, overcoming limitations of conventional sampling methods in doping control and clinical analysis. By improving the robustness and reliability of VAMS for AASs testing, its applicability in sports drug testing programs is enhanced, making it a significant contribution to the broader field of translational chemistry.

Materials and Methods

1. Chemicals and solutions

All reagents and solvents used for sample preparation and HPLC-MS/MS analysis were analytical grade. Methanol (MeOH), acetonitrile (ACN), formic acid (FA), ammonium hydroxide and ultrapure water (18.2 M Ω -cm) were obtained from Merck Life Science (Milan, Italy). VAMS devices (30 μ L) were purchased from Trajan Scientific and Medical (Ringwood, Victoria, Australia). AAS certified reference standards, namely testosterone (17 β -hydroxyandrost-4-en-3-one), nandrolone (19-nor-17 β -hydroxyestr-4-en-3-one), stanozolol (17 α -methyl-2'H-androst-2-eno(3,2-c)-pyrazol-17 β -ol), methandienone (17 β -hydroxy-17 α -methylandrosta-1,4-dien-3-one) and boldenone (17 β -hydroxyandrosta-1,4-dien-3-one) and their respective isotopically labelled ISs were obtained from LGC Standards (Teddington, UK). Stock solutions (1 mg/mL) were prepared in MeOH and stored at -20°C when not in use. Working solutions of AASs and ISs were freshly diluted in water/ACN (50:50, v/v) with 0.1% FA before analysis. All solutions were stored in amber glass vials certified for mass spectrometry (Waters, Milford, MA, USA) and kept protected from light.

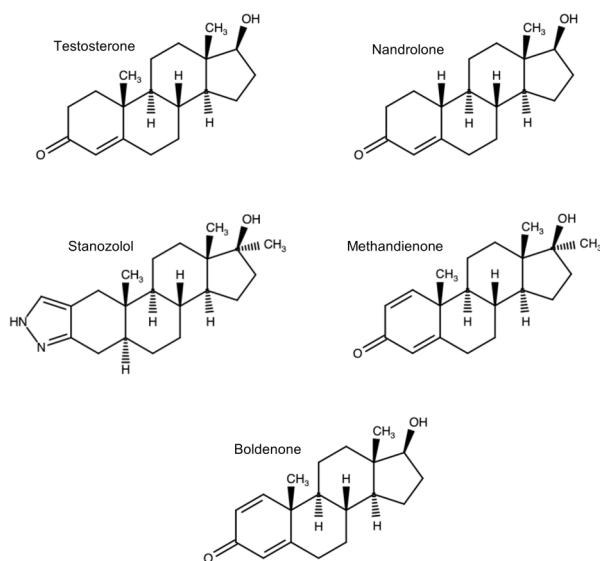


Figure 1 | Chemical structures of the five anabolic androgenic steroids analysed in this study.

2. HPLC-MS/MS method

The HPLC-MS/MS conditions followed those previously established for VAMS-based steroid analysis in urine microsamples, ensuring consistency in chromatographic and mass spectrometric parameters [25]. Chromatographic separation was performed using a Raptor C18 column (50×2.1 mm, $2.7 \mu\text{m}$; Restek, Bellefonte, PA, USA), equipped with a C18 guard column (5×2.1 mm, $2.7 \mu\text{m}$). The mobile phase consisted of 0.1% formic acid in water (Solvent A) and 0.1% formic acid in ACN (Solvent B). The gradient elution program was as follows: 0.0–1.5 min: 30% B (hold); 1.5–3.0 min: 30% to 70% B; 3.0–10.0 min: 70% B (hold); 10.0–12.0 min: 70% to 30% B (re-equilibration); 12.0–15.0 min: 30% B (hold). The flow rate was set at $300 \mu\text{L}/\text{min}$ and the injection volume was $10 \mu\text{L}$. Mass spectrometric detection was performed using electrospray ionisation (ESI) in positive mode. The ion spray voltage was set at 4.00 kV and the source temperature was maintained at 120°C . Other settings included: desolvation temperature: 150°C ; desolvation gas flow: $750 \text{ L}/\text{h}$ (nitrogen); collision gas: argon. The mass spectrometer operated in multiple reaction monitoring (MRM) mode, monitoring specific precursor-to-product ion transitions for each analyte and IS. A full list of MRM transitions, cone voltage and collision energy values is reported in **Table 1**.

This analytical method had been validated for the determination of endogenous and exogenous AASs [25], with the following key performance indicators: limit of detection (LOD) $\leq 0.5 \text{ ng}/\text{mL}$, limit of quantitation (LOQ) $\leq 1.5 \text{ ng}/\text{mL}$, precision as relative standard deviation (%RSD) $\leq 7.6\%$ and absolute recovery ($>77.1\%$).

3. Whole blood collection and handling

Fluid whole capillary blood was collected by means of a Winnoz (New Taipei City, Taiwan) Haiim device. After pricking a fingertip with a disposable lancet, the pricked fingertip was placed on the designated device inlet. Once powered up, the device draws up to $500 \mu\text{L}$ of blood through the inlet and into a anticoagulant-coated

blood collection microtube by vacuum activity.

4. VAMS collection and pretreatment

The miniaturised sampling strategy and pretreatment protocol developed during this experimental work was tested by using whole blood drawn from six healthy volunteers. Aliquots of $30 \mu\text{L}$ of blood were collected by touching the blood surface in the microtube with a VAMS tip, held at a 45° angle and taking care not to completely immerse the tip. The filled VAMS device was left to dry for 45 min at room temperature. When the sample was dry, the tip was detached from the handle and placed in an amber vial, into which $500 \mu\text{L}$ of MeOH were added. The vial was then subjected to ultrasonic assisted extraction (UEA) for 5 min and centrifuged at 4000 RPM for 5 min at 4°C . The supernatant was brought to dryness exploiting a Thermo Fisher Savant SpeedVac SPD 1030 vacuum concentrator and redissolved with $100 \mu\text{L}$ of MeOH.

VAMS were fortified with $30 \mu\text{L}$ of a standard solution containing the analytes at known concentrations. To obtain fortified samples, three different procedures potentially suitable for blood microsampling were studied and namely:

1. Touching the surface of an analyte standard solution with an unused $30 \mu\text{L}$ VAMS tip, leaving it to dry for 45 min and then sampling blood with the same device as described above;
2. Pipetting $30 \mu\text{L}$ of standard solution on an unused VAMS tip, leaving it to dry for 45 min and then sampling blood with the same device as described above;
3. Sampling $30 \mu\text{L}$ of blood with a VAMS as described above, leaving it to dry for 45 min and then touching the surface of a standard solution with the VAMS tip and leaving the tip to dry again.

The obtained fortified blood samples were then subjected to pretreatment and HPLC-MS/MS analysis.

Table 1 | MRM transitions, cone voltage and collision energy for each analyte and IS.

Compound	Parent ion (m/z)	Daughter ion (m/z)	Cone voltage (V)	Collision energy (eV)
Testosterone	289.5	109.2	25	25
Nandrolone	275.0	109.0	25	25
Stanozolol	329.5	81.1	55	31
Methandienone	301.5	121.2	25	25
Boldenone	287.4	121.4	23	30
Testosterone-d3 (IS1)	292.4	112.1	25	25
Nandrolone-d3 (IS2)	278.2	112.0	25	23
Stanozolol-d3 (IS3)	332.5	84.1	55	30
Methandienone-d3 (IS4)	304.4	124.3	23	25
Boldenone-d3 (IS5)	290.4	124.4	25	30

5. VAMS performance assessment

5.1. Volumetric accuracy, repeatability and HCT independence

Blood aliquots at different HCT values in the 20-70% range (namely: 20, 30, 40, 50, 60 and 70%) were sampled by VAMS six times at each HCT value. The mean sampled volume was plotted as a function of HCT value to highlight any volume/HCT variability and possible relationships. Acceptability criterion: $r^2 < 0.5$. Moreover, volume accuracy, expressed as mean percentage volume error and volume repeatability, expressed as percentage relative standard deviation of volumes over six samplings, were obtained at each HCT value. Acceptability criteria: mean RE $\leq \pm 15\%$; RSD $\leq 10\%$.

5.2. Extraction yield

Different extraction procedures of the analytes from VAMS were tested using different solvents, namely: MeOH, ACN, water/MeOH (10/90, 20/80, 30/70) mixtures, water/ACN (10/90, 20/80, 30/70) mixtures, MEOH/ACN (70/30, 50/50, 30/70) mixtures. The samples were subjected to UAE, microwave-assisted extraction (MAE) and vortex-assisted extraction (VAE). Extraction times were tested within the 1-10 min range for UAE, within the 10-180 s range for MAE and within the 30-300 s range for VAE. Acceptability criterion: mean extraction yield $\geq 80\%$.

5.3. Matrix effect

In order to evaluate the extraction procedure effectiveness in analyte purification, IS-corrected matrix effect was evaluated by analysing six blank VAMS replicates, fortified post-extraction by adding known analyte concentrations at three different levels to blank blood VAMS extracts. The mean analyte/IS peak area ratios for each added concentration were compared with analyte/IS peak area ratios from standard solutions at the same theoretical

concentration and the resulting percentage was calculated. Acceptability criterion: response = $100 \pm 15\%$.

5.4. Stability

Short- and medium-term stability of the analytes in the matrix at room temperature (RT) was tested. VAMS samples fortified with two analyte concentrations (a low and a high concentration of the respective calibration curve) were analysed by HPLC-MS/MS at time zero and at set time intervals, corresponding to 1, 7, 14, 20 and 30 days. Subsequently, the analyte concentrations found at each time interval were compared to those found at time zero. For the whole duration of the study, fortified samples were stored at RT, protected from light, heat sources and humidity. Acceptability criterion: mean analyte recovery $\geq 80\%$.

Results and discussion

1. VAMS accuracy and reproducibility

The results of VAMS sampling performance assessment assays (in terms of volumetric accuracy and repeatability) were very satisfactory and are detailed in **Table 2**. As one can see, mean accuracy was well within the $\pm 15\%$ threshold at all HCT values, as was repeatability. For the latter, some HCT dependence is noted, since RSD% becomes higher at extreme HCT values. VAMS demonstrated negligible volume dependency from HCT levels ($R^2 = 0.0051$), confirming its suitability for standardised microsampling across diverse patient populations (**Figure 2**).

2. Optimised extraction and matrix effect

A fast and simple solvent extraction procedure was devised for this analytical workflow. Indeed, more complicated procedures such as solid phase extraction and its variants were deemed unnecessary due to the high selectivity and sensitivity of the HPLC-MS/MS

Table 2 | Evaluation of haematocrit independence of VAMS sampled volume (30 μ L).

Haematocrit value (%)	Mean accuracy (RE%*)	Repeatability (RSD%**)
20	-7	6.3
30	+4	4.7
40	+9	4.1
50	-8	2.2
60	-7	5.5
70	+5	6.4

* RE% = Percent relative error. Calculated as $\frac{V_{\text{actual}} - V_{\text{expected}}}{V_{\text{expected}}} \%$.

** RSD% = Percent relative standard deviation.

Calculated as $\sqrt{\frac{\sum_{i=1}^n (V_i - \bar{V})^2}{(n-1)\bar{V}^2}} \%$.

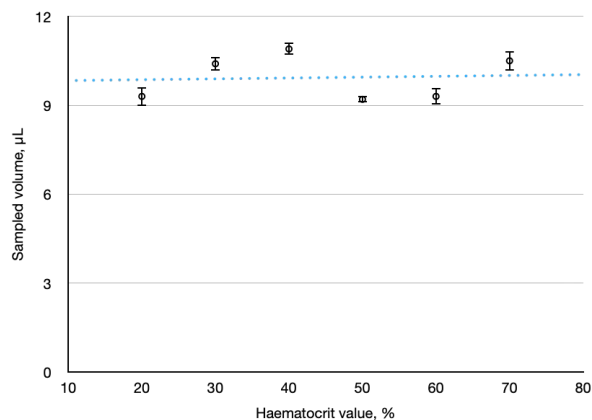


Figure 2 | Haematocrit dependence of sampled volume in VAMS ($R^2 = 0.0051$), demonstrating volumetric stability. The blue dotted line is the least-squares linear regression line.

method and the fact that the very absorption of blood on the polymeric tips constitutes a first sample preparation step, capable of selectively retaining specific matrix compounds and analytes; in a similar way, the extraction procedure from the tip can be likened to a selective elution step of the analytes from a polymeric sorbent. The detailed study of extraction conditions showed that the best procedure involved the use of 500 μL of MeOH and UAE for 5 min. All other solvents and solvent mixtures tested provided either lower extraction yields, or interference, or unacceptably high matrix effect, as detailed in **Table 3**. In a similar way, MAE and VAE

generally produced lower analyte yields than UAE (**Table 3**) and it was ascertained that their combinations did not provide any improvement over simple UAE. Finally, extraction time proved to be critical for method performance, with 5 min (in the case of UAE) being sufficient to reach satisfactory yields and longer times not significantly improving results (**Table 3**). The HPLC-MS/MS chromatogram of a blood VAMS sample fortified with the analytes is shown in **Figure 3**. Peak shape and efficiency are satisfactory, no significant interference is detected and baseline noise is acceptable.

Table 3 | Performance of the main tested extraction conditions.

Solvent	Extraction procedure	Extraction time (s)	Extraction yield range (%)*	Interference	Matrix effect range (% response)*
MeOH	UAE	60	84-90	-	90-95
		300	88-95	-	93-101
		600	87-96	+	78-84
	MAE	10	66-75	-	88-90
		90	67-80	+	80-92
		180	55-89	++	85-95
		30	52-89	+	77-89
		300	54-71	+	76-87
ACN	UAE	60	76-80	+	105-113
		300	70-86	++	104-110
		600	68-79	+++	106-113
	MAE	10	54-66	+++	110-120
		90	61-78	+++	112-119
		180	44-70	++	106-113
		30	42-65	-	90-99
		150	44-78	-	89-95
		300	54-81	+	90-105
MeOH/ACN (50/50)	UAE	60	80-88	+	98-104
		300	85-89	+	99-106
		600	82-87	+	92-99
	MAE	10	70-80	-	99-105
		90	65-79	+	96-106
		180	65-80	++	96-104
	VAE	30	54-67	-	84-94
		150	56-77	+	82-95
		300	49-69	++	83-96

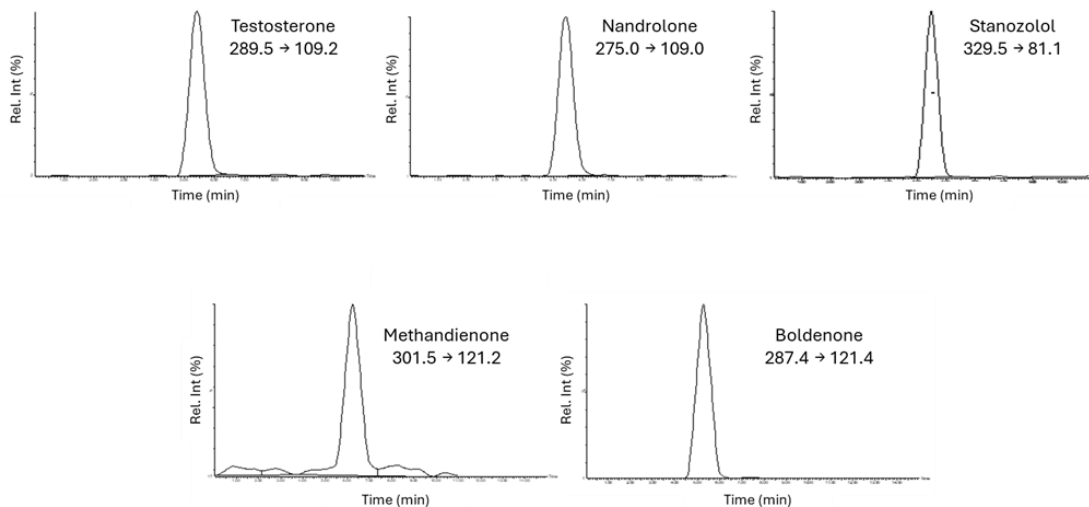


Figure 3 | Representative HPLC-MS/MS MRM chromatograms of a blood VAMS sample fortified with the analytes, showing clear peak separation and lack of interference.

2.1. Internal standard addition

Assays were carried out to find the best procedure for IS addition to VAMS. Three IS addition methods were tested, as described in the 'VAMS collection and pretreatment' Section: IS addition by partial immersion (#1) or by pipetting (#2) before blood VAMS sampling, or by partial immersion (#3) after blood sampling. All three procedures provided reliable results, without significantly negatively impacting analyte determination; no significant differences were found in this respect. Adding ISs after blood sampling (procedure #3) is more convenient, since the subject could use a pristine, sealed VAMS and ISs would be added by the analytical laboratory personnel. While this also means that a potential source of variability (packaging and shipping to the lab) is not accounted for, no manipulation of the devices is needed before sampling, nor until analysis time. On the other hand, standard solution fortification before blood VAMS sampling (procedures #1 and #2) requires the un-sealing of devices before giving them to the subject, so it is suboptimal for anti-doping purposes. Finally, no significant differences were found between fortification by partial

immersion (#1) and by pipetting (#2), however the latter requires some training on pipette use, while the former is easily doable by any subject who is also able to sample blood by VAMS.

2.2. Extraction yield and matrix effect

Three different concentrations were examined, representative of the entire linearity ranges for the different analytes. Average extraction yield values are shown in **Table 4**. These values are the average of six independent analyses.

As can be seen, extraction yields are satisfactory (87-95% range) and similar to what is expected from macroscopic samples. Thus, dried microsampling and extraction does not seem to impair analyte recovery. The combination of microsampling on the polymeric VAMS tip and solvent extraction by MeOH provided sufficient sample clean-up for the declared analytical purpose. In particular, matrix effect response was always in the 93-101% range for all analytes and all concentration levels, as summarised in **Table 5**.

Table 4 | Extraction yield assay results.

Compound	Average extraction yield (%)		
	Low conc. level	Middle conc. level	High conc. level
Testosterone	90	88	87
Nandrolone	89	92	91
Stanozolol	95	95	94
Methandienone	90	91	90
Boldenone	88	88	91

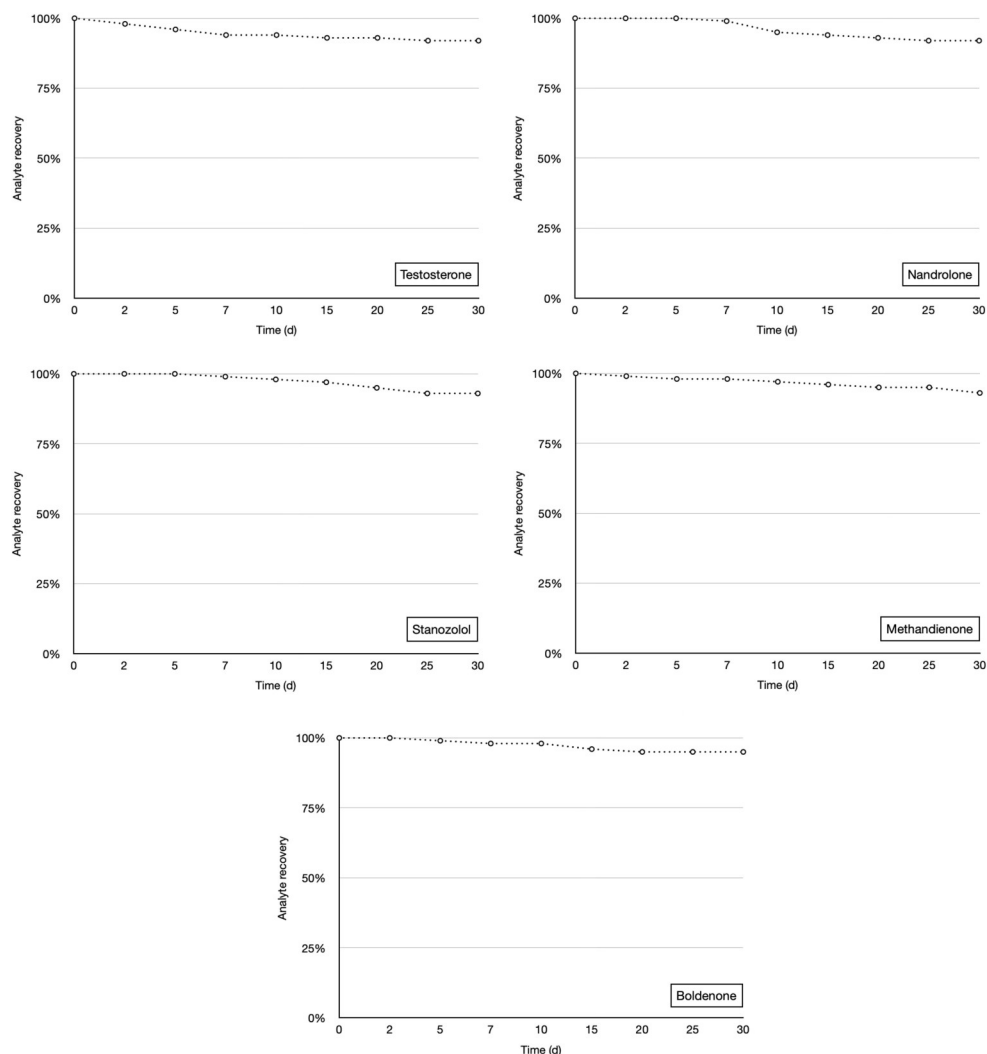
Table 5 | Matrix effect assay results.

Compound	Average matrix effect (%)		
	Low conc. level	Middle conc. level	High conc. level
Testosterone	94	95	94
Nandrolone	100	94	95
Stanozolol	97	93	99
Methandienone	95	95	93
Boldenone	98	100	101

2.3. Stability

Stability was tested for each analyte in VAMS stored for 30 days at RT for comparison with freshly prepared fortified blood VAMS. From the values shown in **Figure 4**, it can be surmised that short-to-medium-term stability of the analytes in the dried matrix is very good (mean analyte recovery $\geq 92\%$). The excellent analyte recovery values obtained underscore that neither analyte degradation nor

“sample aging” happen within the studied timespan. The latter is a potential side effect of microsample drying, where the dried matrix progressively loses over time its capacity to release the analytes due to hardening and loss of wettability. These results confirm that VAMS samples maintain integrity for up to 30 days at room temperature, making them highly suitable for field-based anti-doping programs and remote sample collection in clinical studies.

**Figure 4** | Plots of stability assay results.

3. Comparison with existing sampling methods

The results above prove that VAMS is a mature platform, capable of outstanding volume accuracy and precision results, irrespective of HCT and other confounders. Compared to common venipuncture procedures used for AAS determination, VAMS is surely less invasive (being based on fingerpricking with disposable lancets) and much more error-resistant, leading to the possibility of self-sampling at home, or anyway far from healthcare facilities, by patients or athletes; sampling by non-trained personnel is also possible and feasible. Analyte stability is greatly enhanced in comparison to blood-based fluid matrices, since the latter need frozen storage, while AASs in blood VAMS are stable for at least 30 days at room temperature, also leading to reduced expenses for shipping and storage and reduced space requirements.

4. Real-world applications and limitations

The validated analytical workflow described in this study can be directly translated into real-world applications, especially in the therapeutic drug monitoring (TDM) area and anti-doping frameworks. Moreover, it represents a proof of concept for application to other therapeutic and doping agents in dried blood microsamples, leading the way for a great expansion of the VAMS applicability field. VAMS devices have been designed for straightforward use in automated analytical workflows, so it is conceivable that the procedure presented herein would be easily automated using existing liquid-handling automated instruments, however method performance should be confirmed and validation extended in this regard. The study has a few limitations; it has only been applied to fortified blank blood, thus samples from subjects undergoing pharmacotherapy with AASs, or taking them for any reason, should be analysed and results confirmed before full suitability can be claimed in the anti-doping and forensic spaces. Moreover, just a selection of endogenous and exogenous AASs has been quantified, and for this reason extension of the method to a wider variety of analytes would be advisable for increased applicability. Further assays are underway on both accounts.

Concluding remarks

An innovative method of capillary blood microsampling, based on VAMS, has been developed for the main purpose of anti-doping analysis, with possible applications to forensic and clinical analysis. Dried samples have been shown to be much more convenient than traditional venipuncture: they can be stored for up to 30 days at room temperature without losing more than 8% of their original analyte content. In addition, due to miniaturisation, samples take up much less shelf space and storage equipment and require only minimal amounts of solvents for extraction, making procedures much greener. Finally, analytical VAMS assays have provided ample assurance that this approach provides performances comparable to those typically associated with classical peripheral blood drawing. This translational chemistry study has laid the groundwork for the forthcoming development and optimisation of standardised miniaturised sampling and extraction protocols with

immediate applicability, both for preliminary screening and confirmatory analysis that can be easily implemented by both centralised and local laboratories. It has been carefully developed and optimised to provide possible immediate real-world applications, be they the monitoring and safeguarding of professional and amateur athletes or, in perspective, personalised medicine applications to patients undergoing treatment with AASs.

Acknowledgements

The Authors acknowledge the financial contribution from Alma Mater Studiorum – University of Bologna through Fundamental Oriented Research (RFO) funds.

References

- [1] J.S. Baker, N.E. Thomas, B. Davies, M.R. Graham, *The Open Sports Medicine Journal* 2 (2008) 38e9. DOI: 10.2174/1874387000802010038
- [2] World Anti-Doping Agency (WADA), *The 2025 Prohibited List*. Available online: https://www.wada-ama.org/sites/default/files/2024-09/2025list_en_final_clean_12_september_2024.pdf (accessed on 27 February 2025).
- [3] M. Skrzypiec-Spring, J. Rozmus, G. Abu Faraj, K. Brawańska-Maśluch, K. Kujawa, A. Szeląg, *Journal of Clinical Medicine* 13 (2024) 5892. DOI: 10.3390/jcm13195892
- [4] J. Fink, B.J. Schoenfeld, A.C. Hackney, M. Matsumoto, T. Maekawa, K. Nakazato, S. Horie, *The Physician and Sportsmedicine* 47 (2019) 10–14. DOI: 10.1080/00913847.2018.1526626
- [5] G.D. Albano, F. Amico, G. Cocimano, A. Liberto, F. Maglietta, M. Esposito, G.L. Rosi, N. Di Nunno, M. Salerno, A. Montana, *Healthcare* 9 (2021) 97. DOI: 10.3390/healthcare9010097
- [6] A.L. Baggish, R.B. Weiner, G. Kanayama, J.I. Hudson, M.T. Lu, U. Hoffmann, H.G. Pope Jr., *Cardiovascular toxicity of illicit anabolic-androgenic steroid use*, *Circulation* 135 (2017) 1991–2002. DOI: 10.1161/CIRCULATIONAHA.116.026945
- [7] F. Hartgens, H. Kuipers, *Sports Medicine* 34 (2004) 513–554. DOI: 10.2165/00007256-200434080-00003
- [8] D. Piacentino, G.D. Kotzalidis, A. Del Casale, M.R. Aromatario, C. Pomara, P. Girardi, G. Sani, *Current Neuropharmacology* 13 (2015) 101–121. DOI: 10.2174/1570159X13666141210222725
- [9] E. Nieschlag, E. Vorona, *Reviews in Endocrine and Metabolic Disorders* 16 (2015) 199–211. DOI: 10.1007/s11154-015-9320-5
- [10] R.L. Harries, G. De Paoli, S. Hall, L.A. Nisbet, *WIREs Forensic Science* 6 (2024) e1504. DOI: 10.1002/wfs2.1504
- [11] M. Mazzarino, M.G. Abate, R. Alocci, F. Rossi, R. Stinchelli, F. Molaioni, X. de la Torre, F. Botrè, *Analytica Chimica Acta* 683

- (2011) 221–226. DOI: 10.1016/j.aca.2010.10.003
- [12] M. Tsivou, E. Giannadaki, F. Hooghe, K. Roels, W. Van Gansbeke, F. Garribba, E. Lyris, K. Deventer, M. Mazzarino, F. Donati, D.G. Georgakopoulos, P. Van Eenoo, C.G. Georgakopoulos, X. de la Torre, F. Botrè, *Drug Testing and Analysis* 9 (2017) 699–712. DOI: 10.1002/dta.2048
- [13] R. Mandrioli, R. Di Lecce, M.T. Cartaxo Muniz, W. Taurino De Paula Junior, R. Sardella, L. Mercolini, *Microchemical Journal* 210 (2025) 112940. DOI: 10.1016/j.microc.2025.112940
- [14] R. Faiss, J. Saugy, M. Saugym, *Frontiers in Sports and Active Living* 1 (2019) 30. DOI: 10.3389/fspor.2019.00030
- [15] S. Trinks, K. Braun, A. Gotzmann, E. Bunthoff, D. Mueser, *Drug Testing and Analysis* 16 (2024) 1558–1563. DOI: 10.1002/dta.3679
- [16] M. Thevis, T. Kuuranne, J. Dib, A. Thomas, H. Geyer, *Drug Testing and Analysis* 12 (2020) 704–710. DOI: 10.1002/dta.2790
- [17] M. Protti, E. Milandri, R. Di Lecce, L. Mercolini, R. Mandrioli, *Advances in Sample Preparation* 13 (2025) 100161. DOI: 10.1016/j.sampre.2025.100161
- [18] L. Requena-Tutusaus, I. Anselmo, E. Alechaga, R. Bergés, R. Ventura, *Bioanalysis*. 15 (2023) 1235–1246. DOI: 10.4155/bio-2023-0118
- [19] M. Protti, M.C. Catapano, B.G. Samolsky Dekel, J. Rudge, G. Gerra, L. Somaini, R. Mandrioli, L. Mercolini, *Journal of Pharmaceutical and Biomedical Analysis* 152 (2018) 204–214. DOI: 10.1016/j.jpba.2018.01.043
- [20] M. Protti, J. Rudge, A.E. Sberna, G. Gerra, L. Mercolini, *Journal of Chromatography B* 1044–1045 (2017) 77–86. DOI: 10.1016/j.jchromb.2016.12.038.
- [21] P. Denniff, N. Spooner, *Bioanalysis* 2 (2010) 1385–1395. DOI: 10.4155/bio.10.103
- [22] P.M.M. De Kesel, W.E. Lambert, C.P. Stove, *Analytica Chimica Acta* 881 (2015) 65–73. DOI: 10.1016/j.aca.2015.04.056
- [23] N. Youhnovski, L. Mayrand-Provencher, E.-R. Bérubé, J. Plomley, H. Montpetit, M. Furtado, A. Keyhani, *Bioanalysis* 9 (2017) 1761–1769. DOI: 10.4155/bio-2017-0167
- [24] M. Protti, R. Mandrioli, L. Mercolini, *Analytica Chimica Acta*. 1046 (2019) 32–47. DOI: 10.1016/j.aca.2018.09.004
- [25] R. Mandrioli, L. Mercolini, M. Protti, *Molecules* 25 (2020) 1046. DOI: 10.3390/molecules25051046.
- [26] M. Protti, P.M. Sberna, R. Sardella, T. Vovk, L. Mercolini, R. Mandrioli, *Journal of Pharmaceutical and Biomedical Analysis* 195 (2021) 113873. DOI: 10.1016/j.jpba.2020.113873
- [27] J. Millán-Santiago, R. Vitagliano, F. Modella, R. Mandrioli, R. Sardella, T. Vovk, R. Lucena, S. Cárdenas, F. Boaron, A. Serretti, C. Petio, M. Protti, *Journal of Pharmaceutical and Biomedical Analysis* 236 (2023) 115740. DOI: 10.1016/j.jpba.2023.115740
- [28] M. Protti, I. Varfaj, A. Carotti, D. Tedesco, M. Bartolini, A. Favilli, S. Gerli, L. Mercolini, R. Sardella, *Talanta*. 257 (2023) 124332. DOI: 10.1016/j.talanta.2023.124332
- [29] M. Protti, R. Mandrioli, L. Mercolini. *Perspectives and strategies for anti-doping analysis*. *Bioanalysis*. 2019 Feb;11(3):149–152. DOI: 10.4155/bio-2018-0290
- [30] M. Protti, R. Mandrioli, C. Marasca, A. Cavalli, A. Serretti, L. Mercolini. *Medicinal Research Reviews* 40 (2020) 1794–1832. DOI: 10.1002/med.21671
- [31] S. Palano, D. Turoňova, M. Protti, L. Kujovská Krčmová, R. Sardella, P. Mladěnka, R. Mandrioli, S. Girotti, L. Mercolini, *Microchemical Journal* 203 (2024) 110937. DOI: 10.1016/j.microc.2024.110937
- [32] M. Protti, C. Marasca, M. Cirrincione, A.E. Sberna, R. Mandrioli, L. Mercolini, *Molecules* 25 (2020) 3210. DOI: 10.3390/molecules25143210
- [33] M. Protti, R. Mandrioli, L. Mercolini, *Bioanalysis* 12 (2020) 769–782. DOI: 10.4155/bio-2020-0044.
- [34] A. Wahi, R. Nagpal, S. Verma, A. Narula, R. Kumar Tonk, S. Kumar, *Microchemical Journal* 191 (2023) 108834. DOI: 10.1016/



TRANSLATIONAL CHEMISTRY

AN INTERFACE JOURNAL

[HTTPS://WWW.TRANSLATIONALCHEMISTRY.COM/](https://www.translationalchemistry.com/)



ORIGINAL ARTICLE | DOI: 10.5584/translationalchemistry.v1i1.239

Increasing the potential of enzymatic environmental reactions by applying Tesla valve

Agnieszka Rybarczyk^{1,*}, Malwina Nowak¹, Patrycja Frąckowiak¹, Adam Grzywaczyk¹, Wojciech Smułek¹, Jakub Zdarta^{1,*}

¹Institute of Chemical Technology and Engineering, Faculty of Chemical Technology, Poznan University of Technology, Berdychowo 4, PL-60965 Poznan, Poland

Received: April 2025 Accepted: May 2025 Available Online: June 2025

ABSTRACT

The Tesla valve has been investigated as a potential bioreactor for enzymatic reactions. The reactor obtained through 3D printing was optimized in a colorimetric neutralization reaction of sodium hydroxide with hydrochloric acid and was tested for its ability to facilitate the enzymatic degradation of 17 α -ethynylestradiol (EE2) using laccase. Our study demonstrates the feasibility of utilizing Tesla valves as efficient and cost-effective enzymatic bioreactors for the degradation of pharmaceutical pollutants. The Tesla reactor enables high EE2 degradation efficiency (up to 84%) under optimal flow conditions, offering a sustainable alternative for environmental remediation processes. An additional advantage of using the Tesla valve is its simple design, the absence of mechanical stirrers, and its ability to prevent backflow, contributing to lower operational costs and increased durability. All these findings suggest a high potential for the application of the Tesla valve as a bioreactor in enzymatic processes.

Keywords: Tesla valve, bioreactors, 3D printing, enzymatic reactions, EE2 degradation

Introduction

Modern biocatalysis based on enzyme engineering aimed at improving industrial processes. Enzymes, as efficient and selective catalysts, offer more favorable working conditions in terms of energy efficiency and environmental impact compared to traditional chemical catalysts. Enzyme-catalyzed chemical reactions are not limited to those occurring naturally, enabling new research on the degradation of persistent pollutants and polymers, as well as atom-efficient synthesis of complex biomolecules [1]. Such enzymes include oxidoreductases – biocatalysts that catalyze redox reactions. Due to their wide substrate diversity, they can be applied in various biocatalytic processes through homogeneous and heterogeneous catalysis [2].

Due to the increasing interest in enzymatic processes, a growing number of studies focus on designing these processes and optimizing the selection of reactors has appeared. The choice of the appropriate type of operation carried out in reactors significantly affects reaction efficiency, enzyme stability, and overall process performance [3, 4]. Currently, many different types of biocatalytic reactors are in use. This diversity results from the growing number of enzyme-based processes and modern engineering solutions.

Reactors, depending on their mode of operation and design, can be classified into batch reactors, flow reactors, membrane reactors, and fluidized bed reactors [5]. In a batch reactor, all reagents, including the enzyme and substrate, are loaded into the reactor at the beginning of the process. The reaction proceeds without the addition of fresh substrate or removal of the product until the desired conversion is achieved. Batch reactors are most used in processes involving enzymes in solutions, although immobilized enzymes can also be effectively applied. Typically, the biocatalyst in the form of particles is evenly dispersed in the substrate solution, and mechanical stirrers ensure proper mixing. Batch processes usually require long reaction times [6]. Rather, batch reactors are widely used for producing various products in the chemical and biotechnological industries. Consequently, in recent years, there has been growing interest in optimizing process parameters to maximize economic profit, improve conversion rates, or minimize reaction time [7]. A batch reactor is particularly suitable for products such as pharmaceuticals, polymers, biotechnological products, or other chemical compounds [8].

The use of continuous-flow biochemical reactors is gaining importance in the production of specialty chemicals, pharmaceuticals, biotherapeutics, and biofuels. They also have great

*Corresponding author: Agnieszka Rybarczyk (agnieszka.rybarczyk@doctorate.put.poznan.pl); Jakub Zdarta (jakub.zdarta@put.poznan.pl)

potential for bioanalytical applications [9]. In a flow reactor, substrates are continuously supplied, and products are continuously removed. This type of apparatus operates mainly under steady-state conditions. A key characteristic of a flow reactor is that all reaction parameters depend on the position within the apparatus rather than the reaction time. This type of reactor is used in processes requiring high production efficiency, particularly for fast reactions. Note also that both free and immobilized enzymes can be used in flow reactors [10, 5].

An enzymatic membrane reactor (EMR) is considered a unique apparatus that can simultaneously facilitate both catalytic reactions and product separation, particularly in the hydrolysis of large molecules that enables more cost-effective processes [11]. Membrane reactors integrate membrane separation processes with chemical or biochemical reactions within a single unit. This combination provides higher conversion, improved selectivity, and a compact, cost-efficient reactor design [12]. Membranes in such reactors can be classified into two types: active and passive membranes. In an active membrane, biocatalysts are immobilized, and as substrates pass through their pores, an enzyme-catalyzed reaction occurs. In contrast, a passive membrane functions as a filter that, through appropriate pore size selection, acts as a barrier for catalysts and substrates while allowing only reaction products and solvents to pass through. This system ensures complete separation of substrates and products during the process [5].

A commonly used type of enzymatic reactor is also the fluidized bed reactor (FBR), which can operate continuously. Compared to packed-bed and stirred-tank reactors, fluidized bed reactors are more suitable when substrates are viscous or particulate, as they result in lower pressure losses and a more uniform flow distribution [13-15]. A FBR is a variation of a batch reactor that operates exclusively in an upward-flow mode. The substrate solution is fed from the bottom of the bed at a velocity sufficient to suspend particles, while the pressure drop of the flowing fluid effectively supports the bed's weight. Fluidization can be achieved using either liquids or gases. The main advantage of using a fluidized bed bioreactor is the large specific surface area of the fine-grained packing material. Immobilizing enzymes on the packing particles further separates the residence times of biomass and liquid in the reactor, preventing catalyst washout. This allows for feeding the reactor with a substrate stream at a higher flow rate [8].

In response to the growing demand for more efficient and compact biocatalytic systems, increasing efforts are being made to develop alternative types of reactors. Among them, the Tesla valve stands out as a particularly promising solution. Unlike traditional reactors

that rely on mechanical components or complex flow regulation systems, the Tesla valve enables preferential fluid flow in one direction without the use of moving parts. This unique feature simplifies both the design and operation of the reactor, making it a highly suitable option for continuous-flow enzymatic processes. Integrating biocatalysts within or along the Tesla valve's channels allows for the creation of a compact enzymatic reactor capable of efficiently treating wastewater contaminated with pharmaceutical compounds. In this context, the Tesla valve may offer new perspectives by overcoming many limitations of conventional reactors. Based on these advantages, the present study aimed to utilize and optimize the Tesla valve as an enzymatic reactor for the removal of pharmaceutical pollutants from water streams. The influence of various process parameters on reaction rate and reactor performance was thoroughly investigated and supported by computational modeling to achieve the highest possible removal efficiency.

Material and Methods

Materials and reagents

Sodium hydroxide (98%), hydrochloric acid (37%), bromothymol blue (3',3''-dibromothymolsulfonphthalein), laccase from *Trametes versicolor* (EC 1.10.3.2), and 17 α -ethinyloestradiol (EE2) were received from Sigma-Aldrich. 50 mM acetate buffer pH 5 was freshly prepared.

Reactor fabrication

A model of a flow reactor with a Tesla microvalve was designed using Fusion 360 (Autodesk Inc., USA) and prepared for 3D printing in PrusaSlicer software (Prusa, Czech Republic) using Fused Deposition Modelling technology. The set process parameters are summarised in **Table 1**. Printing was carried out on a Prusa I3 MK3 printer (Prusa, Czech Republic) equipped with a 0.4 mm nozzle, using polylactide (PLA) filaments in white and transparent (Spectrum Filaments, Poland).

Hydrodynamic calculations

In order to determine the dependence of the Reynolds number on the flow rate of the reactant streams, hydrodynamic calculations were made to determine the volumetric flow rate (V'), the averaged flow rate (v), and the apparent flow rate (u), which in turn allowed

Table 1 | Summary of the settings used in the reactor printing.

Parameter	Value
Layer height (mm)	0.1
Filling density (%)	50.0
Nozzle temperature (°C)	208.0
Table temperature (°C)	60.0
Retraction (mm)	2.0
Z-hop (mm)	0.4

the calculation of the averaged (Re_v) and apparent (Re_u) Reynolds number. Calculations were made using equations (1-5):

$$(1) \quad V' = \frac{V_r}{t} \cdot (\text{mL/s})$$

Where: V_r - volume of the reactor (mL), while t - time for the liquid to flow through the reactor (s).

$$(2) \quad v = \frac{l}{t} \text{ (m/s)}$$

Where: l - total length of flow channels (m), and t - time of fluid flow through the reactor (s).

$$(3) \quad u = \frac{L}{t} \text{ (m/s)}$$

Where: L - length of the reactor (m), while t - time for the liquid to flow through the reactor (s).

$$(4) \quad Re_v = \frac{\rho \cdot v \cdot d}{\eta} \text{ (-)}$$

Where: ρ - density of water at 25 °C (kg/m³), v - averaged flow rate (m/s), d - reactor flow diameter (m), and η - water viscosity at 25 °C (Pa*s).

$$(5) \quad Re_u = \frac{\rho \cdot u \cdot d}{\eta} \text{ (-)}$$

Where: ρ - density of water at 25 °C (kg/m³) u - apparent flow rate (m/s), d - reactor flow diameter (m), and η - water viscosity at 25 °C (Pa*s).

Tesla reactor flow study based on the reaction of sodium hydroxide with hydrochloric acid

A reaction between 0.001 M hydrochloric acid and 0.001 M sodium hydroxide in the presence of bromothymol blue, a universal pH indicator, was carried out to investigate the flow characteristics of the reactant streams in the reactor. Eleven experiments were performed, during which the liquid flow through the reactor was monitored at varying flow rates (1, 2, or 3 mL/min). The selection of flow rates was based on preliminary laboratory tests and an analysis of the literature. The process was carried out for 10 minutes following the emergence of the first drop of the reaction mixture from the reactor. During this period, 10 samples were collected at 1-minute intervals. The relationship between the final solution pH and the flow rate of the reactant streams was assessed by measuring pH at 0, 5, and 10 minutes. The samples were subsequently analyzed using UV-Vis spectroscopy in a Jasco V-750 spectrophotometer (Jasco, Japan) over a wavelength range of 280–800 nm.

Study on the degradation of estrogens by free enzymes in a Tesla reactor

The efficiency of enzymatic degradation of estrogens in the Tesla reactor was investigated using a laccase solution (3 mg/mL) and a 17 α -ethynylestradiol solution (0,1 mg/L) prepared in pH 5 acetate buffer. Eleven analogous experiments were conducted at flow rates of 1, 2, or 3 mL/min for each stream, with the residence time of the liquid within the reactor being measured. The reaction proceeded for 10 minutes following the emergence of the first drop of liquid from the reactor, during which 10 samples were collected at 1-minute intervals. The pH of the collected samples was measured at 0, 5, and 10 minutes, followed by analysis via gas chromatography-mass spectrometry (GC-MS). Post-reaction samples were lyophilized using an Alpha 1.4 LD plus lyophilizer (0.36 mbar, -30 °C, 96 h). The resulting residue was resuspended in dimethylformamide (DMF) and transferred to vials. Samples were derivatized by adding N,O-Bis(trimethylsilyl)trifluoroacetamide (BSTFA) with 1% trimethylchlorosilane (TMCS) and subsequently heated at 65 °C for 2 hours. The prepared samples were then subjected to chromatographic analysis. Quantitative analysis of the target compounds was performed using a Pegasus 4D gas chromatograph (Leco, USA) equipped with a BPX-5 column (28 m \times 250 μ m \times 0.25 μ m). Helium was employed as the carrier gas. A 1- μ L sample was injected at 250 °C. The chromatographic separation was conducted under programmed temperature conditions: an initial temperature of 80 °C was maintained for 1 minute, followed by an increase of 20 °C/min to 200 °C, then an increase of 8°C/min to 280 °C, with the final temperature held for 3 minutes. The chromatograph was coupled to a mass spectrometer which analyzed the eluent from the column using an ion source operating in positive ion mode. The temperature of the ion source was 250 °C and the energy was 70 eV. Chroma TOF-GC v4.51.6.0 software was used to analyze the data.

Statistical analysis of the results

The results obtained were collated and statistically analyzed using MODDE[®] 12.1 software (Sartorius Stedim Data Analytics, Germany). The analysis was based on the assumption that there were two variables in the experiment performed - the volumetric flow rate of component A and the volumetric flow rate of component B. The responses of the system - the Tesla reactor - on the other hand, were the actual and apparent linear flow velocity (and the Reynolds numbers calculated from them), the pH of the solution at the outlet of the reactor, and the efficiency of the estrogen degradation process. The calculations were performed in post-ANOVA mode based on three independent measurements of each parameter, together with the default values of the analytical parameters suggested by the software developers. The linear model proved to be the most appropriate (compared to the quadratic models tested) and best correlated with the results obtained, maintaining a confidence level of $p < 0.05$. For individual parameters, the linear equations were as follows:

$$pH = 6.823 + 0.075 V'_A + 0.396 V'_B \quad (6)$$

$$EEr = 49.293 + 0.878 V'_A + 29.592 V'_B \quad (7)$$

$$Re_v = 28.578 + 16.358 V'_A + 15.339 V'_B \quad (8)$$

$$Re_u = 11.223 + 6.424 V'_A + 6.023 V'_B \quad (9)$$

Results and Discussion

The concept of the Tesla valve

A Tesla valve, also known as a valve conduit (**Figure 1**), is a passive

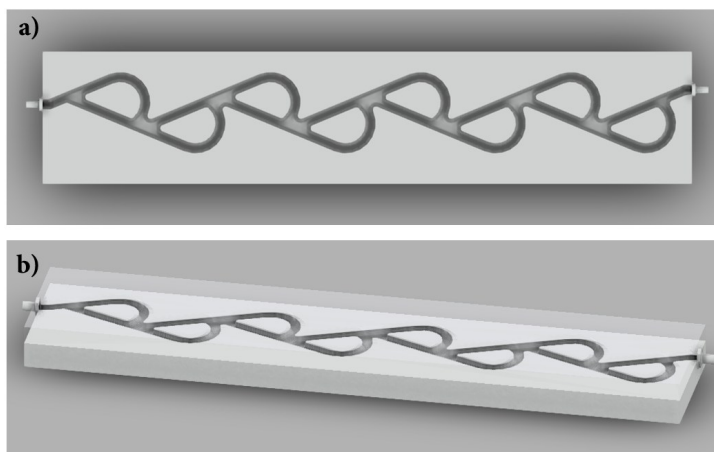


Figure 1 | Reactor design: (a) top view; (b) side view.

The parameters shown in **Table 2** play a key role in the design and operation of the Tesla reactor, influencing its hydraulic properties and lifetime. The length of the reactor indicates a stretched structure, while the width and thickness are significant both for integration into hydraulic systems and for the mechanical strength of the overall structure. The volume of the used reactor, at 2.50 mL, indicates its compactness, which can be important in applications where system size has to be minimized. The flow diameter of the reactor is also a parameter that influences its performance, with a value of 0.25 cm indicating microfluidic operation, where viscous effects and capillary forces play a crucial role. The significant flow length, in turn, suggests an extended flow path, which is characteristic of design designed to increase hydraulic resistance in one direction while minimizing it in the opposite direction. The small flow cross-sectional area of 0.049 cm² limits the space for fluid transport, further enhancing the directional selectivity effect of

non-return valve with a fixed geometry that enables preferential fluid flow in one direction without the need for moving parts. The patent application describes the invention as a conduit with an interior featuring recesses, protrusions, or baffles that impose minimal resistance to fluid flow in the intended direction—aside from surface friction—while creating an almost impassable barrier to flow in the opposite direction. The absence of moving parts significantly enhances the valve's durability, particularly in applications subject to frequent pressure fluctuations [16].

the reactor. The combination of all geometric parameters determines the properties of the Tesla reactor, allowing it to function as a passive check valve [17].

Reynolds number – how flow affect its value

To characterize the operation of the Tesla reactor, it is crucial to determine the Reynolds number and the apparent Reynolds number. This parameter is essential in chemical engineering as it allows for identifying the nature of fluid flow. Through hydrodynamic calculations, the volumetric flow rate (V), the averaged flow rate (v), and the apparent flow rate (u) were determined, enabling the calculation of the Reynolds number and the apparent Reynolds number. This approach allows for establishing the correlation between the Reynolds number and the flow rate of the reactant streams, with the results presented in **Table 3**.

Table 2 | Dimensions of Tesla valve reactor.

Parameter	Value
Length (mm)	196.50
Width (mm)	40.00
Thickness (mm)	8.50
Volume (mL)	2.50
Flow diameter (cm)	0.25
Flow length (cm)	50.93
Flow surface area (cm ²)	0.049
Spigot outer diameter (mm)	4.00
Spigot inside diameter (mm)	1.80
T-piece outside diameter (mm)	5.00
Tee inside diameter (mm)	1.80

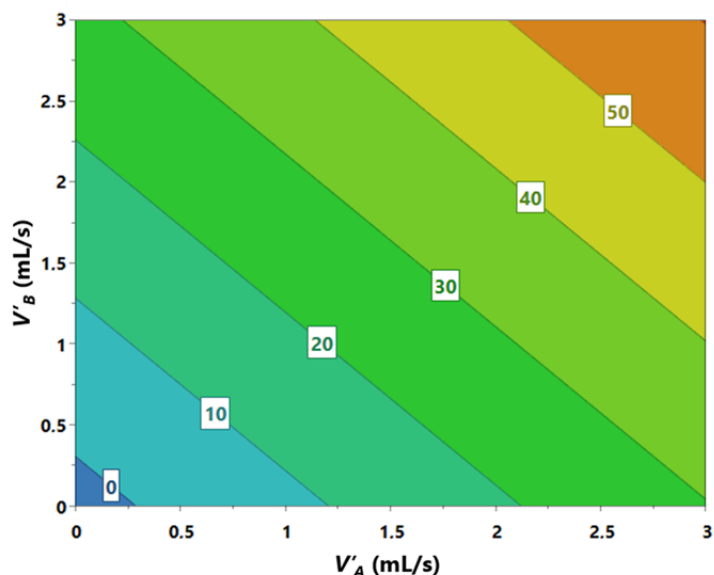
Table 3 | Summary of calculation results for the model reaction of sodium hydroxide with hydrochloric acid.

Experiment number	V' (mL/s)	v (m/s)	u (m/s)	Re_v (-)	Re_u (-)
1	0.015	0.00312	0.00123	8.741	3.433
2	0.015	0.00296	0.00116	8.284	3.253
3	0.033	0.00679	0.00267	18.998	7.460
4	0.052	0.01061	0.00417	29.684	11.657
5	0.048	0.00979	0.00385	27.400	10.760
6	0.060	0.01213	0.00476	33.924	13.322
7	0.061	0.01242	0.00488	34.752	13.647
8	0.074	0.01498	0.00588	41.906	16.457
9	0.093	0.01886	0.00741	52.771	20.723
10	0.081	0.01643	0.00645	45.962	18.049
11	0.114	0.02315	0.00909	64.764	25.433

The obtained values indicate that both Reynolds numbers depend on the flow rates of streams A and B. Both the average Reynolds number (Re_v) and the apparent Reynolds number (Re_u) increase with the rise in the volumetric flow rate. For example, for $V' = 0.015$ mL/s, the values of Re_v and Re_u are 8.741 and 3.433, respectively, whereas for $V' = 0.114$ mL/s, these values increase to 64.764 and 25.433, reaching their maximum values. In all conducted experiments, the values of Re_v and Re_u remain significantly below the transitional flow threshold ($Re < 2100$). These values suggest laminar flow, resulting from the application of relatively low flow velocities. The values of the average Reynolds number are higher than those of the apparent Reynolds number for each analyzed case. This suggests that the average Reynolds number better describes the overall flow characteristics, while the apparent Reynolds number is more sensitive to local variations in flow

parameters. **Figures 2 and 3** show the dependence of the average and apparent Reynolds numbers, respectively, on the flow rates of the acid and hydroxide streams. The graphs indicate that the values of Re_v and Re_u increase as V' increases. For both parameters, the dependence on V' is almost linear, suggesting no sudden changes in the flow characteristics.

The graphs clearly demonstrate that within the examined range, the flow remains laminar, and further increases in flow rate could lead to transitional or turbulent flow. Esterl *et al.*, examined the influence of velocity flow on the catalytic process [18]. Their research was conducted in a different reactor than the Tesla reactor, but they observed the same correlation – the Reynolds number depends on the stream flow rate. Changes in reactor inflow resulted in changes in the Reynolds number, and due to the low velocity, the flow remained laminar.

**Figure 2** | Graph of the dependence of the average Reynolds number on the volumetric flow rate of streams A and B.

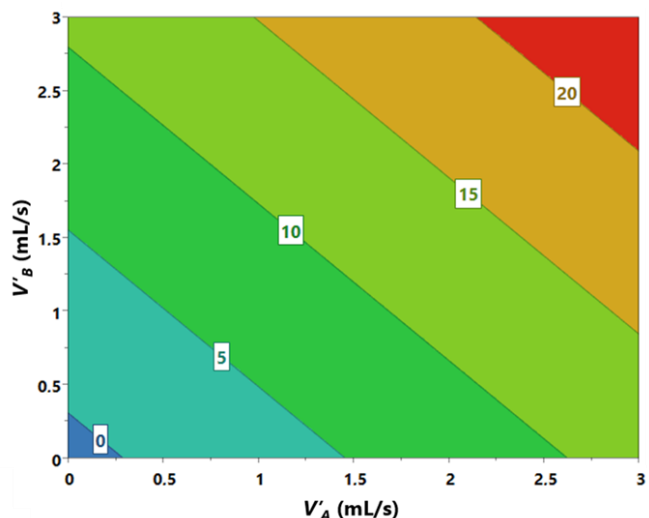


Figure 3 | Graph of the dependence of the apparent Reynolds number on the volumetric flow rate of streams A and B.

Model reaction – how flow affect pH and absorbance

To determine the effect of the flow rate of the reactant streams on the pH of the samples obtained on t , the pH of the samples after leaving the reactor was measured at 0, 5 and 10 min of the process. The results of the measurements are gathered in **Table 4**.

The measurements showed that the pH of the obtained solutions is dependent on the flow rate of the individual streams. A high flow rate of the acid stream causes a shift in the pH value towards an acidic environment, while increasing the ratio of sodium hydroxide flow rate to acid raised the pH of the final solution. However, such changes were observed for experiments with high flow rates whereas for the other experiments, the pH of the solutions remained within the range of a neutral environment. The effect of the flow rate of each stream on the pH of the samples obtained was also analyzed. From **Figure 4** it can be observed that the pH of the samples tested depends mainly on the velocity of stream A,

increasing as the flow rate of the hydroxide increases. In contrast, the effect of the acid stream flow rate on the change in pH of the final solutions was less pronounced.

EE2 removal – how flow affect process duration and removal of estrogens

A key aspect of the research was testing the Tesla reactor in the process of estrogen degradation. Due to its design, the reactor ensures effective mixing of reagents, which enhances the degradation efficiency. Examining the impact of flow parameters on 17 α -ethynylestradiol (EE2) degradation efficiency enables process optimization and assessment of the technology's potential under real-world conditions. The study analyzed the effect of reagent stream flow rates on the duration and efficiency of EE2 degradation. Stream A consisted of an EE2 solution, while stream B contained the laccase enzyme. The flow rates of both streams were

Table 4 | Measured pH values of samples as a function of stream flow rate.

Experiment number	Stream flow rate A (mL/min)	Stream flow rate B (mL/min)	Measured pH		
			$t = 0$ (min)	$t = 5$ (min)	$t = 10$ (min)
1	0	1	8		
2	1	0	4.5		
3	1	1	7	7	7
4	1	2	7	7	6.5
5	2	1	7	7	7
6	2	2	7	7	7
7	1	3	6.5	6.5	6.5
8	3	1	7.5	7	7.5
9	2	3	7.5	6.5	7.5
10	3	2	7.5	7.5	7.5
11	3	3	6.5	7	7

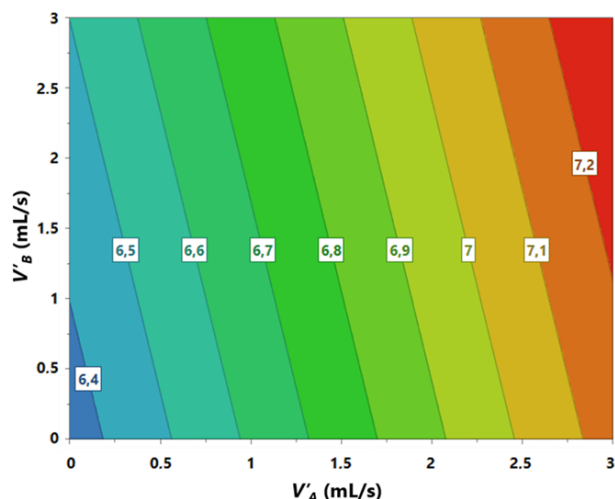


Figure 4 | Graph of the pH dependence of samples on the flow velocity of streams A and B.

varied from 1 mL/min to 3 mL/min, enabling the evaluation of the relationship between these parameters and the effectiveness of estrogen degradation (**Figure 5**).

The graph shows that as the laccase flow rate increases, the degradation efficiency of EE2 rises, reaching a maximum of 84% when the laccase flow rate is three times higher than that of EE2. This indicates that a greater enzyme-to-substrate availability promotes more effective degradation. In contrast, the lowest EE2 removal efficiency, recorded at 38%, was observed when the

opposite flow rate ratio was applied (**Table 5**). These results are consistent with previous studies by Lloret *et al.*, in which, at a high EE2 concentration (4 mg/L) in an enzymatic membrane reactor and under conditions of reduced laccase activity, a removal efficiency of 85% was achieved.

Moreover, no biocatalyst inactivation was observed over 100 hours of operation, and estrogenicity was reduced by 84% [19]. For comparison, in the study conducted by Diório *et al.*, a photocatalytic membrane reactor (UV/H₂O₂/TiO₂) was used,

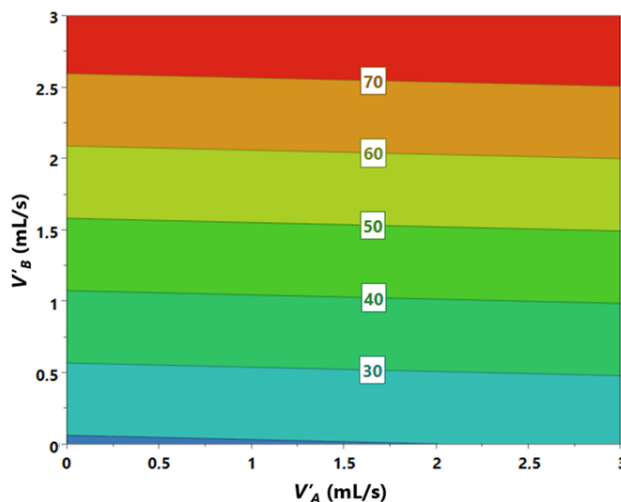


Figure 5 | Graph of the dependence of the estrogen degradation efficiency on the velocity of the reactant streams.

achieving a maximum EE2 degradation rate of 2.9 $\mu\text{M}/\text{min}$ after 7 minutes of operation under optimized conditions (optimal H₂O₂ concentration and pH). These findings confirm the high effectiveness of alternative strategies for micropollutant degradation; however, they require more complex operational conditions, such as UVC irradiation and the use of a heterogeneous catalyst [20].

In the last two experiments, degradation efficiency began to decline at high flow rates. This is likely due to the process duration being too short, leading to insufficient contact between the enzyme and estrogen. The research results indicate that both the flow rate of the streams and the process duration influence the efficiency of

enzymatic estrogen degradation. The degradation time of estrogens depends on the flow rate of both streams. At a flow rate of 1 mL/min, the degradation process lasted 163 and 172 seconds, respectively. A sixfold increase in flow rate reduced reaction duration by over eight times (from 163 seconds to 22 seconds), likely limiting enzyme-substrate interactions and resulting in lower degradation efficiency at higher flow rates.

Furthermore, degradation efficiency analysis shows that the Tesla reactor enables high-efficiency reactions, forming the basis for further research on the apparatus. The Tesla valve not only has potential for EE2 degradation but also for other compounds. As stated in the work of Li *et al.*, the Tesla valve significantly enhances

Table 5 | Summary of the results of the studies on the enzymatic degradation of 17 α -ethynylestradiol.

Experiment number	Stream flow rate A (mL/s)	Stream flow rate B (mL/s)	EE2 removal efficiency (%)
1	0	1	0
2	1	0	0
3	1	1	75
4	1	2	79
5	2	1	61
6	2	2	76
7	1	3	84
8	3	1	38
9	2	3	73
10	3	2	49
11	3	3	58

the degradation rate of VOCs by a photocatalyst [21]. This system enables faster elimination of compounds such as toluene and formaldehyde. During the experiment, 97% degradation of toluene was achieved within 130 minutes and of formaldehyde within 175 minutes. These results are repeatable within a temperature range of 10 °C to 30 °C, indicating the stability of the system under various conditions. Such an application of the Tesla valve could serve as a foundation for developing modern purification methods that effectively remove unwanted compounds and minimize their negative impact on the environment.

Concluding remarks

All obtained results confirm that an enzymatic reaction for the degradation of organic contaminants can be efficiently carried out in a reactor based on the Tesla valve structure. The study demonstrated that reaction efficiency primarily depends on the flow rate of the laccase stream through the reactor, with the highest degradation rate of 17 α -ethynylestradiol, reaching 84%, achieved when the enzyme flow rate was three times higher than that of the estrogen. It was also observed that high flow rates of both streams negatively affected the efficiency of laccase, which was attributed to an excessively short reaction and contact time. Hydrodynamic calculations further allowed for the determination of the flow type within the reactor showing the maximum recorded values were 64.764 for the averaged Reynolds number and 25.433 for the apparent Reynolds number, indicating that the system remained in the laminar regime. Additionally, an analysis of the relationship between pH and flow rate revealed that a high flow rate ratio of acid to hydroxide led to a shift in pH towards the acidic range, whereas the opposite scenario resulted in an alkaline pH. However, such phenomena were only observed at high flow rates, while in all other cases, the pH of the samples remained at 7. All obtained results provide a foundation for further studies on systems utilizing this type of apparatus, as its industrial application could offer significant economic benefits. The absence of moving parts that could wear out or fail, the elimination of the need for mechanical stirrers, the

simplicity of fabrication, and the backflow-preventing design—particularly crucial for low flow rates—would undoubtedly contribute to reducing the operational costs of the reactor in industrial settings. Furthermore, the practical implications of these findings are substantial. The reactor's simple construction and ease of manufacturing via 3D printing not only streamline the production process but also allow for rapid prototyping and adaptation to various industrial requirements. This versatility makes the Tesla valve reactor a promising candidate for large-scale applications in chemical and biotechnological industries, especially in wastewater treatment and pollutant removal processes where cost efficiency and reliability are paramount. The demonstrated balance between reaction efficiency and operational cost underlines the potential of this technology to revolutionize industrial practices in the field of enzymatic degradation.

Acknowledgements

This work was supported by National Science Center Poland, as research project no. DEC 021/43/B/ST8/01854. This work also was supported by the Ministry of Science and Higher Education, Poland through a subsidy to Poznan University of Technology, research number 0912/SBAD/2511.

References

- [1] Reisenbauer, J. C., Sicinski, K. M., & Arnold, F. H. (2024). Catalyzing the future: Recent advances in chemical synthesis using enzymes. *Current Opinion in Chemical Biology*, 83, 102536.
- [2] Cárdenas-Moreno, Y., González-Bacerio, J., García Arellano, H., & del Monte-Martínez, A. (2023). Oxidoreductase enzymes: Characteristics, applications, and challenges as a biocatalyst. *Biotechnology and Applied Biochemistry*, 70, 2108–2135.
- [3] Mojto, M., Horváthová, M., Kiš, K., Furka, M., & Bakošová, M.

- (2021). Predictive control of a cascade of biochemical reactors. *Acta Chimica Slovaca*, 14(1), 51–59.
- [4] De Santis, P., Meyer, L.-E., & Kara, S. (2020). The rise of continuous flow biocatalysis – fundamentals, very recent developments and future perspectives. *Reaction Chemistry and Engineering*, 5(12), 2155–2184.
- [5] Katoh, S., Horiuchi, J.-i., & Yoshida, F. (2015). *Biochemical Engineering*. Wiley-VCH Verlag GmbH & Co. KGaA, Boschstr. 12, 69469 Weinheim, Germany.
- [6] Poppe, J. K., Fernandez-Lafuente, R., Rodrigues, R. C., & Ayub, M. A. Z. (2015). Enzymatic reactors for biodiesel synthesis: Present status and future prospects. *Biotechnology Advances*, 33(5), 511–525.
- [7] Grubecki, I. (2010). Optimal temperature control in a batch bioreactor with parallel deactivation of enzyme. *Journal of Process Control*, 20(5), 573–584.
- [8] Aziz, N. (2002). Optimal operation policies in batch reactors. *Chemical Engineering Journal*, 85(2-3), 313–325.
- [9] Hajba, L., & Guttman, A. (2016). Continuous-flow biochemical reactors: Biocatalysis, bioconversion, and bioanalytical applications utilizing immobilized microfluidic enzyme reactors. *Journal of Flow Chemistry*, 6(1), 8–12.
- [10] Britton, J., Majumdar, S., & Weiss, G. A. (2018). Continuous flow biocatalysis. *Chemical Society Reviews*, 47(15), 5891–5918.
- [11] Sitanggang, A. B., Drews, A., & Kraume, M. (2021). Enzymatic membrane reactors: Designs, applications, limitations and outlook. *Chemical Engineering and Processing - Process Intensification*, 108729.
- [12] Algieri, C., Coppola, G., Mukherjee, D., Shammas, M. I., Calabro, V., Curcio, S., & Chakraborty, S. (2021). Catalytic Membrane Reactors: The Industrial Applications Perspective. *Journal of Catalysis*, 11(6), 691.
- [13] Ching, C. B., & Chu, K. H. (1988). Modelling of a fixed bed and a fluidized bed immobilized enzyme reactor. *Applied Microbiology and Biotechnology*, 29(4), 316–322.
- [14] Bódalo, A., Gómez, J. L., Gómez, E., Bastida, J., & Máximo, M. F. (1995). Fluidized bed reactors operating with immobilized enzyme systems: Design model and its experimental verification. *Enzyme and Microbial Technology*, 17(10), 915–922.
- [15] Fidalgo, W. R. R., Ceron, A., Freitas, L., Santos, J. C., & Castro, H. F. (2016). A fluidized bed reactor as an approach to enzymatic biodiesel production in a process with simultaneous glycerol removal. *Journal of Industrial and Engineering Chemistry*, 38, 217–223.
- [16] Patent #: US001329559. United States Patent and Trademark Office. Office of the Chief Communications Officer, 2017.
- [17] Mohammadzadeh, K., Kolahdouz, E. M., Shirani, E., & Shafii, M. B. (2013). Numerical study on the performance of Tesla type microvalve in a valveless micropump in the range of low frequencies. *Journal of Micro-Bio Robotics*, 8(3-4), 145–159.
- [18] Esterl, S., Özmütlu, Ö., Hartmann, C., & Delgado, A. (2003). Three-dimensional numerical approach to investigate the substrate transport and conversion in an immobilized enzyme reactor. *Journal of Biotechnology and Bioengineering*, 83(7), 780–789.
- [19] Lloret, L., Eibes, G., Moreira, M. T., Feijoo, G., & Lema, J. M. (2013). Removal of Estrogenic Compounds from Filtered Secondary Wastewater Effluent in a Continuous Enzymatic Membrane Reactor. Identification of Biotransformation Products. *Environmental Science & Technology*, 47(9), 4536–4543.
- [20] Diório, A., Bergamasco, R., & Vieira, M. F. (2024). Performance of tube-in-tube membrane microreactor in E2/EE2 degradation via UV/H₂O₂/TiO₂ process. *Desalination and Water Treatment*, 100852.
- [21] Li, X., Cao, L. N. Y., Zhang, T., Fang, R., Ren, Y., Chen, X., Bian, Z., & Li, H. (2024). Optimizing photocatalytic performance in an electrostatic-photocatalytic air purification system through integration of triboelectric nanogenerator and Tesla valve. *Nano Energy*, 128, 109965.



TRANSLATIONAL CHEMISTRY

AN INTERFACE JOURNAL

[HTTPS://WWW.TRANSLATIONALCHEMISTRY.COM/](https://www.translationalchemistry.com/)



ORIGINAL ARTICLE | DOI: 10.5584/translationalchemistry.v1i1.241

Enhancing Luminescent Solar Concentrators with Aggregation-Induced Emission Fluorophores: Overcoming ACQ for Efficient Light Harvesting in PMMA Films

Antonino Oliveri¹, Alberto Picchi¹, Qiuli Zhao², Jing Zhi Sun², Marco Carlotti^{1,*}, Andrea Pucci^{1,3}, Ben Zhong Tang⁴, Tarita Biver^{1,3,*}

¹ Dipartimento di Chimica e Chimica Industriale, Università di Pisa, Via Moruzzi 13, 56124 Pisa, Italy. ² Department of Polymer Science and Engineering, Zhejiang University, Hangzhou 310027, China. ³ INSTM, Udr Pisa, Via Moruzzi 13, 56124 Pisa, Italy. ⁴ School of Science and Engineering, The Chinese University of Hong Kong, Shenzhen (CUHK-Shenzhen), Guangdong 518172, China

Received: March 2025 Accepted: April 2025 Available Online: June 2025

ABSTRACT

The development of efficient and stable luminescent solar concentrators (LSCs) requires fluorophores with high photoluminescence quantum yield (QY), minimal self-absorption, and robust solid-state performance. In this work, we investigate the optical properties and device performance of a red-emitting, aggregation-induced emission (AIE)-active fluorophore, [N,N'-dicyclohexyl-1,7-bis(4'-(1',2',2'-triphenyl)vinyl)phenylperylene-3,4:9,10-tetracarboxylic bisimide] (1,7-DTPEPBI), embedded in poly(methyl methacrylate) (PMMA) thin films. The dye was characterized in solution and polymer matrices, revealing excellent absorption characteristics and AIE behavior in solvent/non-solvent mixtures. In PMMA films, 1,7-DTPEPBI displayed concentration-dependent fluorescence, with a maximum QY of 37% at 0.4 weight % and a red-shifted emission ideal for LSC applications. LSC devices were fabricated using solution-cast PMMA films doped with the dye at varying concentrations. Optical characterization showed an internal photon efficiency (η_{hint}) up to 29% and minimal self-absorption losses, confirmed by P_0 values close to 0.9. Despite lower external photon efficiency (η_{ext}) and device efficiency (η_{dev}) compared to benchmark fluorophores, the AIE-active 1,7-DTPEPBI demonstrated potential as a solid-state emitter for thin-film LSCs, especially in configurations requiring reduced dye reabsorption and good long-term photostability.

Keywords: Luminescent solar concentrators, aggregation-induced emission, poly(methyl methacrylate), optical efficiencies, device efficiency.

Introduction

The global transition toward renewable energy sources has driven extensive research into solar energy harvesting technologies. Among these, luminescent solar concentrators (LSCs) have gained significant attention as cost-effective alternatives to traditional photovoltaic (PV) panels [1,2]. LSCs consist of transparent waveguiding slabs embedded with high-quantum-yield fluorophores that absorb sunlight and re-emit it at longer wavelengths [3]. Through total internal reflection (TIR), the emitted photons are guided toward the edges of the slab, where photovoltaic cells convert them into electricity. Compared to conventional PV modules, LSCs offer lightweight, scalable, and versatile solutions that integrate well with building-integrated photovoltaics (BIPV), enabling applications in windows, facades,

and urban energy harvesting systems [4,5]. A crucial component of LSC efficiency is the selection of high-performance fluorophores capable of absorbing a broad portion of the solar spectrum while exhibiting high fluorescence quantum yield (QY), minimal self-absorption, and long-term photostability [6]. Traditional organic fluorophores such as perylene derivatives, rhodamines, and coumarins have been widely used due to their strong absorption, tunable emission, and high solubility in polymer matrices [7]. However, a major limitation of many organic fluorophores is aggregation-caused quenching (ACQ) – a phenomenon where molecular aggregation leads to non-radiative relaxation, drastically reducing fluorescence efficiency in solid-state applications [8]. This effect is particularly detrimental for LSCs, where high dye loading is often required to maximize light absorption. To address this challenge, fluorophores exhibiting aggregation-induced emission

*Corresponding author: Dr. Marco Carlotti, Email: marco.carlotti@unipi.it | Prof. Tarita Biver, E-mail: tarita.biver@unipi.it

(AIE) have emerged as promising candidates for next-generation LSCs [9]. Unlike conventional fluorophores that experience ACQ, AIE-active materials are non-emissive in dilute solutions but exhibit strong fluorescence upon aggregation due to the restriction of intramolecular motions (RIM) [10,11]. This mechanism effectively suppresses non-radiative decay channels, enabling bright emission in the solid state. Among the most studied AIE-active compounds are tetraphenylethylene (TPE) derivatives, which have demonstrated enhanced stability, minimal self-absorption, and excellent processability in polymer matrices [12–16].

Recent studies have demonstrated the successful incorporation of AIE luminogens into poly(methyl methacrylate) (PMMA) films for LSC applications [17–20]. PMMA remains the benchmark polymer matrix for LSCs due to its high optical transparency, chemical resistance, and compatibility with a wide range of fluorophores [21]. In particular, TPE-based fluorophores have been widely investigated for their ability to maintain high fluorescence efficiency under concentrated conditions, effectively mitigating aggregation-caused quenching (ACQ). Among them, several donor–acceptor TPE derivatives, such as TPE-MRh [22] and TPE-BPAN [23] have demonstrated aggregation-induced emission (AIE) behavior, red-shifted emission, and promising quantum yields when embedded in polymer matrices. These red-emitting TPE systems have shown excellent compatibility with PMMA and have enabled long-term photostability and efficient light harvesting in both thin-film and bulk LSC architectures. Such characteristics make them ideal candidates for enhancing the performance and durability of next-generation luminescent solar concentrators

In this study, the fluorophore [N,N'-dicyclohexyl-1,7-bis(4'-(1',2',2'-triphenyl)vinyl)phenylperylene-3,4:9,10-tetracarboxylic bisimide] (1,7-DTPEPBI) (**Figure 1A**) [24], was selected for its dual structural advantage: it merges the strong light-harvesting and red-emitting properties of perylene bisimides (PBIs) with the AIE behavior of the TPE units. The specific substitution at the bay position of the perylene core with TPE moieties is designed to suppress the detrimental π – π stacking interactions typical of PBIs, which are known to cause fluorescence quenching in the solid state. At the same time, the presence of TPE enables AIE, ensuring that fluorescence is activated upon aggregation, as occurs in polymer matrices and thin films. This tailored molecular design was conceived to retain high photoluminescence efficiency under the concentrated and condensed conditions typical of LSCs, while minimizing reabsorption losses and enhancing photostability. Compared to other TPE-based AIEgens, 1,7-DTPEPBI also offers extended spectral coverage in the red region and improved compatibility with PMMA, making it a particularly suitable candidate for solid-state light-harvesting applications (**Figure 1B**) [25,26]. This study investigates the optical and photovoltaic performance of this AIE-active red-emitting fluorophore in PMMA-based LSCs. LSCs are evaluated for their light-harvesting capabilities, fluorescence quantum yield, and resistance to photodegradation under prolonged solar exposure with the aim to demonstrate the feasibility of AIE-based materials in enhancing the sustainability and efficiency of LSC technology.

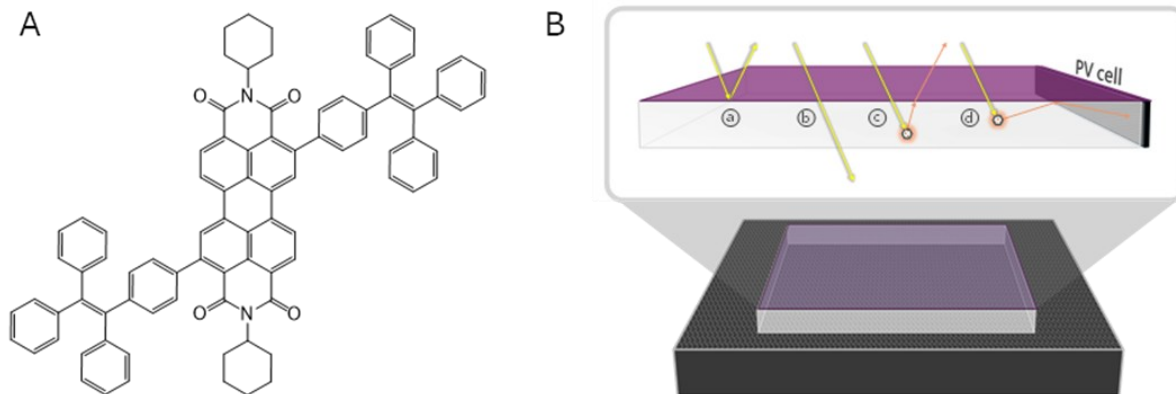


Figure 1 | (A) Molecular structure of [N,N'-dicyclohexyl-1,7-bis(4'-(1',2',2'-triphenyl)vinyl)phenylperylene-3,4:9,10-tetracarboxylic bisimide] (1,7-DTPEPBI); (B) Interactions of photons within an LSC. In particular: a) reflection; b) transmission; c) photon losses by outward refraction; d) emitted photon reaching the PV cell on the LSC edge.

Material and Methods

Materials

The [N,N'-dicyclohexyl-1,7-bis(4'-(1',2',2'-triphenyl)vinyl)phenylperylene-3,4:9,10-tetracarboxylic bisimide] (1,7-DTPEPBI, **Figure 1A**) was synthesized in a previous work [24]. The molar concentration of the dye will be indicated as CD. Poly(methyl methacrylate) (PMMA) was from Merck, average Mw ~350,000 by GPC, density 1.17 g/mL at 15.0 °C.

All solvents used in present work were the ultrapure reagent: acetone (ACS reagent, > 99.5%, Merck); acetonitrile (HPLC-GOLD-Ultragradient Grade, Carlo Erba); chloroform (Spectrophotometric Grade, > 99.5%, Alfa Aesar); hydrochloric acid (ACS reagent, 37%, Merck); diethylether (ACS reagent, ≥99.8%, Merck); dimethylsulfoxide (≥99.9%, Merck); ethanol (≥99.8%, Merck); hexane (for HPLC, ≥97.0%, Merck); methanol (Spectrophotometric Grade, 99.8+%, Alfa Aesar); tetrahydrofuran (ACS reagent, > 99.9%, Honeywell or Spectrophotometric Grade, 99.7+%, Alfa Aesar); toluene (Spectrophotometric Grade, 99.7+%, Alfa Aesar).

Methods

Preliminary solubilization tests (0.5 mg in 1.5 mL solvent) showed that 1,7-DTPEPBI is insoluble in acetone, acetonitrile, diethyl ether, dimethylsulphoxide, hexane and methanol. It is, instead, soluble in chloroform, tetrahydrofuran (THF) and toluene which were thus chosen for the characterization in solution of the dye. Stock solutions of the dye in each of the solvents were done by weight. In brief, 2-3 mg of 1,7-DTPEPBI (MW = 1251.5 g/mol) were added to 1.0 mL of solvent (chloroform, THF or toluene). These mother solutions (ca. 2 mM) were diluted either with the same solvent or with the appropriate solvent/non-solvent mixtures (v/v%) to obtain working solutions for both UV-vis and fluorescence experiments. For the solution spectra, UV-vis data were collected using a Perkin-Elmer Lambda 650 spectrophotometer. Absorption spectra were recorded in the wavelength range from 200 nm to 800 nm, using slit width 2 nm, spectral resolution 1 nm, integration time 0.2 s; quartz cuvettes of the “macro” type (minimum volume 1000 μL), with an optical path of 1.0 cm, were used. In the experiments at different concentrations, increasing amounts of the working solutions were added directly in the spectrophotometric cuvette by means of a Hamilton micro-syringe connected to a Mitutoyo micrometric screw (1 turn = 8.2 μL). An Agilent Technologies Cary 5000 Series UV-Vis-NIR spectrophotometer was used for the spectrophotometric characterization of the polymeric matrices. The polymer films were housed in a solid sample holder and three absorption spectra were recorded, one at the center and two at the edges.

Spectrofluorimetric measurements were done on a Perkin Elmer LS55 instrument, using semi-micro cuvettes (minimum volume 500 μL) with an optical path of 1.0 cm. Fluorescence spectra were recorded by exciting at different absorption maxima and emission wavelength range typically from λ_{ex} to 800 nm, using slit widths both 3 nm, spectral resolution of 1 nm, integration time of 0.5 s. In the experiments at different concentrations, increasing amounts of the working solutions were added directly in the spectrofluorimetric cuvette by means of the already cited Hamilton micro-syringe. In the case of the polymeric films, the fluorescence tests used a Horiba Jobin Yvon FluoroLogR-3 instrument. The polymer films were analyzed using the solid sample holder and placing the detector in front-face mode (30°, FF) to avoid the

interference of scattered light. The quantum yield measurements performed on the solid-state samples were obtained using a 152 mm diameter Quanta-phi integrating sphere, coated in Spectralon® and positioned on the optical path of the Horiba Jobin Yvon FluoroLogR-3 spectrofluorometer.

The LSC was fabricated on a high-purity optical glass substrate measuring 50.0 \times 50.0 \times 3.3 mm, specifically an Edmund Optics BOROFLOAT® window (50 \times 50 mm, TS grade). This glass is maintained in 6 N HCl for one night, then rinsed with water, acetone and ethanol. To prepare the solution to be cast, 60.0 mg of polymer were mixed with a known quantity of chloroform solution containing the fluorophore to obtain a mixture at a known weight % in the 0.2-2.0% range. The mixture is made up to 1.5 mL volume and shaken to ensure solubilization. This latter mixture is thus dropped on the glass following a solution casting procedure. The films were left to dry for 24 h, then detached from the glass support by immersion in Ultra-Pure water. The film thickness was controlled by Rupac-Digitronic micrometer with 0-25 mm measuring range, 0.001 mm resolution and \pm 4 μm precision. The surface of the polymer films, still adhered to the preparation glass, was investigated by an LED epifluorescence microscope from AUXILAB S.L., code HBF002, connected to a 2.3 Mega Pixel Invenio 2EIII camera and a personal computer equipped with the DeltaPix InSight software. The images were acquired working both in transmission and epifluorescence.

Results and discussion

Solution studies

To thoroughly investigate the optical properties of 1,7-DTPEPBI in solution, we performed UV-Vis absorption and fluorescence measurements in three selected solvents (chloroform, THF, and toluene) and in different solvent/non-solvent systems in which the dye was dispersed. **Figure 2** shows the absorbance profiles of 1,7-DTPEPBI in the different solvents. In agreement with the literature, there are four maxima: the two at shorter wavelengths are related to the tetraphenylethylene groups [27,28], while those at lower energies are due to the perylene core [29]. UV-Vis absorption spectra were recorded for different dye concentrations (CD), approximately in the 2×10^{-6} M to 1×10^{-4} M range (**Figure S1**).

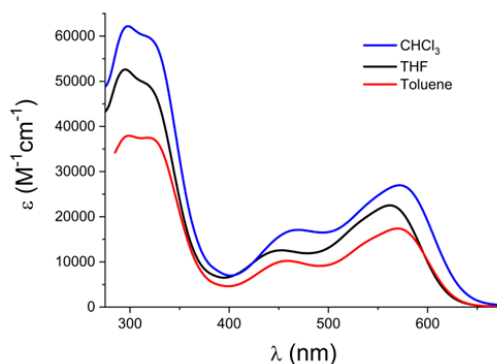


Figure 2 | Absorbance profiles of 1,7-DTPEPBI in different solvents, 25.0 °C.

The shapes do not seem to change with increasing concentrations, as it would have occurred in the presence of auto-association processes.

The absorbance vs. concentration test is done to further inspect any possible aggregation phenomena. Data are analyzed both for linearity (Lambert-Beer plots) (Figure S2) and using the absorbance ratio at two different wavelengths (Figure S3). The latter approach emphasizes also subtle deviations from direct proportionality. None of the experiments done evidenced auto-aggregation effects under the conditions of the experiments. The photophysical parameters are collected in Table 1.

We thus checked the possible light emission characteristics of 1,7-DTPEPBI in the three selected solvents, at a concentration of ca. 1×10^{-6} M and excitation at each of the absorbance maxima. Given that 1,7-DTPEPBI was designed to show AIE characteristics, an absence of fluorescence emission is expected in a good solvent [10]. This was indeed the case for chloroform and THF. On the other hand, the measurements in toluene revealed a signal centered at $\lambda_{\text{MAX,em}} = 630$ nm for $\lambda_{\text{MAX,ex}} = 570$ nm (Figure S4), indicating that the dye molecules are at least partially in the form of an aggregate in hydrophobic solvents [24]. The light emission is proportional to concentration and the limit of detection of 1,7-DTPEPBI in toluene ($\text{LOD} = 3\sigma$ of the blank) is found to be 2.40×10^{-8} M (Figure S5).

The AIE characteristics of 1,7-DTPEPBI were then inspected by dispersing it in different solvent/non-solvent systems. In particular, we considered THF/H₂O, CHCl₃/Hexane, CHCl₃/Methanol and Toluene/Hexane mixtures. The absorption and fluorescence properties of each system were analyzed as the percentage of non-

solvent increased, keeping the dye concentration constant. In agreement with AIE, light emission switches on as the non-solvent content increases. For THF/H₂O (Figure S6), AIE light-on is detectable already at 10% H₂O but significant precipitation occurs for H₂O% $\geq 40\%$. Note that the precipitates are amorphous (the solid does not emit any light) [30]. For CHCl₃/Hexane mixtures (Figure S7) the low polarity of both solvents suppressed precipitation phenomena and enabled to test all the possible compositions of the mixtures; Figure 3A shows the AIE effect for this system. In this more favorable case, we also collected an EEM plot (Figure S8). Switching to CHCl₃/Methanol produced dye precipitation at 70% Methanol and a reduced light switch effect (Figure S9). Finally, in Toluene/Hexane mixtures, 1,7-DTPEPBI started to precipitate at 70% Hexane; as already cited, an emission signal is present also at 0% Hexane, but it further increases with the non-solvent content (Figure S10). Figure 3B collects the variation of the fluorescence signals as a function of the percentage of non-solvent present in solution, comparing the behavior of the different solvent/non-solvent systems. It is interesting to note that the emission band of the highly emissive aggregates formed in CHCl₃/Hexane and Toluene/Hexane (550-750 nm) corresponds to the optimal region for LSC applications (500-850 nm, i.e. the region of maximum photovoltaic efficiency) with a Stokes' shift of ca. 60-65 nm. Differently, THF/H₂O and CHCl₃/Methanol mixtures induce the formation of low emitting species with a signal centered at ca. 520 nm. Overall, CHCl₃ seems the solvent with the better performance.

Table 1 | UV-vis characterization of 1,7-DTPEPBI in different solvents, 25.0 °C. ϵ_r = polarity index; ϵ = molar absorption coefficient (error < 1%).

Solvent	ϵ_r	$\lambda_{\text{MAX,Abs}}$ (nm), ϵ ($10^4 \text{ M}^{-1} \text{ cm}^{-1}$)			
THF	7.5	295, 5.54	323, 5.05	453, 1.27	562, 2.26
CHCl ₃	4.8	298, 6.30	321, 6.01	470, 1.99	572, 2.83
Toluene	2.4	299, 3.99	323, 2.95	458, 1.11	570, 1.89

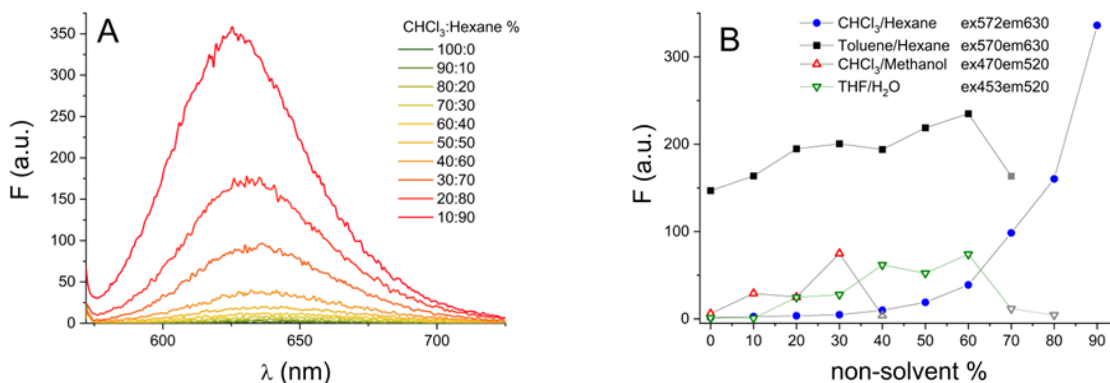


Figure 3 | (A) Fluorescence emission of 1,7-DTPEPBI in different CHCl₃/Hexane mixtures; $C_D = 1.66 \times 10^{-5}$ M, $\lambda_{\text{ex}} = 572$ nm, 25.0 °C. (B) Comparison of fluorescence light on effects at 25.0 °C for the different mixtures considered in this work (normalized at the same 1,7-DTPEPBI content; grey points are those where precipitation occurs).

2. Optical studies in polymeric films

After studying the spectroscopic properties of 1,7-DTPEPBI in solution, we investigated its behavior in polymeric films to evaluate its possible application as fluorescent dopant in luminescent devices. In particular, we employed films of poly(methyl methacrylate) (PMMA) because of its very high clarity and good processability, which makes it an ideal material for the fabrication of optical devices and clear structural components [31].

We prepared several films (thickness of $25 \pm 5 \mu\text{m}$) containing different amounts of dye, from 0.2 weight % (wt.%) to 2 wt.%, via solution casting (**Figure 4A**). The films appeared clear, with a purple coloration, and emitted red fluorescence upon exposure under UV light (366 nm; **Figure 4B**).

The absorption properties of 1,7-DTPEPBI in PMMA films closely resembled that of the dye in solution, with the most red-shifted featuring a λ_{MAX} of 564 nm and a shoulder centered at about 465 nm; conversely, we found that the fluorescence of the dye in the film was significantly different from the examples reported above in solution (**Figure 5A**). To start, the emission maximum in PMMA was red-shifted, resulting in larger Stokes shifts in this system. These latter ranged from about 99 nm, with respect to the absorption peak at 564 nm, in the case of the film with the lowest dye concentration (0.2 wt.%) and increased up to 135 nm in the case of the one with the highest (2 wt.%). The reason behind this variation in the Stokes shift with concentration is not only due to inner filter effects but also to a change in the shape of the emission profile. At low 1,7-DTPEPBI concentrations, the emission peak is symmetric and centered at about 660 nm, similar in shape to those observed in solution. This suggests that, even at the lowest concentration tested, the dye either forms emissive aggregates in the chosen PMMA matrix or that its motion is sufficiently restricted to have a significant emission. Upon investigation via fluorescence microscopy, it is possible to observe the presence of irregular aggregates of different dimensions (20-150 μm diameter) randomly distributed within the matrix, which emitted

red radiation (**Figure 4C**) throughout the concentration range tested. Nevertheless, no evidence of fluorophore segregation at the surface was observed.

As the quantity of 1,7-DTPEPBI in the film increased, a new peak appeared centered at about 700 nm. The AIE behavior of the investigated dye was noticeable even in the polymer matrix, with the maximum emission intensity increasing dramatically going from 0.2 wt.% to 0.8-1.0 wt.%. At higher concentrations, the intensity decreased again, most likely due to self-absorption phenomena and to the formation of amorphous aggregates. In these latter, fluorescence is inherently lower due to the less dense packing, which increases the intermolecular distance, making the side chains more mobile and more likely to dissipate energy through vibrational and rotational motions.

Figure 5B reports the photoluminescence quantum yield (QY) of 1,7-DTPEPBI in PMMA for the different concentrations. In particular, it was found to decrease constantly from $37 \pm 4 \%$ in the case of the less concentrated film to $10 \pm 1\%$ for the 2.0 wt.% one, suggesting the formation of amorphous, poorly luminescent aggregates, as indicated by fluorescence microscopy images. This could be related to the fact that perylene bisimides still experience progressive quenching of their emissions in PMMA, likely due to self-aggregation and energy transfer processes, notwithstanding the presence of TPE moieties at the bay positions. On the other hand, Lumogen Red in PMMA films exhibits remarkable QY stability across the entire concentration range investigated, confirming its superior resistance to aggregation-induced quenching effects [32]. The QY values for 1,7-DTPEPBI were found to be considerably lower than those of highly performing ACQ fluorophores, such as Lumogen F Red 305 (LR305) [33], benzobisthiazoles [34], benzodithiophenes [35], and quinoxalines [36,37], prepared and measured in similar conditions. However, the measured QY at a 1,7-DTPEPBI concentration of 0.4 wt.%, i.e. $37 \pm 4\%$, is higher or comparable to that of similar AIE or AIEE systems already investigated in LSC applications [22,23,38].

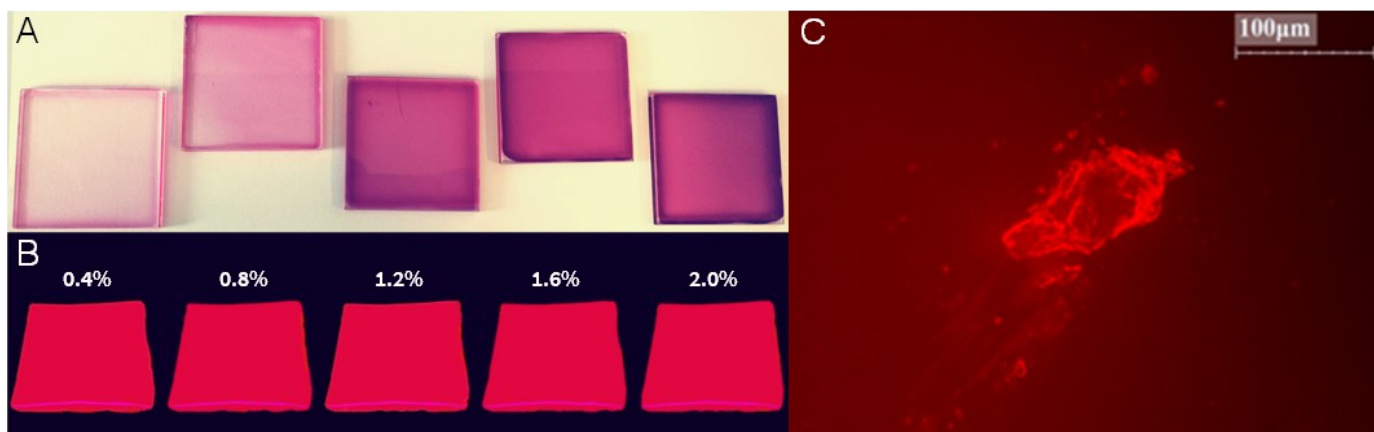


Figure 4 | Films (5×5 cm) of 1,7-DTPEPBI dispersed in PMMA; (A) under natural light; (B) under 366 nm illumination. (C) Epifluorescence microscopy image of 1,7-DTPEPBI/PMMA thin films at 0.4 wt.%.

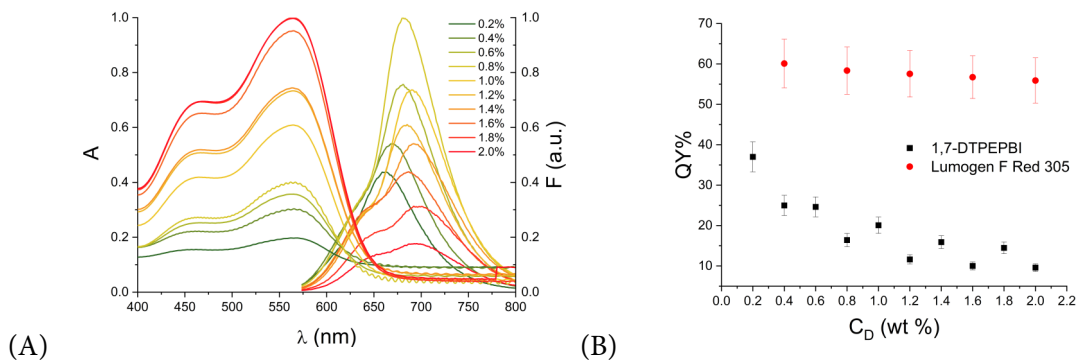


Figure 5 (A) Absorbance and fluorescence emission profiles of 1,7-DTPEPBI in PMMA; $0.2\% \leq C_D \leq 2.0$ wt.%; $\lambda_{ex} = 564$ nm. (B) Quantum yield percent (QY%) for 1,7-DTPEPBI in PMMA ($\lambda_{ex} = 564$ nm); data for the same films with Lumogen F Red 305 ($\lambda_{ex} = 575$ nm) are also shown for comparison.

Luminescent solar concentrators (LSCs) based on 1,7-DTPEPBI

Despite the non-optimal QY of the dye, we conducted further tests on PMMA films doped with 1,7-DTPEPBI to evaluate its performance as emitter in thin-film LSCs compared to previously investigated AIEgens [23,38–42]. These tests help determine whether aggregation-induced emission (AIE) effects can be effectively exploited in solid-state PMMA matrices, despite the quenching observed at higher dye concentrations. To do so, we prepared via solution casting a series of $5 \times 5 \times 0.4$ cm LSC devices comprising thin PMMA films at different dye concentrations (0.5–2.0 wt.%) and evaluated their performances in terms of internal photon efficiency (η_{int}), representing the fraction of absorbed photons which is emitted from the edges of the device, external photon efficiency (η_{ext}), the fraction of incident photons which is emitted from the edges, and, finally, device efficiency (η_{dev}), the ratio between the incident power and the power originating from a PV module coupled to the edge of the LSC. As shown in **Figure 6A**, the internal photon efficiency, η_{int} , decreases with increasing concentration, from a value of $29 \pm 2\%$ at 0.4 wt.% to $12 \pm 2\%$ at 2.0 wt.%. This result is consistent with QY and with the formation of low-emission aggregates. Although a small concentration range of AIE occurrence, which was previously shown from 0.4 to 0.8% wt., the highest QY is observed at 0.4 wt.%. This may indicate a simultaneous formation of highly emitting aggregates, due to the AIE effect, and non-emitting amorphous aggregates, caused by

ACQ. However, the decline in η_{int} is less substantial with increasing concentration compared to QY, indicating a minimal occurrence of self-absorption, a phenomenon that is generally detrimental to the efficiency at extended photon optical paths. An estimation of self-absorption losses was provided by Wilson *et al.* [43]. Following the detailed procedure and considering as reabsorption-free an edge-emission spectrum acquired when exciting at a point close to the edge, we calculated P_0 , i.e. the probability of photons nonsuffering self-absorption. As shown in **Table S1**, P_0 is approximately constant at ≈ 0.9 across the concentration range examined. This suggests that self-absorption has a limited impact, even at high fluorophore loadings. This outcome can be attributed to the thin-film configuration, which, although necessitates higher concentrations (by approximately 100 times), has a reduced volume of doped polymer, while the light-guiding effect is predominantly exerted by the glass substrate. Consequently, for most of the optical path, the emitted photons pass through the non-absorbing glass. The external photon efficiency, η_{ext} , increased with concentration until it reached almost constant values at around 2.2% (**Figure 6B**). These performances were found to be considerably lower than those of the benchmark fluorophores, with roughly a quarter of the efficiency of LR305, and also lower than the $\approx 3.4\%$ calculated for recently investigated TPE-based emitters [23,40]. This decline can be attributed to the significant QY decrease from 0.8 wt.% onwards.

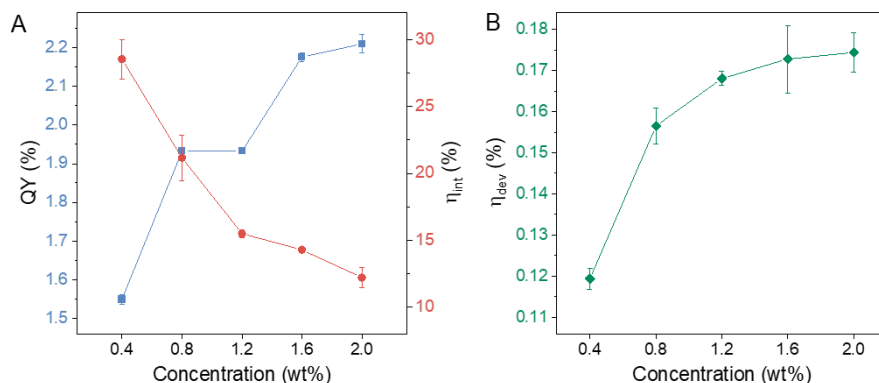


Figure 6 | (A) Quantum yield percent (QY%) and internal photon efficiency (η_{int}) for 1,7-DTPEPBI in PMMA; (B) External photon efficiency (η_{ext}) and electrical device efficiency (η_{dev}) for thin-film LSCs containing 1,7-DTPEPBI.

Concurrently, the electrical device efficiency, η_{dev} , exhibited an analogous trend to η_{ext} , increasing with concentration. η_{dev} was derived from J-V curve acquisitions without the application of a reflective tape on the edges. This approach enables the calculation of low values, which can be multiplied by 4 to simulate the scenario where solar cells are placed on all four sides [44]. Consequently, for a four-side collection configuration, $\eta_{\text{dev},4 \text{ sides}} = 0.70\%$. Although not directly comparable with previous literature data acquired with reflective tape on the uncovered edges, this determination is helpful to estimate the real power production of an LSC-PV system. It is important to note that only through a device scale-up reliable power production measurements can be obtained simulating real-world conditions. Nevertheless, data on photon efficiencies can be readily utilized for cross-laboratory comparisons, as outlined in the widely accepted LSC laboratory protocols [45].

Concluding remarks

This study explored the integration of a novel red-emitting fluorophore, 1,7-DTPEPBI, combining perylene bisimide and tetraphenylethylene moieties, into PMMA matrices for the fabrication of efficient luminescent solar concentrators (LSCs). Designed to exhibit aggregation-induced emission (AIE) behavior, 1,7-DTPEPBI demonstrated good solubility in selected organic solvents and excellent photostability. Spectroscopic analyses in solution confirmed the absence of aggregation-caused quenching (ACQ) and the activation of AIE properties under specific solvent/non-solvent conditions. When embedded in PMMA films, 1,7-DTPEPBI exhibited significant, red-shifted fluorescence and AIE-driven luminescence, although the quantum yield (QY) decreased at higher concentrations due to the formation of low-emissive, amorphous aggregates. Nevertheless, LSC devices fabricated with these films achieved promising optical performances. The optimal internal photon efficiency (η_{int}) was observed at 0.4 wt.% dye loading, with values progressively decreasing at higher concentrations due to partial quenching. Importantly, self-absorption losses were found to be minimal, as confirmed by high P_0 values across the concentration range. While external photon efficiency (η_{ext}) and device efficiency (η_{dev}) were lower than those achieved with benchmark fluorophores like Lumogen F Red 305, the results demonstrate the potential of AIE-based fluorophores as viable, structurally tunable alternatives for solid-state light-harvesting applications. The combination of photostability, controlled emission, and low self-absorption in thin-film configurations underscores the relevance of these systems in the ongoing development of cost-effective and scalable LSC technologies. Future work will focus on the structural optimization of AIE-active fluorophores to enhance QY at higher loadings, the exploration of new polymeric matrices with reduced aggregation tendencies, and device scaling to validate real-world photovoltaic performance.

Acknowledgements

This research is supported by PON 2014-2020 “Research and Innovation” resources – Green/Innovation Action – DM MUR

1061/2022. We also acknowledge financial support under the National Recovery and Resilience Plan (NRRP), Mission 4, Component 2, Investment 1.1, Call for tender No. 104 published on 2.2.2022 by the Italian Ministry of University and Research (MUR), funded by the European Union – NextGenerationEU – Project Title Luminescent solar Concentrators based on recycled methyl methacrylate and Eco-compatible materials (LUCE) CUP I53D23004190006 Codice progetto: 2022ZZC2HZ by the Italian Ministry of University and Research (MUR).

References

- [1] N. Aste, L.C. Tagliabue, C. Del Pero, D. Testa, R. Fusco, *Renew. Energy* 76 (2015) 330–337. DOI: 10.1016/j.renene.2014.11.026
- [2] W.G.J.H.M. Van Sark, *EPJ Web Conf.* 33 (2012) 0–7. DOI: 10.1051/epjconf/20123302003
- [3] S. Castelletto, A. Boretti, *Nano Energy* 109 (2023) 108269. DOI: 10.1016/j.nanoen.2023.108269
- [4] B.S. Richards, I.A. Howard, *Energy Environ. Sci.* 16 (2023) 3214–3239. DOI: 10.1039/D3EE00331K
- [5] F. Meinardi, F. Bruni, S. Brovelli, *Nat. Rev. Mater.* 2 (2017) 17072. DOI: 10.1038/natrevmats.2017.72
- [6] J. Roncali, *Adv. Energy Mater.* 10 (2020) 2001907. DOI: 10.1002/aenm.202001907
- [7] L. Beverina, A. Sanguineti, in: *Sol. Cell Nanotechnol.*, Wiley, 2013, pp. 317–355. DOI: 10.1002/9781118845721.ch13
- [8] E. Tatsi, A. Nitti, D. Pasini, G. Griffini, *Nanoscale* 16 (2024) 15502–15514. DOI: 10.1039/D4NR01910E
- [9] J. Xu, M.H. Chua, B.Z. Tang, eds., *Aggregation-Induced Emission (AIE)*, Elsevier, 2022. DOI: 10.1016/C2020-0-01478-7
- [10] Y. Hong, J.W.Y. Lam, B.Z. Tang, *Chem. Commun.* (2009) 4332–4353. DOI: 10.1039/b904665h
- [11] J. Luo, Z. Xie, Z. Xie, J.W.Y. Lam, L. Cheng, H. Chen, C. Qiu, H.S. Kwok, X. Zhan, Y. Liu, D. Zhu, B.Z. Tang, *Chem. Commun.* 18 (2001) 1740–1741. DOI: 10.1039/b105159h
- [12] N. Guidugli, R. Mori, F. Bellina, B.Z. Tang, A. Pucci, in: *Princ. Appl. Aggregation-Induced Emiss.*, Springer International Publishing, Cham, 2019, pp. 335–349. DOI: 10.1007/978-3-319-99037-8_14
- [13] T.A. Geervliet, I. Gavrila, G. Iasilli, F. Picchioni, A. Pucci, *Chem. - An Asian J.* 14 (2019) 877–883. DOI: 10.1002/asia.201801690
- [14] G. Lyu, J. Kendall, I. Meazzini, E. Preis, S. Bayseç, U. Scherf, S.

- Clément, R.C. Evans, *ACS Appl. Polym. Mater.* 1 (2019) 3039–3047. DOI: 10.1021/acsapm.9b00718
- [15] F. Yang, X. Ye, G. Chen, J. Xiao, Z. Wu, Y. Luo, W. Zheng, W. Zhou, L. Wang, B. Lu, Y. Wei, Z. Yang, Z. Chi, X. Dong, *Compos. Part B Eng.* 219 (2021) 108898. DOI: 10.1016/j.compositesb.2021.108898
- [16] H. Wang, Q. Li, P. Alam, H. Bai, V. Bhalla, M.R. Bryce, M. Cao, C. Chen, S. Chen, X. Chen, Y. Chen, Z. Chen, D. Dang, D. Ding, S. Ding, Y. Duo, M. Gao, W. He, X. He, X. Hong, Y. Hong, J. Hu, R. Hu, X. Huang, T.D. James, X. Jiang, G. Konishi, R.T.K. Kwok, J.W.Y. Lam, C. Li, H. Li, K. Li, N. Li, W. Li, Y. Li, X. Liang, Y. Liang, B. Liu, G. Liu, X. Liu, X. Lou, X. Lou, L. Luo, P.R. McGonigal, Z. Mao, G. Niu, T.C. Owyong, A. Pucci, J. Qian, A. Qin, Z. Qiu, A.L. Rogach, B. Situ, K. Tanaka, Y. Tang, B. Wang, D. Wang, J. Wang, W. Wang, W. Wang, W. Wang, X. Wang, Y. Wang, S. Wu, Y. Wu, (2023). DOI: 10.1021/acsnano.3c03925
- [17] J.L. Banal, B. Zhang, D.J. Jones, K.P. Ghiggino, W.W.H. Wong, *Acc. Chem. Res.* 50 (2017) 49–57. DOI: 10.1021/acs.accounts.6b00432
- [18] J.L. Banal, K.P. Ghiggino, W.W.H. Wong, *Phys. Chem. Chem. Phys.* 16 (2014) 25358–25363. DOI: 10.1039/c4cp03807j
- [19] W. Ma, W. Li, M. Cao, R. Liu, X. Zhao, X. Gong, *Org. Electron.* 73 (2019) 226–230. DOI: 10.1016/j.orgel.2019.06.017
- [20] P. Meti, F. Mateen, D.Y. Hwang, Y.-E. Lee, S.-K. Hong, Y.-D. Gong, *Dye. Pigment.* 202 (2022) 110221. DOI: 10.1016/j.dyepig.2022.110221
- [21] G. Griffini, *Front. Mater.* 6 (2019) 1–8. DOI: 10.3389/fmats.2019.00029
- [22] C. Micheletti, Q. Wang, F. Ventura, M. Turelli, I. Ciofini, C. Adamo, A. Pucci, *Aggregate* 3 (2022) 1–10. DOI: 10.1002/agt2.188
- [23] A. Picchi, Q. Wang, F. Ventura, C. Micheletti, J. Heijkoop, F. Picchioni, I. Ciofini, C. Adamo, A. Pucci, *Polymers (Basel)*. 15 (2023). DOI: 10.3390/polym15173530
- [24] Q. Zhao, S. Zhang, Y. Liu, J. Mei, S. Chen, P. Lu, A. Qin, Y. Ma, J.Z. Sun, B.Z. Tang, *J. Mater. Chem.* 22 (2012) 7387. DOI: 10.1039/c2jm16613e
- [25] A. Nowak-Król, F. Würthner, *Org. Chem. Front.* 6 (2019) 1272–1318. DOI: 10.1039/c8qo01368c
- [26] O. Krupka, P. Hudhomme, *Int. J. Mol. Sci.* 24 (2023). DOI: 10.3390/ijms24076308
- [27] G. Seybold, G. Wagenblast, *Dye. Pigment.* 11 (1989) 303–317. DOI: 10.1016/0143-7208(89)85048-X
- [28] L. Liu, G. Zhang, J. Xiang, D. Zhang, D. Zhu, *Org. Lett.* 10 (2008) 4581–4584. DOI: 10.1021/ol801855s
- [29] C. Li, J. Yum, S. Moon, A. Herrmann, F. Eickemeyer, N.G. Pschirer, P. Erk, J. Schöneboom, K. Müllen, M. Grätzel, M.K. Nazeeruddin, *ChemSusChem* 1 (2008) 615–618. DOI: 10.1002/cssc.200800068
- [30] X. Lou, Y. Yang, *Aggregate* 1 (2020) 19–30. DOI: 10.1002/agt2.1
- [31] M. Zettl, O. Mayer, E. Klampaftis, B.S. Richards, *Energy Technol.* 5 (2017) 1037–1044. DOI: 10.1002/ente.201600498
- [32] A. Picchi, I. Bettini, M. Ilarioni, M. Carlotti, A. Pucci, *RSC Appl. Polym.* 2 (2024) 624–633. DOI: 10.1039/D4LP00067F
- [33] F.J. Ostos, G. Iasilli, M. Carlotti, A. Pucci, *Polymers (Basel)*. 12 (2020) 2898. DOI: 10.3390/polym12122898
- [34] C. Papucci, A. Dessì, C. Coppola, A. Sinicropi, G. Santi, M. Di Donato, M. Taddei, P. Foggi, L. Zani, G. Reginato, A. Pucci, M. Calamante, A. Mordini, *Dye. Pigment.* 188 (2021) 109207. DOI: 10.1016/j.dyepig.2021.109207
- [35] M. Bartolini, C. Micheletti, A. Picchi, C. Coppola, A. Sinicropi, M. Di Donato, P. Foggi, A. Mordini, G. Reginato, A. Pucci, L. Zani, M. Calamante, *ACS Appl. Energy Mater.* 6 (2023) 4862–4880. DOI: 10.1021/acsaem.3c00362
- [36] G. Goti, G. Reginato, C. Coppola, A. Dessì, D. Franchi, A. Mordini, A. Picchi, A. Pucci, A. Sinicropi, L. Zani, M. Calamante, *European J. Org. Chem.* 27 (2024) 1–10. DOI: 10.1002/ejoc.202400112
- [37] C. Papucci, R. Charaf, C. Coppola, A. Sinicropi, M. Di Donato, M. Taddei, P. Foggi, A. Battisti, B. De Jong, L. Zani, A. Mordini, A. Pucci, M. Calamante, G. Reginato, *J. Mater. Chem. C* 9 (2021) 15608–15621. DOI: 10.1039/d1tc02923a
- [38] R. Mori, G. Iasilli, M. Lessi, A.B. Muñoz-García, M. Pavone, F. Bellina, A. Pucci, *Polym. Chem.* 9 (2018) 1168–1177. DOI: 10.1039/C7PY01933E
- [39] A.S. Perera, S. Zhang, S. Homer-Vanniasinkam, M.O. Coppens, M. Edirisinghe, *ACS Appl. Mater. Interfaces* 10 (2018) 15524–15531. DOI: 10.1021/acsaami.8b04774
- [40] F. Corsini, A. Nitti, E. Tatsi, G. Mattioli, C. Botta, D. Pasini, G. Griffini, *Adv. Opt. Mater.* 9 (2021). DOI: 10.1002/adom.202100182
- [41] X. Zheng, Q. Peng, L. Zhu, Y. Xie, X. Huang, Z. Shuai, *Nanoscale* 8 (2016) 15173–15180. DOI: 10.1039/c6nr03599j
- [42] F. De Nisi, R. Francischello, A. Battisti, A. Panniello, E. Fanizza, M. Striccoli, X. Gu, N.L.C. Leung, B.Z. Tang, A. Pucci,

Mater. Chem. Front. 1 (2017) 1406–1412. DOI: 10.1039/c7qm00008a

[43] L.R. Wilson, B.C. Rowan, N. Robertson, O. Moudam, A.C. Jones, B.S. Richards, Appl. Opt. 49 (2010) 1651. DOI: 10.1364/AO.49.001651

[44] C. Yang, H.A. Atwater, M.A. Baldo, D. Baran, C.J. Barile, M.C. Barr, M. Bates, M.G. Bawendi, M.R. Bergren, B. Borhan, C.J. Brabec, S. Brovelli, V. Bulović, P. Ceroni, M.G. Debije, J.-M. Delgado-Sanchez, W.-J. Dong, P.M. Duxbury, R.C. Evans, S.R. Forrest, D.R. Gamelin, N.C. Giebink, X. Gong, G. Griffini, F. Guo, C.K. Herrera, A.W.Y. Ho-Baillie, R.J. Holmes, S.-K. Hong, T.

Kirchartz, B.G. Levine, H. Li, Y. Li, D. Liu, M.A. Loi, C.K. Luscombe, N.S. Makarov, F. Mateen, R. Mazzaro, H. McDaniel, M.D. McGehee, F. Meinardi, A. Menéndez-Velázquez, J. Min, D.B. Mitzi, M. Moemeni, J.H. Moon, A. Nattestad, M.K. Nazeeruddin, A.F. Nogueira, U.W. Paetzold, D.L. Patrick, A. Pucci, B.P. Rand, E. Reichmanis, B.S. Richards, J. Roncali, F. Rosei, T.W. Schmidt, F. So, C.-C. Tu, A. Vahdani, W.G.J.H.M. van Sark, R. Verduzco, A. Vomiero, W.W.H. Wong, K. Wu, H.-L. Yip, X. Zhang, H. Zhao, R.R. Lunt, Joule 6 (2022) 8–15. DOI: 10.1016/j.joule.2021.12.004

[45] M.G. Debije, R.C. Evans, G. Griffini, Energy Environ. Sci. 14 (2021) 293–301. DOI: 10.1039/D0EE02967J

REVIEW



TRANSLATIONAL CHEMISTRY

AN INTERFACE JOURNAL

[HTTPS://WWW.TRANSLATIONALCHEMISTRY.COM/](https://www.translationalchemistry.com/)



REVIEW | DOI: 10.5584/translationalchemistry.v1i1.242

Translational Advances: Biomaterials and Antimicrobial Photodynamic Therapy, a Synergistic Approach

Filipe M. P. Morais^{1,3}, Carlos Lodeiro^{2,3}, Nuno M. M. Moura^{1,*}

¹ LAQV-REQUIMTE, Department of Chemistry, University of Aveiro, 3810-193 Aveiro, Portugal. ² PROTEOMASS Scientific Society, 2825-466, Sto Antonio de Caparica, Costa de Caparica, Portugal. ³ BIOSCOPE Research Group, LAQV-REQUINTE, Chemistry Department, NOVA School of Science and Technology, NOVA University Lisbon, 2829-516, Caparica, Portugal.

Received: April 2025 Accepted: May 2025 Available Online: June 2025

ABSTRACT

The increasing prevalence of drug-resistant pathogens represents a serious public health challenge, driven by factors such as inadequate water sanitation, the misuse and overuse of antimicrobials, and insufficient infection prevention and control measures. Appropriately functionalized porphyrin derivatives present a promising strategy as broad-spectrum photo-antimicrobial agents, activated by visible light in the presence of molecular oxygen throughout photodynamic approach. These compounds effectively target resistant microorganisms, namely bacteria. To mitigate production costs, the immobilization of these compounds on solid supports has been proved essential, as it enables their recovery, reuse, and recycling. This approach enhances both the economic viability and environmental sustainability of antimicrobial photodynamic therapy. Furthermore, various biopolymers, including cyclodextrin, lignin and chitosan, have been employed to immobilize porphyrin-based photosensitizers, allowing for the tailoring of the substrates physicochemical and biological properties.

Keywords: Photosensitizers, porphyrins, photodynamic therapy, biopolymers, immobilization.

Introduction

Antimicrobial resistance is a major global health challenge that impacts individuals at all stages of life and has significant repercussions for healthcare, veterinary medicine, and agriculture. Key contributing factors include poor sanitation, limited access to clean water, inadequate infection prevention and control measures, and the improper use of antimicrobials. Consequently, there is an urgent need to create affordable and innovative treatments to combat drug-resistant pathogens [1–3]. Antimicrobial Photodynamic Therapy (aPDT) leverages the interaction of light, a photosensitizer (PS), and molecular oxygen to eliminate microorganisms. Upon absorbing light, the PS transitions to an excited state, initiating a series of energy transfers that ultimately leading to the generation of reactive oxygen species (ROS), namely singlet oxygen (1O_2) [4,5]. These ROS are highly cytotoxic and effectively damage microbial cells. The process involves the PS absorbing light, moving through various excited states, and potentially undergoing intersystem crossing to a longer-lived triple state. This extended lifetime enhances energy transfer to molecular oxygen, leading to the generation of ROS. aPDT harnesses light to activate a PS, generating a targeted and localized oxidative attack

against microorganisms [6–8]. This process oxidizes various cellular components, leading to rapid cell photoinactivation. aPDT offers advantages over traditional antimicrobials because it does not promote the development of resistance. Its ability to target multiple cellular sites, inflicting damage on various structures through ROS-induced oxidative stress, this extensive damage makes it difficult for microorganisms to develop resistance by altering a single target. Moreover, aPDT typically acts promptly, with microbial death occurring soon after treatment. This rapid action minimizes the selective pressure on microorganisms, unlike prolonged exposure to antibiotics, which provides more opportunities for resistant strains to emerge and multiply [4,5]. The effectiveness of photodynamic action in aPDT is largely determined by the structure of the PS and its capacity to generate ROS. Directing PS to specific subcellular locations, can amplify its phototoxic effects while minimizing harm to surrounding healthy tissues. The design of a PS also influences its biocompatibility and the likelihood of side effects. Ideally, a PS should exhibit minimal toxicity toward healthy cells while delivering potent cytotoxic effects to target cells. Although various organic compounds have been explored as PS in aPDT, porphyrins and related macrocycles are at the forefront of PS research. There is considerable interest in synthesizing

*Corresponding author: Nuno M. M. Moura, E-mail: nmoura@ua.pt

porphyrins and their derivatives because of their unique properties, which are applicable in biomedicine, catalysis, and advanced materials. In the context of PS for aPDT, porphyrins exhibit distinctive characteristics such as chemical versatility, stability under light and during storage, strong absorption in the visible spectrum, efficient photoinduced reactions with molecular oxygen, low inherent toxicity, and a high binding affinity to cellular components such as membranes, proteins, and DNA [9–11]. The structure of the cell wall in Gram-positive and Gram-negative bacteria plays a crucial role in determining their sensitivity to aPDT. In general, PS molecules readily attach to Gram-positive bacteria, resulting in their photoinactivation. In contrast, Gram-negative bacteria tend to be more resistant to PS treatment due to their intricate cell wall structure. The presence of negatively charged lipopolysaccharides enhances the interactions with cationic PS, which can influence the treatment's overall effectiveness [12]. This review aims to provide a concise and comprehensive overview of recent advancements in the immobilization of porphyrin-based PS, particularly focusing on the use of various biopolymeric supports such as cyclodextrins,

chitosan, and lignin, for developing cost-effective and environmentally friendly photoactive materials.

1. Preparation of cyclodextrin-porphyrin hybrids

Cyclodextrins (CD) are cyclic oligosaccharides composed of glucose units derived from starch through enzymatic conversion. The three most common types of CD are α (alpha), β (beta), and γ (gamma), which consist of six, seven, and eight glucose units, respectively, arranged in a ring fashion (Figure 1). The central cavity of a CD molecule can encapsulate guest molecules, including hydrophobic substances such as neutral porphyrins, making them valuable for various applications. Additionally, these complexes can protect the encapsulated molecules from external environmental factors. One of the main fields application of CD is in the pharmaceutical field, where they enhance the solubility and stability of poorly water-soluble drugs, thereby improving their effectiveness [13–15]. The use of CD in aPDT shows significant potential for improving the field by tackling important issues related to the formulation and delivery of PS [16,17].

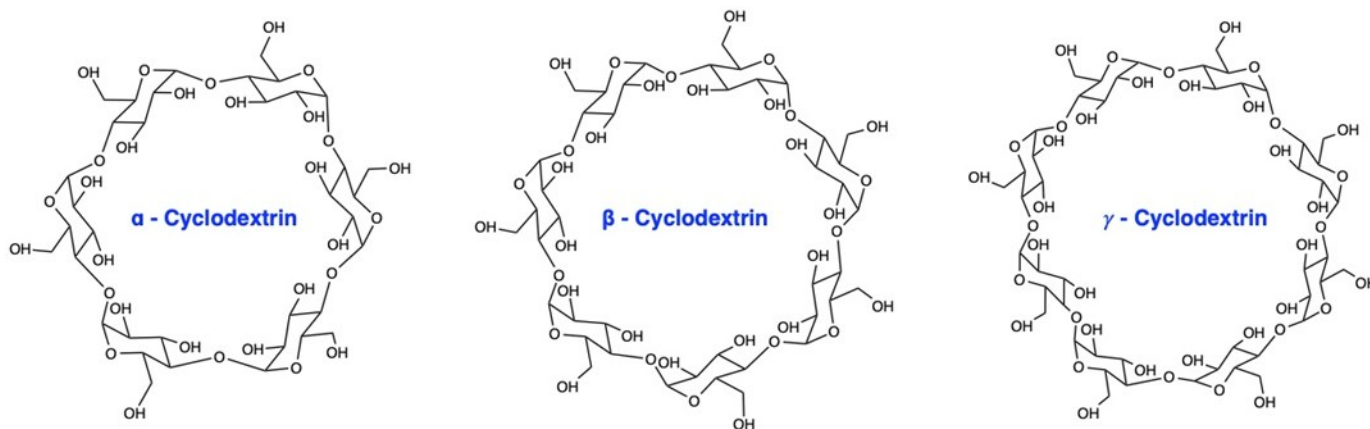
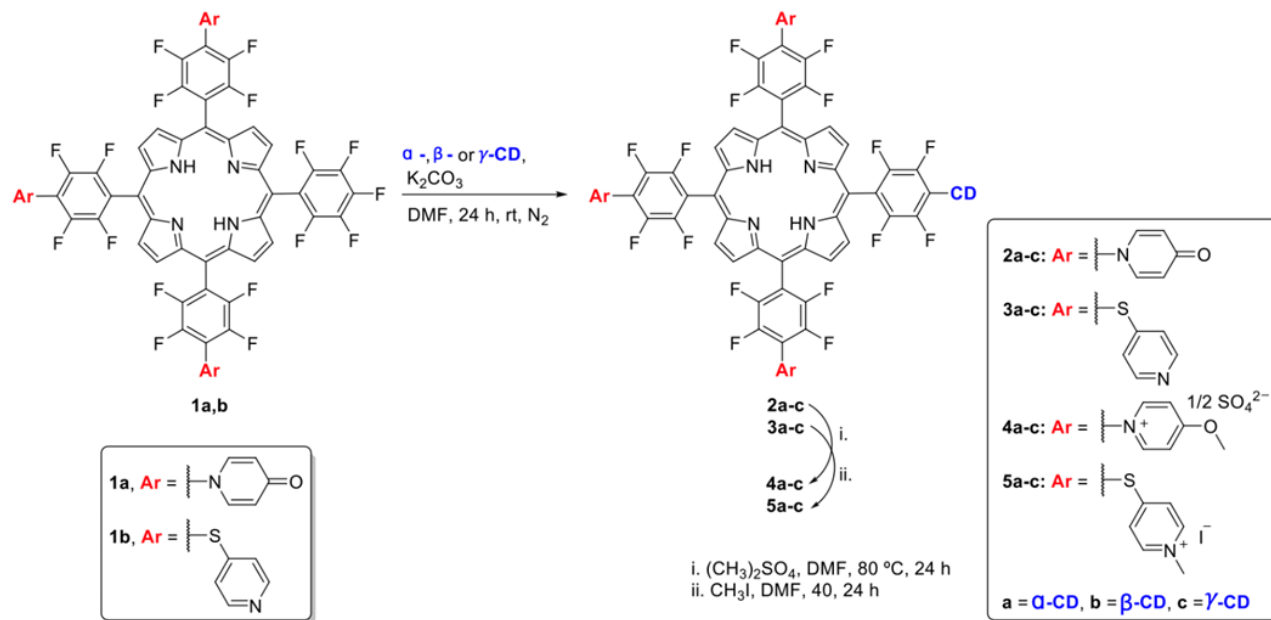


Figure 1 | Structures of α , β and γ cyclodextrins.

2.1. Covalent linkage

The covalent functionalization of porphyrin derivatives with CD can lead to the development of innovative molecular structures. Ribeiro *et al.* [18,19] synthesized two series of asymmetrical cationic free-base PS-CD conjugates containing α -, β - and γ -CD units (Scheme 1). The formation of PS-CD conjugates **4a–c** and **5a–c** involved the reaction of the appropriate neutral porphyrin bearing pyridone **1a** or thiopyridyl **1b** units with K_2CO_3 and α - or γ -CD in dry *N,N*-dimethylformamide (DMF) for 72 h at 60 °C under N_2 atmosphere, yielding the respective neutral porphyrin-CD conjugates **2a–c** and **3a–c** (41–58%). The neutral derivatives were submitted to a cationization reaction with a suitable alkylating agent. The tetracationic porphyrin derivatives bearing inverted methoxypyridinium units **4a–c** were obtained in yields ranging from 43 to 73%, while the corresponding thiopyridinium counterparts **5a–c** were isolated in better yields (70–95%) [18,19].

The photosensitizing properties of porphyrin-CD conjugates were assessed against *E. coli*. Overall, the thiopyridinium derivatives **5a–c** revealed a better performance and capability to photoinactivate the Gram-negative *E. coli*, exhibiting a strong correlation between the 1O_2 generation capability and the aPDT efficiency. Porphyrin-CD conjugate **5c** exhibited the best performance reaching the limit detection of the method at a concentration of 5.0 μM after 15 min at an irradiance of 25.0 mW/cm², while the α -CD counterpart **5a** required 30 min of irradiation under the same conditions. Porphyrin-CD conjugates **4a–c** bearing methoxypyridinium units experienced a poor photodynamic effect at an irradiance of 25.0 mW/cm², have been observed only ≈ 1.5 Log reduction in the viability of *E. coli* by derivative **4c**. An irradiance enhancement to 50.0 mW/cm² led to a better performance for this series of porphyrin-CD conjugates being observed a ≈ 4.0 Log reduction in the viability of *E. coli* in the presence of **4c** and ≈ 3.0 Log with **4a** and **4b** after 60 min of irradiation [18,19].



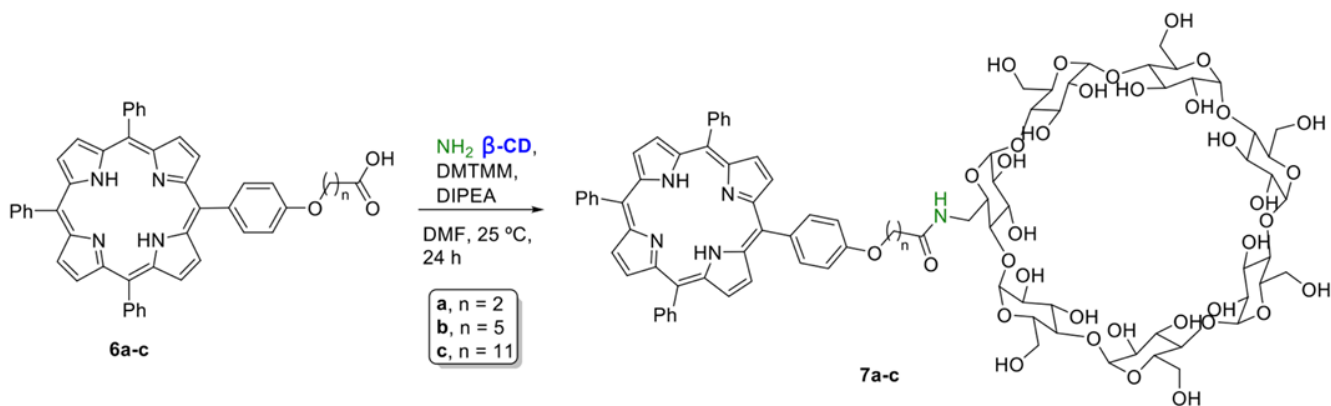
Scheme 1 | Synthetic approach to prepare cationic porphyrin-CD conjugates **4a-c** and **5a-c** prepared by C.P.S. Ribeiro *et al.* [18,19].

aPDT assays showed the relevance of the capability of porphyrin derivatives to generate $^1\text{O}_2$ as well as the position of the positive charge to provide porphyrin-CD-based PS with improved capability to photoinactivate *E. coli*. The positive charge at an external position of the thiopyridinium units of porphyrin-CD conjugates **5a-c** probably enhanced the interaction between the PS and the bacterial membrane enhancing the aPDT effect, while for derivatives **4a-c** the inverted position of the methoxy-pyridinium hindered this interaction. Additionally, the CD cavity size also seems to play a relevant role in the aPDT effect, being the γ -CD preferable compared to α - and β -CD.

Continuous efforts have been made to synthesize CD-based conjugates modified with porphyrin PS to that effectively respond to light. In this context, Panagiotakis *et al.* [20] synthesized

porphyrin β -CD conjugates **7a-c** via amide bond coupling. The process involved reacting mono-(6-amino-deoxy)- β -CD with 5-[4-(4-carboxyalkoxy)phenyl]-10,15,20-triphenylporphyrins, which differed in alkyl chain lengths (**Scheme 2**).

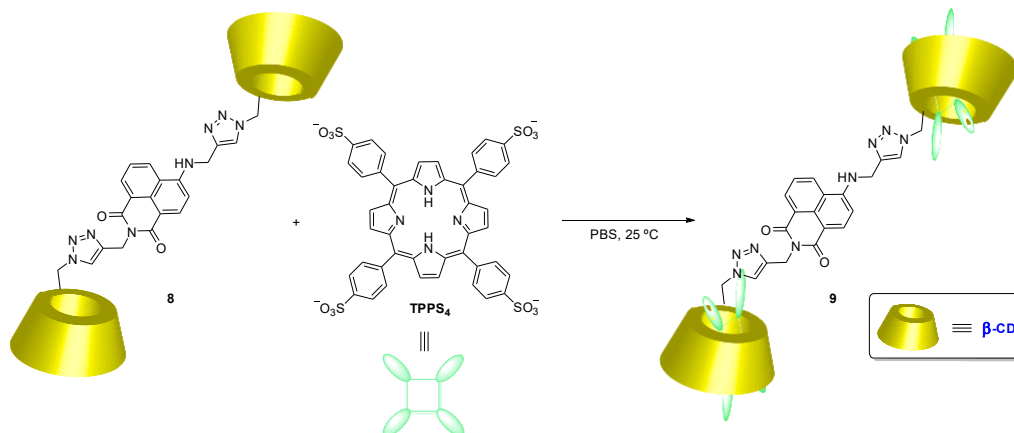
The adequate porphyrin **6a-c** was reacted with amino-functionalized β -CD in the presence of 4-(4,6-dimethoxy-1,3,5-triazin-2-yl)-4-methyl-morpholinium chloride (DMTMM) and *N,N*-diisopropylethylamine (DIPEA) in DMF and under N_2 atmosphere at room temperature for 24 h. After chromatographic purification and dialyzes approach, the porphyrin- β -CD conjugates **7a-c** was obtained as dark brown solids with yields ranging from 56% (**7a**) to 94% (**7c**). Conjugates **7a-c** exhibited the capability to produce $^1\text{O}_2$, a key factor for aPDT applications, when irradiated in PBS [20].



Scheme 2 | Synthesis of porphyrin-CD conjugates **7a-c** prepared by S. Panagiotakis *et al.* [20].

2.2. Supramolecular interaction

The non-covalent interaction between β -CD and porphyrins provides a practical and flexible method for exploring the photophysical and photochemical properties of porphyrins. Additionally, this interaction facilitates the creation of functionalized supramolecular assemblies in water. Yu *et al.* [21] prepared the porphyrin- β -CD conjugate **9** through non-covalent interactions β -CD-factionalized 1,8-naphthalimide-based derivative **8** with 5,10,15,20-tetra(4-sulfonatophenyl)porphyrin (**TPPS₄**)



Scheme 3 | Schematic preparation of porphyrin- β -CD conjugate **9** synthesized by Yu *et al.* [21].

Nanoformulations in drug delivery systems provide significant advantages over traditional treatment methods, including reduced drug toxicity and side effects, improved bioavailability, and sustained drug release at infection sides. Choi *et al.* [22] developed a β -CD formulation incorporating the gallium(III) complex of 5,10,15,20-tetraphenylporphyrin (**TPP**). The preparation of the **CD-GaTPP** conjugate took place in a 10 mM HEPES buffer solution using gallium(III) **TPP** and β -CD through a homogenization technique at room temperature with overnight stirring. The resulting mixture was then sonicated on ice, followed by washing

(**Scheme 3**). This approach involved the previous functionalization of 1,8-naphthalimide core with an excess of permethyl- β -CD under typical Click-chemistry reaction conditions to afford derivative **8**. Then, by taking advantage of the strong binding interactions between the tetraanionic porphyrin derivative **TPPS₄** and the β -CD cavity, the supramolecular assembly was carried out by combining both components in an aqueous solution. In this process, the porphyrin effectively entered the non-polar cavity of CD through Van der Waals interactions, which served as the main binding force and also prevented the self-aggregation of porphyrin [21].

with distilled water and reconstituted in PBS [22].

The use of nanophototherapeutics-based drug delivery system is seen as an effective way to improve the targeted release of PS while reducing the risk of unwanted photosensitization from PS buildup in healthy tissues [23]. Zagami *et al.* [24] developed nanoassemblies by mixing **CAPTISOL[®]** (sulfobutylether- β -cyclodextrin) and 5,10,15,20-tetrakis(1-methylpyridinium-4-yl)porphyrin (**TMPPyP**) in a 1:1 molar ratio and stirred magnetically at room temperature for 10 min. (**Figure 2**).

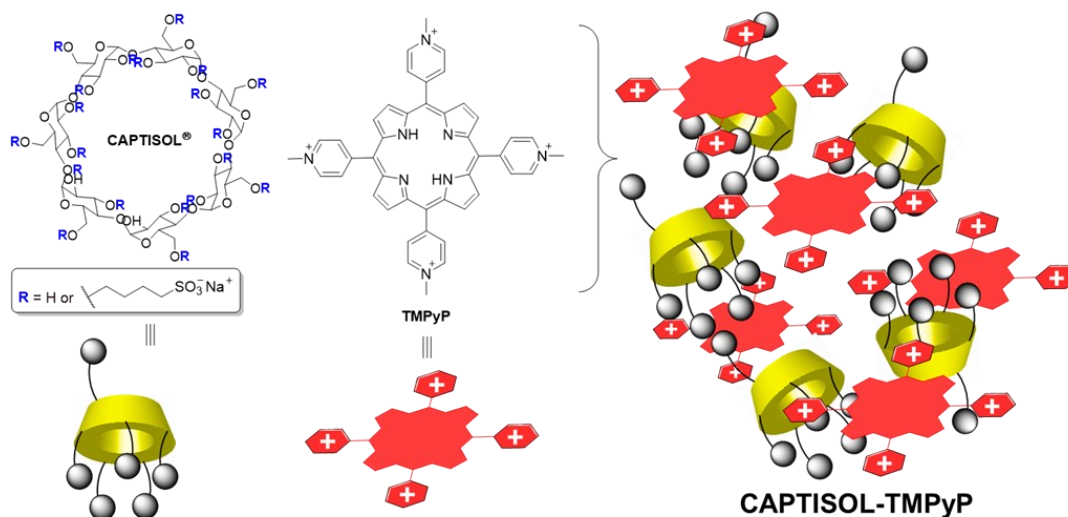
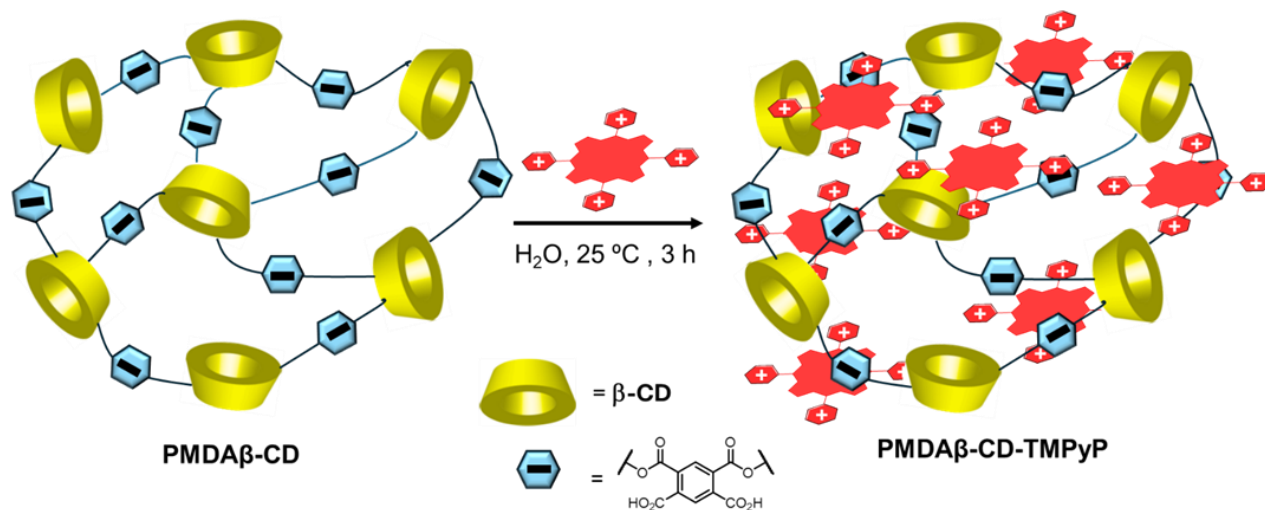


Figure 2 | Outlined depiction of the preparation process for **CAPTISOL-TMPyP** nanoassembly considered in the work by Zagami *et al.* [24].

These innovative nanoformulations not only showed improved PS stability and controlled release but also maintained strong aPDT activity against *P. aeruginosa*, *E. coli*, and *S. aureus*, all at a PS concentration of 6.0 μM and a light dose of 42.0 J/cm^2 against both Gram-positive and Gram-negative bacterial cells. This research highlights the promise of CD-based nanocarriers in enhancing the therapeutic effectiveness of aPDT [24].

The same group studied a different nanoformulation with a CAPTISOL-TMPyP ratio of 50:1. A series of aPDT assays were performed using TMPyP at a 1:50 molar ratio. Notably, this nanosystem demonstrated strong photo-bactericidal activity against both Gram-positive and Gram-negative bacteria with Minimum Inhibitory Concentration (MIC) of 3 μM and 6 μM , respectively. Interesting results were observed in experiments with *P. aeruginosa*, showing that CAPTISOL alone can inhibit the production of pyocyanin, an important virulence factor, while also affecting bacterial biofilm formation. This effect is likely due to the quorum quenching mechanism of CD, which interferes with

bacterial communication among Gram-negative strains. When paired with TMPyP, CAPTISOL demonstrated a synergetic effect, leading to both the inhibition and destruction of *P. aeruginosa* biofilm formation [25]. Later, Zagami *et al.* [26] prepared a three-dimensional network CD-based nanosponges (NS) through a cross-linked approach with pyromellitic dianhydride (PMDA) (Scheme 4). The preparation of the NS doped with TMPyP required the previous preparation of the PMDA β -CD NS by mixing β -CD and PMDA in 8:1 ratio in dimethyl sulfoxide (DMSO) in the presence of triethylamine at room temperature and under vigorous stirring. The obtained NS was then mixed with TMPyP using a mass ratio of 25:1. The resulting dispersion was stirred magnetically for 3 h at room temperature to obtain the PMDA β -CD-TMPyP conjugate. It was observed that NS protects TMPyP from photodegradation rather than controlling its release throughout the treatment period. Also, the incorporation of TMPyP do not compromise its capability to generate $^1\text{O}_2$, since PMDA β -CD-TMPyP conjugate exhibits comparable to $\phi\Delta$ that of free TMPyP (0.67 vs 0.74) [26].



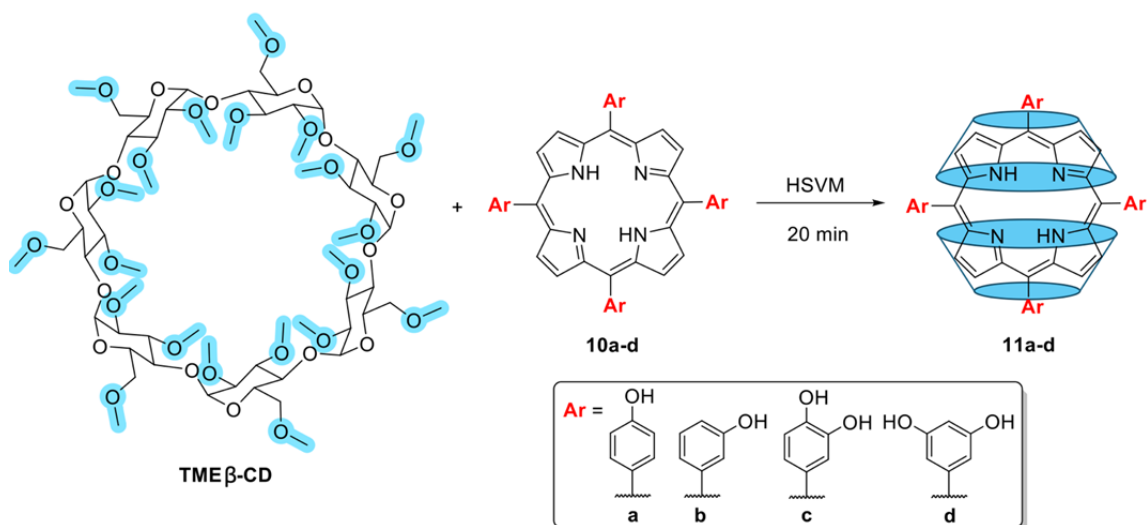
Scheme 4 | Schematic representation of the synthetic approach to prepare the NS PMDA β -CD-TMPyP conjugate developed by Zagami *et al.* [26].

Biological assays were performed to assess the photobacterial activity of both TMPyP and PMDA β -CD-TMPyP conjugate against *P. aeruginosa* and *S. aureus* at a PS concentration of 3.75 μM . It was achieved a complete reduction in bacterial load for both strains. However, while free TMPyP reached the bacterial full photoinactivation after just 1 h with a total light dose of 13.71 J/cm^2 , the PMDA β -CD-TMPyP NS required 4 h of light exposure (54.82 J/cm^2) [26].

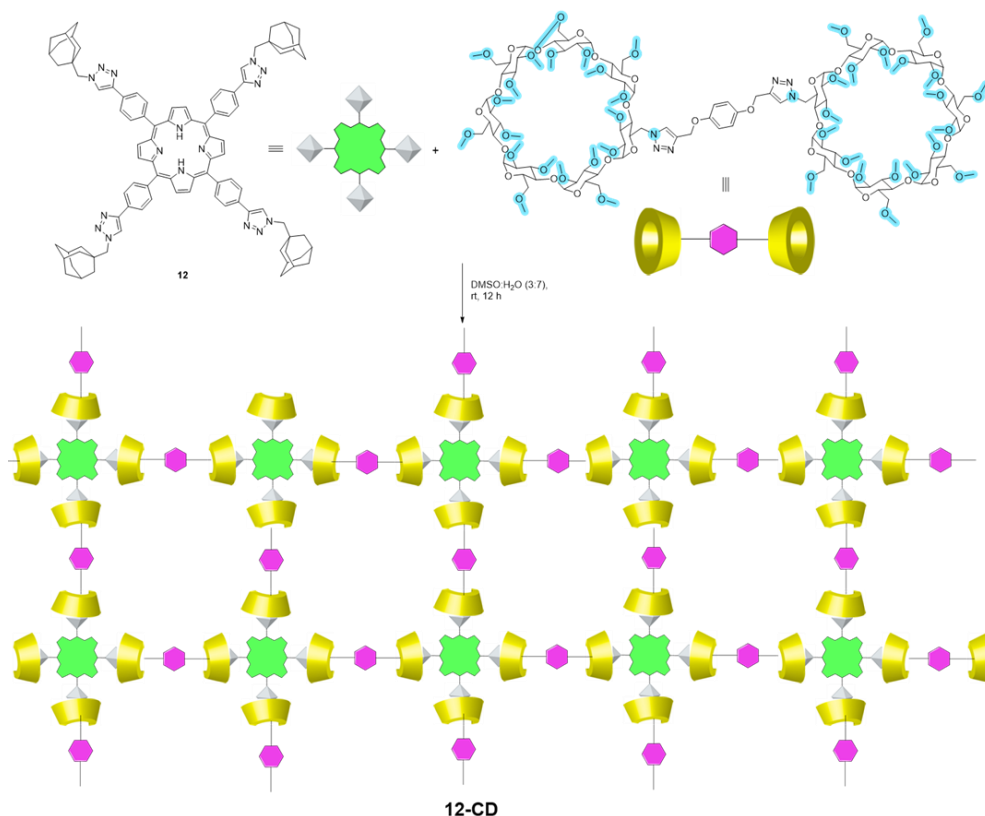
Meso-tetraarylporphyrins bearing hydroxyphenyl (10a,b) or dihydroxyphenyl (10c,d) moieties were successfully encapsulated with two trimethyl- β -CD (TMe β -CD) units (Scheme 5). The formation of the porphyrin-CD supramolecular structure enabled the solubility in water of the porphyrin derivatives eliminating the need for further chemical modifications on the porphyrin core or the use of co-solvents (e.g. DMSO) (Scheme 5). The supramolecular porphyrin-TMe β -CD conjugates 11a-d were

prepared by mixing both components using mechanochemical high-speed vibration-milling (HSVM) technique for 20 min. After this period, the solid mixture was suspended in pure water, following removal of non-encapsulated porphyrin derivatives through centrifugation. All porphyrin derivatives linked with CD successfully generated $^1\text{O}_2$ [14,27].

Xia *et al.* [28] developed a supramolecular porphyrin-CD PS through host-guest and assembling of the tetra-substituted porphyrin-triazolyladamantane derivative 12 with a dimer of permethyl- β -cyclodextrin (Scheme 6). Both components were dissolved in a DMSO/H₂O mixture (3:7) and stirred at room temperature for 12 h, followed by dialysis to remove DMSO to afford 12-CD Conjugate in a 1.33 mg/mL concentration. The supramolecular complex 12-CD demonstrated significant effectiveness in producing $^1\text{O}_2$. These results highlight the potential of the complex as a promising candidate for aPDT [28,29].



Scheme 5 | Schematic preparation of porphyrin-TME β -CD conjugates **11a-d** considered in the work of Ikeda and co-workers [14,27].



Scheme 6 | Schematic representation to prepare **12-CD** conjugate synthesized by Xia *et al.* [28].

3. Chitosan

Chitosan (CS) is a naturally occurring polysaccharide derived from the deacetylation of chitin, composed mainly of β -(1 \rightarrow 4) linked D-glucosamine and N-acetyl-D-glucosamine. Its molecular structure features free amino groups that enhance solubility under acidic conditions and contribute to its mucoadhesive and antimicrobial properties. This polysaccharide is present in the shells of crustaceans and also found in the exoskeletons of insects and the cell walls of certain fungi [30,31]. CS degree of deacetylation and

molecular weight can be adjusted to tailor its functional properties. This versatility makes it a promising material for various biomedical and industrial applications, including drug delivery systems, wound healing scaffolds, and tissue engineering [30,32,33]. In photodynamic approaches, CS biocompatibility, biodegradability, and mucoadhesiveness have been leveraged to develop NPs-based delivery systems that improve the stability, bioavailability, and targeted uptake of PS [34]. Chemical modifications such as acylation, alkylation, and esterification have further enhanced its solubility, mechanical strength, and drug-

release profiles, while its intrinsic antimicrobial activity synergistically enhance the therapeutic effects in combating infections. Additionally, it is cost-effective and environmentally friendly, posing no threat to the ecosystem [35,36].

Castro *et al.* [37] prepared a series of CS-based films modified with different *meso*-tetraarylporphyrins aiming to taking advantage of CS antimicrobial and film forming features. Porphyrin derivatives bearing carboxylic acid units were selected to be immobilized in CS to improve the electrostatic interactions with the CS amino units. and 5,10,15,20-tetrakis(4-carboxyphenyl)porphyrin (**TCPP**) and 5,10,15,20-tetrakis(pentafluorophenyl)porphyrin (**TPFPF**) were prepared through well-described approaches. **TPFPF** was further used as a scaffold to prepare the corresponding thio-carboxylate derivatives **13a,b** through nucleophilic aromatic substitution of the *p*-fluorine atoms in **TPFPF** with 3- and 4-mercaptobenzoic acid (**Figure 3**).

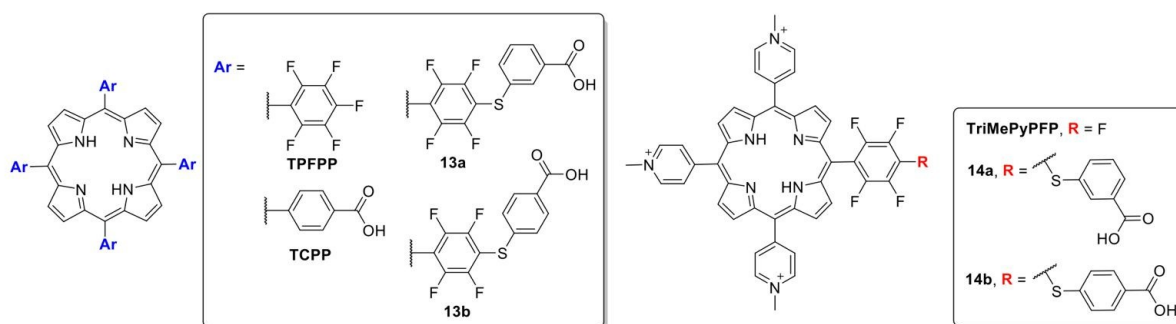


Figure 3 | Structures of porphyrin derivatives used by Castro *et al.* to prepare different CS-based films [37].

This property is dependent on the porphyrin structure and the $^1\text{O}_2$ generation capability of CS films, and the combination of photodynamic inactivation and biofilm prevention makes these materials strong contenders of antifouling coatings, especially in the food industry. The study emphasizes how the structure of porphyrins plays a vital role in influencing the overall aPDT of the CS based materials [37].

In a separate study, Silva *et al* studied the photodynamic activity of **13b@CS** films against cancer cells. The incorporation of **13b** into chitosan nanostructures mitigates aggregation issues associated with non-incorporated **13b** and enhances the photosensitizing properties of **13b@CS** by 3-fold compared to free **13b** in HeLa cells [38].

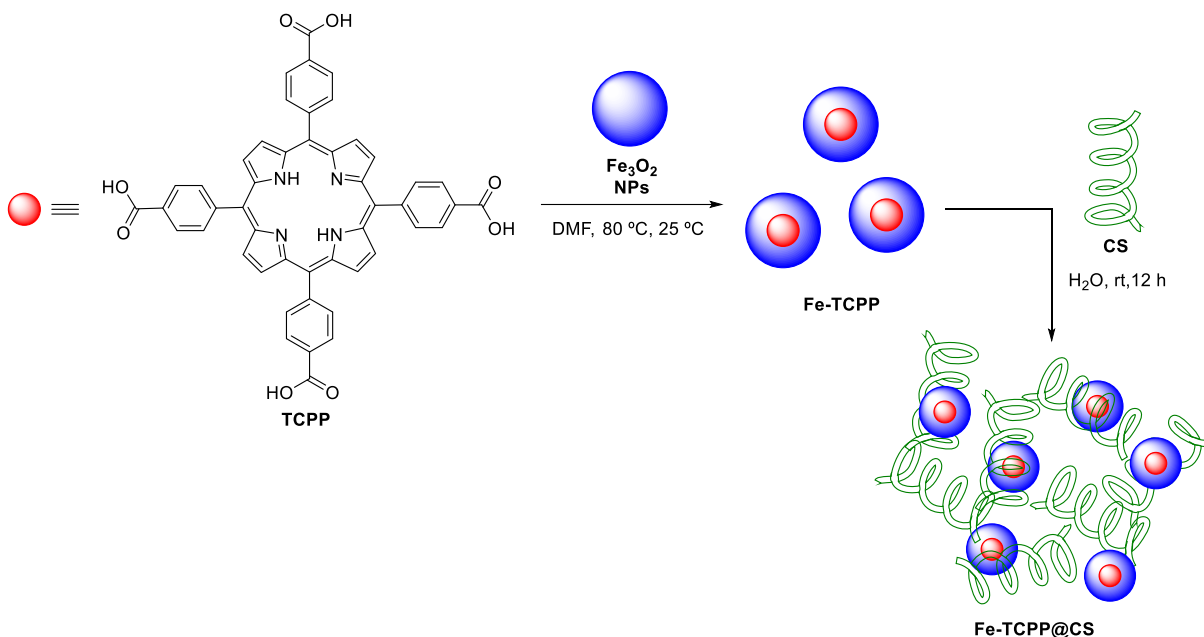
Based on previous results, the same research group studied the immobilization of two tricationic porphyrin derivatives (**14a,b**) featuring a thio-carboxylate units and their precursor **TriMePyPFP** in CS. Then, was assessed the aPDT effectiveness of both **TriMePyPFP@CS** and **14@CS** films towards the bioluminescent Gram-negative *Escherichia coli* bacterium. The results showed that the position of the carboxyl group in the mercapto units or the absence of these substituents in the porphyrin macrocycle modulate

the action of the PS against *E. coli*. Porphyrin **14a,b** after incorporated in CS films, exhibited a poor capability to generate $^1\text{O}_2$ which is strongly correlated with their lack of aPDT effect. After 90 min of exposure to light, only **TriMePyPFP@CS** was able to induce a ≈ 4 Log reduction in the viability of *E. coli* [33].

For the immobilization of porphyrin derivatives within a chitosan matrix, a chitosan solution was slowly added dropwise to the porphyrin solution in acetone, while continuously stirring magnetically. The resulting matrix was stirred in the dark for 72 h at room temperature, allowing for the complete evaporation of acetone to obtain the **porphyrin@CS** hybrid. **TPFPF** exhibited an immobilization rate in CS of 16%, while it was significantly improved for **TCPP** and **13a,b** reaching a porphyrin immobilization rate ranging from 76% (**TCPP**) to 100% (**13a**). This data confirms the relevance of the presence of the carboxylic acid units to enhance the interaction with the CS matrix. The **porphyrin@CS** films exhibited photostability and were effective in generating $^1\text{O}_2$. Additionally, **TCPP** attachment to CS reduced the aggregation-induced quenching of $^1\text{O}_2$ production observed for the free counterpart in solution. The **porphyrin@CS** films displayed anti-adherent characteristics, successfully preventing cell attachment and biofilm formation of *Listeria innocua*.

Zhang *et al.* [39] developed an advanced antimicrobial system by incorporating **Fe-TCPP** NPs into CS. This system leverages the electrostatic targeting of CS in conjugation with aPDT. **TCPP** was coordinated with Fe_3O_2 clusters, forming **Fe-TCPP** NPs (**Scheme 7**). Then, **Fe-TCPP** NPs were encapsulated into a CS matrix. The **Fe-TCPP@CS** nanocomposite were able to induce substantial reduction in 9,10-anthracenediyl-bis(methylene)dimalonic acid (ABDA) absorbance upon light exposure, indicating a strong capacity for ROS production [39].

The efficacy of **Fe-TCPP@CS** was evaluated against both Gram-positive *S. aureus* and Gram-negative *E. coli* bacterial strains. Upon exposure to white light (0.3 W/cm^2 , 10 min) at a concentration of $20 \mu\text{g/mL}$, was able to induce a 97% reduction in the viability of *S. aureus*. However, **Fe-TCPP@CS** nanocomposite was much less effective against *E. coli*. Even after a ten-fold increase in the PS concentration, it only reached a bacterium photoinactivation lower



Scheme 7 | Schematic representation depicting the synthesis approach used to prepare Fe-TCPP@CS nanocomposite by Zhang *et al.* [39].

than 50%. To enhance efficacy against *E. coli*, the researchers investigated a synergistic approach combining aPDT with photothermal therapy. This combined strategy achieved approximately 98% elimination of *E. coli* at a concentration of 100 µg/mL under 635 nm laser irradiation (1.0 W/cm², 10 min). The ¹O₂ generation capability of Fe-TCPP@CS nanocomposite highlights their potential as a promising candidates for advancing aPDT in the treatment of bacterial infections through a combined synergistic effect with photothermal therapy [39].

Hasanin *et al.* [40] investigated the potential of 5,10,15,20-tetrakis(3-hydroxyphenyl)porphyrin (**10b**) loaded onto an CS and ethyl cellulose (EC)-CS nanocomposites, activated by laser irradiation, for combating multidrug-resistant bacteria (**Figure 4**) [40]. Laser irradiation of free **10b** in the blue region (70 mW, 15 min) resulted in a significant reduction in microbial survival rates. The **10b@CS**

nanocomposite exhibited a slightly reduced efficacy under identical blue light irradiation conditions. However, the incorporation into EC-CS biopolymeric matrix not only retained the photodynamic activity of **10b** but also enhanced its physicochemical properties, particularly the absorption in the therapeutic red region (635 nm). The **10b@CE-CS** nanocomposite demonstrated remarkable reductions in microbial survival rates upon exposure to 635 nm laser light (5.0 mW/cm², 15 min), highlighting its potential as a highly effective therapeutic agent [40].

Introducing diamagnetic heavy metal ions into the porphyrin cavity significantly fine-tune its photophysical and photochemical properties, typically leading to an increase in the ¹O₂ production capability through enhanced intersystem crossing compared to the corresponding free-base counterpart [41,42]. Sen *et al.* [43] prepared a series of porphyrin@CS nanocomposites **15a-c** through

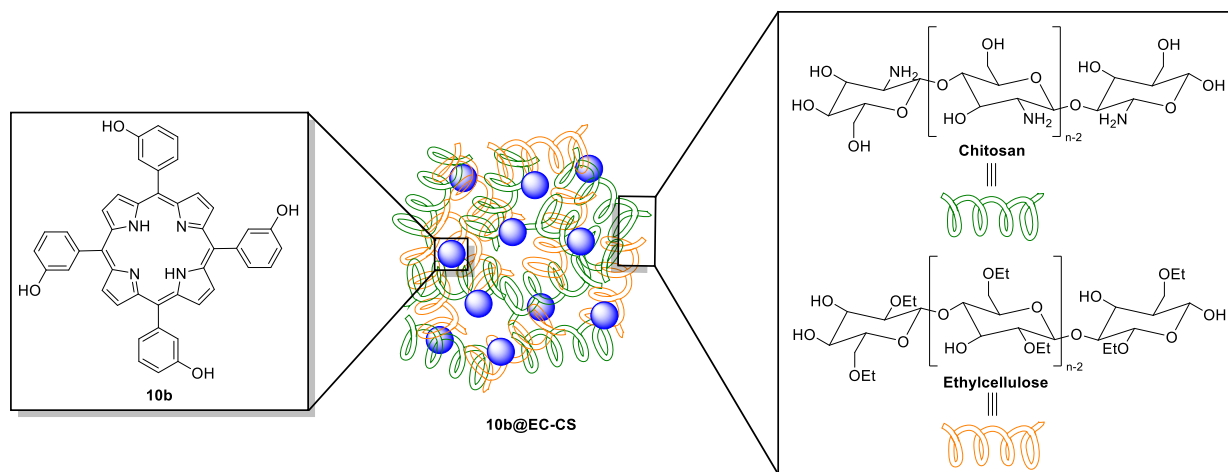


Figure 4 | Schematic representation of **10b@EC-CS** nanocomposite used in the work of Hasanin *et al.* [40].

the incorporation of 5,10,15,20-tetrakis(4-dibutylaminophenyl) porphyrin **15a** and their neutral and tetracationic Pd(II) complexes **15b,c** into CS. As expected the incorporation of the heavy metal Pd(II), have been the CS-based nanocomposite prepared with the tetracationic metalloporphyrin **15c** those with the highest efficiency in the generation of the cytotoxic species $^1\text{O}_2$ [43].

The authors assessed the photo-antimicrobial properties of the **porphyrin@CS** nanocomposites against *S. aureus*, focusing on the impact of Pd(II) ion, molecular charge, and CS conjugation on aPDT efficiency (Figure 5A-C) [43]. The tetracationic metalloporphyrin **15c** and their CS conjugate demonstrated better

photoinactivation activity, even at low PS concentration (0.5 μM), reaching the full photoinactivation of *S. aureus* after 15 min of irradiation. Meanwhile the non-embedded counterpart required 30 min of irradiation under the same conditions to achieve identical results (Figure 5C). These results highlighted the best performance of the **porphyrin@CS** conjugates which can be attributed to the synergistic antibacterial properties of CS, which contribute to an amplified photoinactivation effect. Nonetheless, the improved activity also inducing some dark toxicity. The poor effectiveness of the neutral derivatives **15a,b** is mainly related to their propensity for aggregation in aqueous media, which compromises aPDT effect [43].

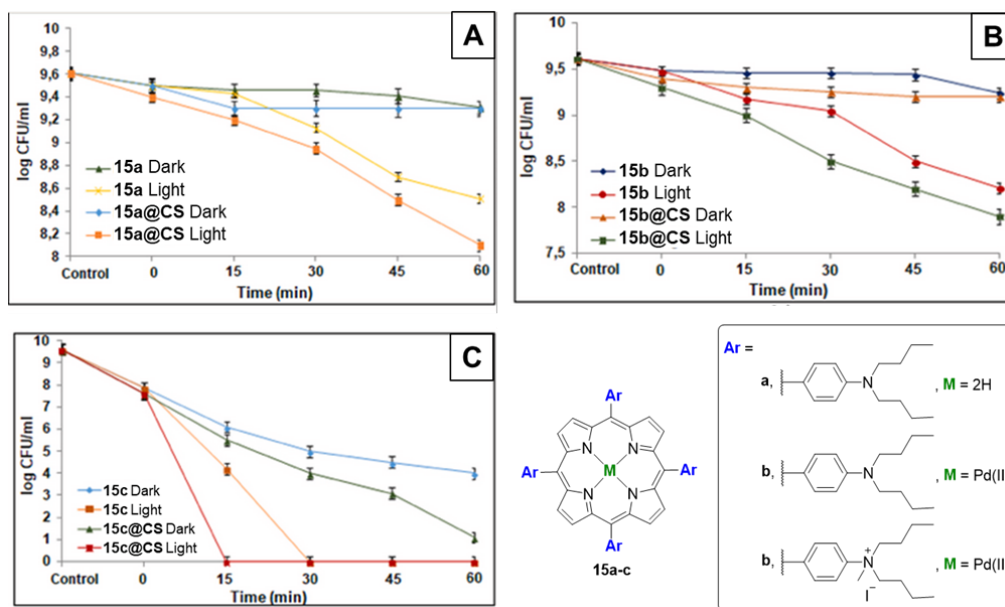


Figure 5 | Evaluation of the photo-antimicrobial activity of **porphyrin@CS** hybrids against *S. aureus*. Adapted from reference [43]

4. Lignin

Lignin (Li) is a complex, aromatic and heterogeneous organic polymer that constitutes a key component of plant cell walls, providing structural integrity and resistance against environmental stresses. Although it is most abundant in wood, lignin is also present in other plant tissues such as bark and fibers [44,45]. Chemically, lignin is a phenolic polymer with a highly variable structure, formed through the polymerization of phenolic monomers such as coniferyl, sinapyl, and *p*-coumaryl alcohol. The specific composition and linkage patterns of these monomers differ among plant species. Beyond its various industrial applications, lignin has attracted considerable interest as a renewable and sustainable resource. Researchers have been investigating its potential for producing biofuels and other value-added products, which could contribute to the advancement of a sustainable bioeconomy [46,47].

Despite its natural abundance, Li has historically received limited attention for photodynamic therapy applications, mainly due to its

inherent antioxidant properties. Recently, however, lignin has emerged as a promising material in PDT research. Researchers have been exploring lignin-based NPs as delivery vehicles for PS, aiming to enhance their delivery and improve therapeutic efficacy. These lignin-based nanocarriers offer notable benefits, including biocompatibility, biodegradability, and the potential for targeted tissue delivery [48].

Carmona *et al.* [49] employed a multi-step procedure to encapsulate 5,10,15,20-tetrakis(4-hydroxyphenyl)porphyrin (**10a**) within acetylated lignin (AcLi) to obtain **10a@AcLi** NPs (Scheme 11). This approach involved the previous acetylation of Li by reacting a kraft lignin with acetic anhydride and dry pyridine 1:1 mixture at room temperature for 48 h. To obtain **10a@AcLi** hybrids, a **10a** and AcLi mixture was prepared in acetone, following by 24 h dialysis against water and 1 h centrifugation (Figure 6). **10a@AcLi** NPs exhibited high stability, with minimal **10a** leakage (9%) and both **10a@AcLi** and the non-encapsulated porphyrin counterpart AcLi demonstrated $^1\text{O}_2$ production after 30 minutes of irradiation [49].

The authors assessed the potential of **10a@AcLi** as PS against several bacterial strains of both Gram-positive and Gram-negative bacteria (**Figure 6**) [49]. The study evaluated the aPDT effect of **10a@AcLi** NPs and found out that they were quite effective against Gram-positive bacteria, achieving 99.9% reduction in survival at concentrations below 5 μM when exposed to low doses of white LED light (4.16 J/cm², 1 h irradiation). However, under the same

irradiation conditions did not show noticeable impact on Gram-negative bacteria. The study suggests that the reason for the lack of effectiveness against Gram-negative bacteria might be due to the impermeability of their cell walls to the nanoparticles. TEM observations showed that **10a@AcLi** remained outside the bacterial cells, affecting the cell wall and causing flocculation (**Figure 6**).

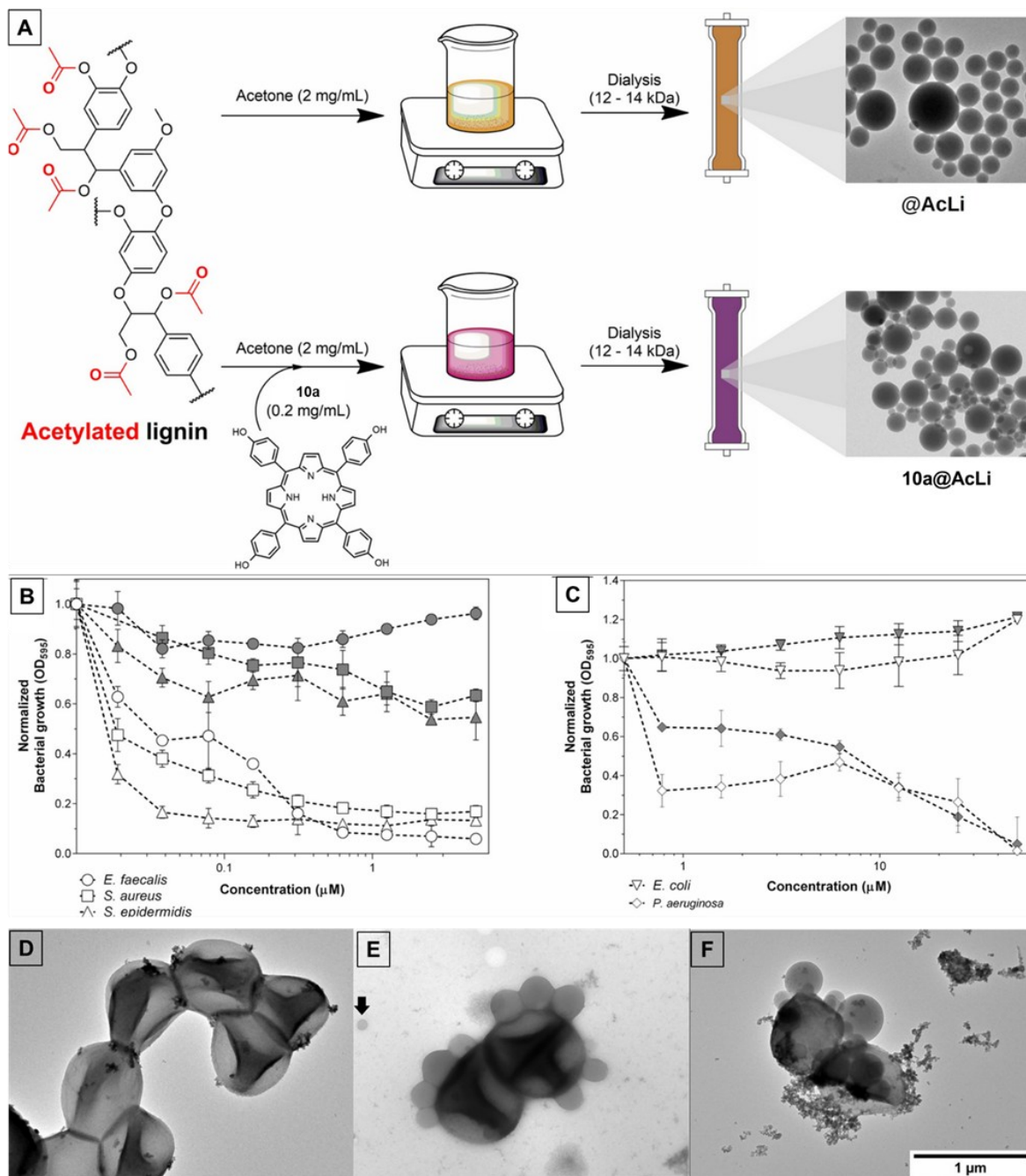


Figure 6 | A) Preparation of acetylated lignin-based **@AcLi** and **10a@AcLi** NPs. Bacteriostatic effect of **10a@AcLi** NPs after light irradiation (white LED light dose, 4.16 J/cm², white symbols) or dark incubation (gray symbols) against **B**) three Gram-positive bacteria and **C**) two Gram-negative bacteria. Transmission electron microscopy (TEM) observations of **D**) *S. aureus* cells in vivo; **E**) *S. aureus* and **10a@AcLi**, the black arrow indicates a non-bound nanoparticle; and **F**) *S. aureus* and **10a@AcLi** after light irradiation (incandescent bulb, 2,500 luxes, 5 min). Adapted from reference [49]

The same group followed an analogous protocol to incorporate a series of neutral and cationic free-base porphyrin derivatives **16a-c** and the Zn(II) complex **17** (Figure 7) to prepare other **porphyrin@AcLi** NPs to explore structure-activity relationship [50,51]. The **porphyrin@AcLi** NPs follows similar trends for both

$^1\text{O}_2$ generation capability and fluorescence quantum yield as follows **16c@AcLi** > **16a@AcLi** > **16b@AcLi** > **10a@AcLi** > **17@AcLi** [49,51]. This study revealed the higher relevance of the pyridinium units to provide better performance in both properties.

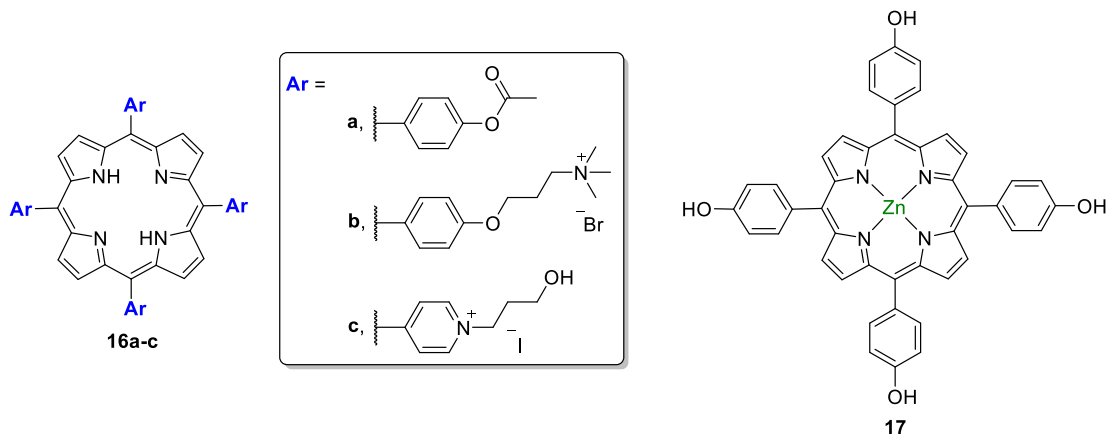


Figure 7 | Chemical structures of free-base porphyrin derivatives **16a-c** and Zn(II) complex **17** incorporated into AcLi NPs by Carmona *et al.* [50,51].

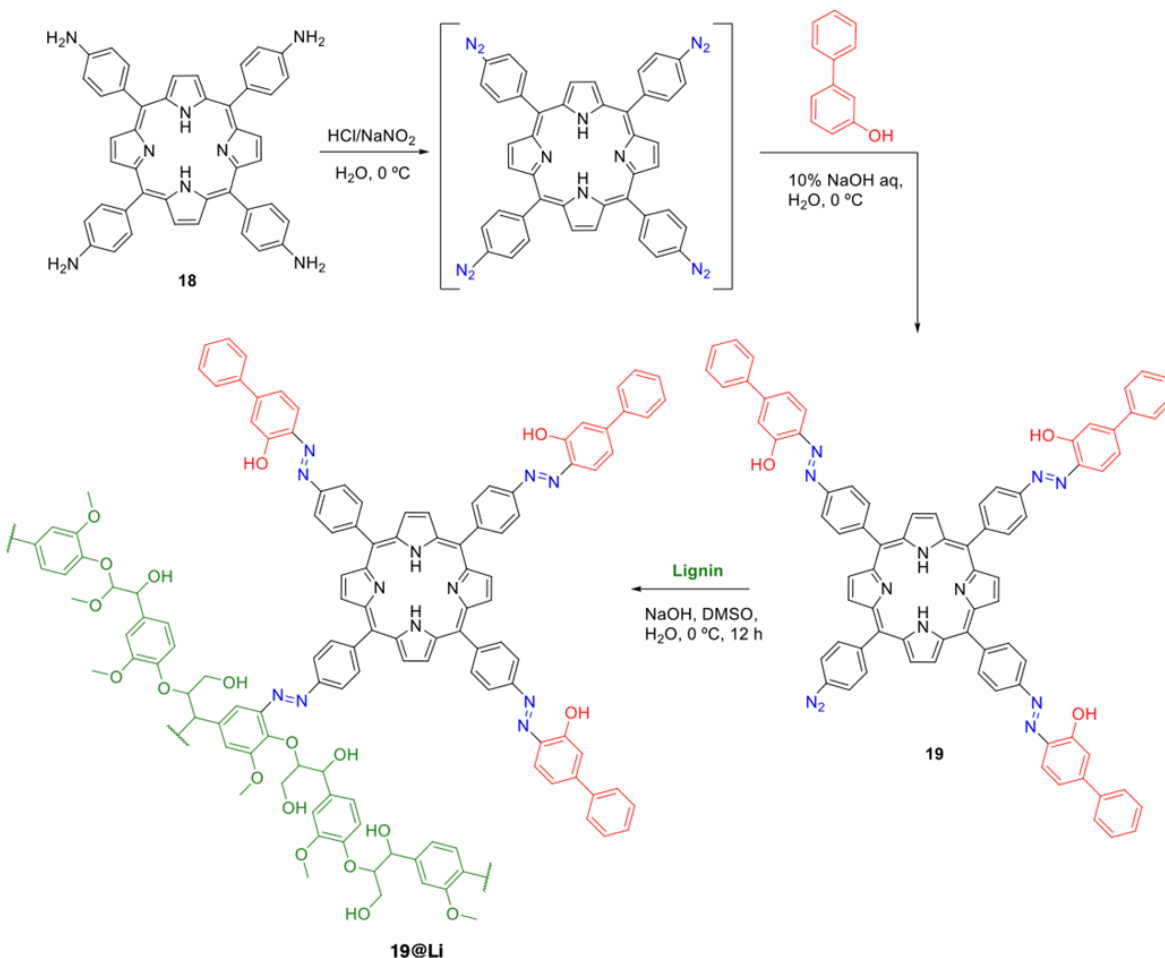
The photo-antimicrobial properties of **porphyrin@AcLi** NPs were further evaluated against *S. aureus* and *E. coli*. Their previous findings have established the efficacy of **10a@AcLi** in eradicating Gram-positive bacteria under white LED light exposure (4.16 J/cm², 1 h irradiation). The minimal bactericidal concentrations (MBC) for Gram-positive bacteria were lower, with effective aPDT results at 2.5 μM of **10a@AcLi**. However, even when **10a@AcLi** was used at a concentration of 50 μM, it was not able to induce a reduction in the viability of Gram-negative bacteria under the same irradiation conditions. This emphasizes how **10a@AcLi** was selective against Gram-positive bacteria while falling against Gram-negative bacterial strains [49]. The aPDT effect of **10a@AcLi**, **16a-c@AcLi** and **17@AcLi** NPs and the corresponding non-encapsulated porphyrin was further assessed against *S. aureus* and *E. coli* upon exposure to blue LED light (455 ± 5 nm, 15.0 J/cm², 30 min). While encapsulation generally led to a decrease in light-dependent antibacterial activity, for example compound **10a** showed a light activated MBC of 0.0488 μM, while **10a@AcLi** was 0.7813 μM against *S. aureus*, it conferred a significant advantage by minimizing dark toxicity, for example compound **17** showed dark toxicity at around 0.3 μM against *S. aureus*, whereas compound **17@AcLi** showed no effect at 50 μM. Notably, the encapsulation of the lipophilic porphyrin **16a**, which was inactive in its free form (>50 μM MBC against *S. aureus*), enhanced its bactericidal efficacy when encapsulated (**16a@AcLi** showed ≈ 2.5 log reduction at 12.5 μM). The mechanism of action for the encapsulated porphyrins appears to involve localized generation of ROS at the bacterial surface. For *E. coli*, free cationic porphyrins like **16b,c** exhibited greater activity, and the impact of encapsulation on their efficacy varied significantly [51]. Tse *et al.* [52] developed a one-pot synthetic strategy to synthesize sustainable lignin NPs decorated with porphyrin moieties. Lignin-based NPs **19@Li** were prepared under mild reaction conditions through a typical 5-5' linkage

interunit azo-coupling between porphyrin **17** and alkali lignin (AL) (Scheme 8). Porphyrin **19** was previously prepared via a two-step approach from 5,10,15,20-tetrakis(4-aminophenyl)porphyrin **18** involving the sequential preparation of the corresponding diazonium salt then underwent a one-pot coupling reaction with 2-phenylphenol yielding the diazonium-porphyrin **19**. **19@Li** NPs exhibited capability to generate $^1\text{O}_2$ ($\phi\Delta = 0.62$) and robust photostability, thereby underscoring their potential application in PDT [52].

Concluding remarks

The growing threat posed by drug-resistant pathogens is prompting a reevaluation of antimicrobial strategies. In this context, aPDT using PS like porphyrin derivatives is emerging as a promising approach. To make aPDT more practical and cost-effective, researchers are exploring methods to attach PS to solid supports for efficient recovery and reuse. Various biopolymeric matrixes, such as CD, CS and Li, are being investigated for this purpose, each offering unique advantages in terms of stability, targeted delivery, and overall effectiveness. Additionally these materials are readily accessible and biocompatible, contributing to the cost-effectiveness and environmental friendliness of aPDT approach. One major challenge with using porphyrin-based PS is their tendency to aggregate in water, which can reduce their effectiveness. To address this issue, considerable research is focused on developing advanced nanostructures that can encapsulate and deliver porphyrin-based PS more effectively, thereby improving their solubility, stability, and selectivity for target pathogens.

Detailed structure-activity relationship studies have underscored the critical role of both the CD type and porphyrin substitution patterns in tailoring these conjugates for specific applications. The



Scheme 8 | Synthetic approach to synthesize **19@Li** NPs considered in the work of Tse *et al.* [52].

formation of functional supramolecular assemblies in aqueous solutions, driven by non-covalent interactions effectively mitigates porphyrin aggregation while enhancing water solubility, resulting in efficient ¹O₂ generation and improved photostability.

The porphyrin incorporation in CD nanosponges and exploring solvent-free synthetic methodologies further broaden the therapeutic potential of these systems, emphasizing the promise of porphyrin-CD conjugates in a wide range of biomedical applications. The unique benefits of CS are also being actively harnessed in aPDT. CS not only boost the stability and bioavailability of PS, but its inherent antimicrobial properties make it a highly appealing material. Researchers are currently delving into innovative strategies like CS-encapsulated metal-organic nanoparticles, which show promising effectiveness against multidrug-resistant bacteria. These advancements suggest that aPDT utilizing CS could be effective in treating various diseases, including infections and cancer. Additionally, the exploration of lignin-based nanoparticles as innovative carriers for PS has opened exciting new paths in aPDT, particularly against Gram-positive bacterial infections. This approach highlights the potential of using sustainable biomaterials like lignin in the battle against infectious diseases.

In summary, the thoughtful combination of the beneficial properties of biopolymeric materials, such as CD, CS, and Li with the phototherapeutic capabilities of porphyrin derivatives represents a significant and promising direction in developing innovative therapeutic strategies for a wide range of health issues, including bacterial infectious diseases and cancer.

Funding

This research work received financial support from University of Aveiro and Fundação para a Ciência e Tecnologia and Ministério da Ciência, Tecnologia e Ensino Superior (FCT/MCTES) for the financial support of the UID/50006 - Laboratório Associado para a Química Verde - Tecnologias e Processos Limpos unit through national funds. FMP Morais also thanks FCT for his doctoral grant (UI/BD/154486/2022). NMM Moura gratefully acknowledges FCT for an Assistant Research Position under the Individual Scientific Employment Stimulus - 6th Edition (2023. 06495.CEECIND). CL thanks the PROTEOMASS Scientific Society (Portugal) by the funding provided through the General Funding Grant 2024-2025, and by the funding provided to the Laboratory for Biological Mass Spectrometry Isabel Moura (#PM001/2019 and #PM003/2016). C.L. thanks the Royal Society of Chemistry for the Sustainable Laboratory Grants 2023 reference L23-8861107285.

Acknowledgements

The authors thank the University of Aveiro and FCT/MCTES for financial support to UID/50006 - Laboratório Associado para a Química Verde - Tecnologias e Processos Limpos.

References

- [1] N. Kashef, Y.-Y. Huang, M.R. Hamblin, *Nanophotonics* 6 (2017) 853–879. DOI: 10.1515/nanoph-2016-0189
- [2] C. Vieira, A.T.P.C. Gomes, M.Q. Mesquita, N.M.M. Moura, M.G.P.M.S. Neves, M.A.F. Faustino, A. Almeida, *Front. Microbiol.* 9 (2018) 1–16. DOI: 10.3389/fmicb.2018.02665
- [3] M. Q. Mesquita, C. J. Dias, M. P. M. S. Neves, A. Almeida, M. F. Faustino, *Molecules* 23 (2018) 2424. DOI: 10.3390/molecules23102424
- [4] M.R. Hamblin, *Curr. Opin. Microbiol.* 33 (2016) 67–73. DOI: 10.1016/j.mib.2016.06.008
- [5] H. Abrahamse, M.R. Hamblin, *Biochem. J.* 473 (2016) 347–364. DOI: 10.1042/BJ20150942
- [6] A.M. Udrea, A. Smarandache, A. Dinache, C. Mares, S. Nistorescu, S. Avram, A. Staicu, *Pharmaceutics* 15 (2023) 2124. DOI: 10.3390/pharmaceutics15082124
- [7] I.S. Mfouo-Tynga, L.D. Dias, N.M. Inada, C. Kurachi, *Photodiagnosis Photodyn. Ther.* 34 (2021) 102091. DOI: 10.1016/j.pdpdt.2020.102091
- [8] R. Baskaran, J. Lee, S.-G. Yang, *Biomater. Res.* 22 (2018) 25. DOI: 10.1186/s40824-018-0140-z
- [9] J.M. Dąbrowski, B. Pucelik, A. Regiel-Futyra, M. Brindell, O. Mazuryk, A. Kyzioł, G. Stochel, W. Macyk, L.G. Arnaut, *Coord. Chem. Rev.* 325 (2016) 67–101. DOI: 10.1016/j.ccr.2016.06.007
- [10] A. Almeida, M.A. Faustino, J.P. Tomé, *Future Med. Chem.* 7 (2015) 1221–1224. DOI: 10.4155/fmc.15.59
- [11] A.N. Hurst, B. Scarbrough, R. Saleh, J. Hovey, F. Ari, S. Goyal, R.J. Chi, J.M. Troutman, J.L. Vivero-Escoto, *Int. J. Mol. Sci.* 20 (2019) 134. DOI: 10.3390/ijms20010134
- [12] N. Malatesti, I. Munitic, I. Jurak, *Biophys. Rev.* 9 (2017) 149–168. DOI: 10.1007/s12551-017-0257-7
- [13] J. Singh, I. Dhamija, H. Meehenian, N. Kumar, S. Simran, M. Muskan, M.L. Verma, S. Kumar, *Bull. Natl. Res. Cent.* 46 (2022) 202. DOI: 10.1186/s42269-022-00904-y
- [14] A. Ikeda, S. Satake, T. Mae, M. Ueda, K. Sugikawa, H. Shigetou, H. Funabashi, A. Kuroda, *ACS Med. Chem. Lett.* 8 (2017) 555–559. DOI: 10.1021/acsmchemlett.7b00098
- [15] P. Ahmadi, A. Ahmadi, M. Tabibiazar, S. Hamidi, S. Ramezani, *Carbohydr. Polym.* 353 (2025) 123241. DOI: 10.1016/j.carbpol.2025.123241
- [16] L.A. Gusmão, A.E.H. Machado, J.R. Perussi, *Photodiagnosis Photodyn. Ther.* 40 (2022) 103073. DOI: 10.1016/j.pdpdt.2022.103073
- [17] P. Saha, M.R. Rafe, *Heliyon* 9 (2023) e19287. DOI: 10.1016/j.heliyon.2023.e19287
- [18] C.P.S. Ribeiro, M.A.F. Faustino, A. Almeida, L.M.O. Lourenço, *Microorganisms* 10 (2022) 0–13. DOI: 10.3390/microorganisms10040718
- [19] C.P.S. Ribeiro, S.R.D. Gamelas, M.A.F. Faustino, A.T.P.C. Gomes, J.P.C. Tomé, A. Almeida, L.M.O. Lourenço, *Photodiagnosis Photodyn. Ther.* 31 (2020) 101788. DOI: 10.1016/j.pdpdt.2020.101788
- [20] S. Panagiotakis, B. Mavroidi, A. Athanasopoulos, A.R. Gonçalves, L. Bugnicourt-Moreira, T. Regagnon, N. Boukos, G. Charalambidis, A.G. Coutsolelos, M. Grigalavicius, T.A. Theodossiou, K. Berg, C. Ladavière, M. Pelecanou, K. Yannakopoulou, *Carbohydr. Polym.* 306 (2023) 120579. DOI: 10.1016/j.carbpol.2023.120579
- [21] J. Yu, S. Xiao, F. Chen, L. Li, G. Xu, *Dye. Pigment.* 180 (2020) 108518. DOI: 10.1016/j.dyepig.2020.108518
- [22] S.-R. Choi, G.A. Talmon, B.E. Britigan, P. Narayanasamy, *ACS Infect. Dis.* 7 (2021) 2299–2309. DOI: 10.1021/acsinfecdis.0c00896
- [23] S. Shaikh, P.S. Chary, N.K. Mehra, *Int. J. Pharm.* 671 (2025) 125277. DOI: 10.1016/j.ijpharm.2025.125277
- [24] R. Zagami, D. Franco, J.D. Pipkin, V. Antle, L. De Plano, S. Patanè, S. Guglielmino, L. Monsù Scolaro, A. Mazzaglia, *Int. J. Pharm.* 585 (2020) 119487. DOI: 10.1016/j.ijpharm.2020.119487
- [25] D. Franco, R. Zagami, L.M. De Plano, N. Burduja, S.P.P. Guglielmino, L.M. Scolaro, A. Mazzaglia, *Molecules* 28 (2023). DOI: 10.3390/molecules28062493
- [26] R. Zagami, A. Rubin Pedrazzo, D. Franco, F. Caldera, L.M. De Plano, M. Trapani, S. Patanè, F. Trotta, A. Mazzaglia, *Int. J. Pharm.* 637 (2023). DOI: 10.1016/j.ijpharm.2023.122883
- [27] T. Yumoto, S. Satake, S. Hino, K. Sugikawa, R. Kawasaki, A. Ikeda, *Org. Biomol. Chem.* 18 (2020) 6702–6709. DOI: 10.1039/D0OB01379J
- [28] L. Xia, J. Wu, B. Huang, Y. Gao, J. Tian, W. Zhang, *Chem. Commun.* 56 (2020) 11134–11137. DOI: 10.1039/d0cc03574b

- [29] L. Greci, J. Kaczor, P. Carloni, E. Damiani, L. Greci, P. Stipa, F. Tanfani, E. Tartaglini, M. Wozniak, *Res. Clwm. Lntermed* 19 (1993) 395–405.
- [30] S. Qu, X. Ma, S. Yu, R. Wang, *Front. Bioeng. Biotechnol.* 11 (2023) 1–11. DOI: 10.3389/fbioe.2023.1234758
- [31] M. Kołodziejaska, K. Jankowska, M. Klak, M. Wszola, *Nanomaterials* 11 (2021) 1–44. DOI: 10.3390/nano11113019
- [32] B. Sultankulov, D. Berillo, K. Sultankulova, T. Tokay, A. Saparov, *Biomolecules* 9 (2019) 470. DOI: 10.3390/biom9090470
- [33] K.A.D.F. Castro, N.M.M. Moura, F. Figueira, R.I. Ferreira, M.M.Q. Simões, J.A.S. Cavaleiro, M.A.F. Faustino, A.J.D. Silvestre, C.S.R. Freire, J.P.C. Tomé, S. Nakagaki, A. Almeida, M.G.P.M.S. Neves, *Int. J. Mol. Sci.* 20 (2019) 2522. DOI: 10.3390/ijms20102522
- [34] R. Yañez-Macías, A. Muñoz-Bonilla, M.A. De Jesús-Tellez, H. Maldonado-Textle, C. Guerrero-Sánchez, U.S. Schubert, R. Guerrero-Santos, *Polymers (Basel)*. 11 (2019) 1789. DOI: 10.3390/polym11111789
- [35] C. Hu, D. Jiang, Y. Zhang, H. Gao, Y. Zeng, N. Khaorapong, Z. Liu, Y. Yamauchi, M. Pan, *Coord. Chem. Rev.* 523 (2025) 216264. DOI: 10.1016/j.ccr.2024.216264
- [36] D. Tahir, A. Ardiansyah, H. Heryanto, E.E.M. Noor, M.A. Mohamed, *Int. J. Biol. Macromol.* 298 (2025) 140010. DOI: 10.1016/j.ijbiomac.2025.140010
- [37] K.A.D.F. Castro, N.M.M. Moura, A. Fernandes, M.A.F. Faustino, M.M.Q. Simões, J.A.S. Cavaleiro, S. Nakagaki, A. Almeida, Á. Cunha, A.J.D. Silvestre, C.S.R. Freire, R.J.B. Pinto, M. da G.P.M.S. Neves, *Dye. Pigment.* 137 (2017) 265–276. DOI: 10.1016/j.dyepig.2016.10.020
- [38] L.B. Silva, K.A.D.F. Castro, C.E.A. Botteon, C.L.P. Oliveira, R.S. da Silva, P.D. Marcato, *Front. Bioeng. Biotechnol.* 9 (2021) 1–15. DOI: 10.3389/fbioe.2021.679128
- [39] Y. Zhang, J. Ma, D. Wang, C. Xu, S. Sheng, J. Cheng, C. Bao, Y. Li, H. Tian, *Biomater. Sci.* 8 (2020) 6526–6532. DOI: 10.1039/D0BM01427C
- [40] M.S. Hasanin, M. Abdelraof, M. Fikry, Y.M. Shaker, A.M.K. Sweed, M.O. Senge, *Molecules* 26 (2021). DOI: 10.3390/molecules26123551
- [41] C. Musewald, G. Hartwich, F. Pöllinger-Dammer, H. Lossau, H. Scheer, M.E. Michel-Beyerle, *J. Phys. Chem. B* 102 (1998) 8336–8342. DOI: 10.1021/jp982309z
- [42] H.L. Kee, J. Bhaumik, J.R. Diers, P. Mroz, M.R. Hamblin, D.F. Bocian, J.S. Lindsey, D. Holten, *J. Photochem. Photobiol. A Chem.* 200 (2008) 346–355. DOI: 10.1016/j.jphotochem.2008.08.006
- [43] P. Sen, R. Soy, S. Mgidlana, J. Mack, T. Nyokong, *Dye. Pigment.* 203 (2022) 110313. DOI: 10.1016/j.dyepig.2022.110313
- [44] M. Erfani Jazi, G. Narayanan, F. Aghabozorgi, B. Farajidizaji, A. Aghaei, M.A. Kamyabi, C.M. Navarathna, T.E. Mlsna, *SN Appl. Sci.* 1 (2019) 1–19. DOI: 10.1007/s42452-019-1126-8
- [45] E. Csiszár, D. Kun, F. Temesváry-Kis, E. Fekete, *Carbohydr. Polym. Technol. Appl.* 9 (2025) 100743. DOI: 10.1016/j.carpta.2025.100743
- [46] M. Balk, P. Sofia, A.T. Neffe, N. Tirelli, *Int. J. Mol. Sci.* 24 (2023) 11668. DOI: 10.3390/ijms241411668
- [47] G. Marchand, G. Fabre, N. Maldonado-Carmona, N. Villandier, S. Leroy-Lhez, *Nanoscale Adv.* 2 (2020) 5648–5658. DOI: 10.1039/D0NA00615G
- [48] X. Liu, M. Li, X. Li, M. Ge, S. Liu, S. Li, J. Li, J. Ding, A.J. Ragauskas, W. Sun, T.D. James, Z. Chen, *Mater. Today Chem.* 26 (2022) 101000. DOI: 10.1016/j.mtchem.2022.101000
- [49] N. Maldonado-Carmona, G. Marchand, N. Villandier, T.S. Ouk, M.M. Pereira, M.J.F. Calvete, C.A. Calliste, A. Žak, M. Piksa, K.J. Pawlik, K. Matczyszyn, S. Leroy-Lhez, *Front. Microbiol.* 11 (2020) 1–17. DOI: 10.3389/fmicb.2020.606185
- [50] G. Piccirillo, N. Maldonado-Carmona, D.L. Marques, N. Villandier, C.A. Calliste, S. Leroy-Lhez, M.E.S. Eusébio, M.J.F. Calvete, M.M. Pereira, *Catal. Today* 423 (2023) 113903. DOI: 10.1016/j.cattod.2022.09.009
- [51] N. Maldonado-Carmona, T.S. Ouk, N. Villandier, C.A. Calliste, M.J.F. Calvete, M.M. Pereira, S. Leroy-Lhez, *Antibiotics* 10 (2021) 1–26. DOI: 10.3390/antibiotics10050513
- [52] H.Y. TSE, C.S. Yeung, C.Y. Lau, M.Y. Cheung, J. Guan, M.K. Islam, P.T. Anastas, S.Y. Leu, *Green Chem.* 24 (2022) 2904–2918. DOI: 10.1039/d2gc00196a